Modeling diffraction of nanostructured materials: a combined theoretical and experimental study

Robert Koch

3 December 2015

Approved by

Prof. Riccardo Ceccato, University of Trento
Prof. David Bish, Indiana University
Prof. Federica Bondioli, University of Parma

Koch, Robert. *Modeling diffraction of nanostructured materials: a combined theoretical and experimental study.* PhD Thesis, University of Trento (2015).

For my family

Contents

List of Equations

List of Tables

List of Figures

Chapter 1

Introduction

1.1 Historical perspective

A large portion of the field of materials science is focused on understanding and exploiting underlying patterns in relative atomic positions within solid materials. For reasonably ordered materials, such understanding and exploitation rests firmly on the pillars of *crystallography* and *diffraction*, which together provide the theory and practical tools to measure and decode these patterns.

Phenomena characterized by diffraction, or the scattering and resulting interference or superposition of waves, are pervasive within the natural world. In fact, the color blue as seen in vertebrates can be attributed *solely* to diffraction of visible light[1]. This suggests that Mother Nature has been exploiting diffraction phenomena long before *Homo Sapiens* even contemplated the wave nature of light.

Although diffraction can arise when any type of waves are involved, this work focuses on the diffraction of X-rays, a subset of light with a wavelength from roughly 0.01 to 10 nm. First systematically studied by Wilhelm Röntgen in 1895 [2], X-rays or "Röntgenstrahlung" were initially exploited for medical imaging. Later, following a conversation with Peter Ewald, Max von Laue used this new type of rays to collect the first X-ray diffraction photographs with Walter Friedrich and Paul Knipping in 1913 [3]. von Laue used his understanding of crystallography to offer an interpretation of this image [4]. On the basis of this work, the father-son pair, Bragg and Bragg correctly interpreted

the new diffraction phenomena, and provided a simple mathematical relationship to compute inter-atomic spacings based on the position of what would soon be called "Bragg spots" [5]. With these pioneering experiments, von Laue and the Braggs launched the field of X-ray crystallography and earned themselves separate Nobel Prizes in physics.

Many of the theoretical underpinnings of *crystallography*, or the study of how objects or atoms fill space, were actually known before diffraction facilitated the measurement of atomic positions. In 1892, a complete list of the 230 three-dimensional space groups, based on arguments of group theory and including rigorous mathematical descriptions, was enumerated in personal communications between the mathematicians Fedorov and Schönflies. This work laid the foundation for the future of diffraction based crystallography.

In the years since the inception of diffraction and crystallography, 29 Nobel Prizes have been awarded for work related to these topics. It is also evident that the field of materials science, fueled largely by crystallography and diffraction, has quite literally been the driving force behind many of the technological leaps and bounds of the last century, from Moore's law to modern medicine. The importance of these topics is then clear, from both a practical and theoretical perspective.

1.2 Goals and motivations

The novel components of this work are focused largely on the close investigation of diffracted X-ray intensity distributions from nanopowders showing stacking disorder (or one-dimensional disorder). Additionally, a general goal of this work is also to give a broader overview of what can be considered an emerging field of diffraction techniques in general: modeling of diffracted intensity distributions without empirical assumptions on the constituent profile shapes, positions, or relative intensities.

With the exception of total scattering studies, the first goal of most diffraction experiments is to accurately measure the position and relative intensity of Bragg diffraction peaks so as to understand the unit cell shape and contents (the lattice and the basis of the structure). A alternate goal is often the careful analysis of the shape of these Bragg diffraction peaks. The advent of modern personal computers and the

resulting availability of pattern decomposition softwares have largely simplified and expedited these processes [6–8]. Such whole pattern fitting approaches are based on the hypothesis that diffracted intensity distributions can be modeled as a sum Bragg peaks, or line-profiles, with shapes, positions, and relative intensities constrained by simple models [9–11].

The recent interest in nanomaterials, however, gives justification for abandoning such a hypothesis. These materials often show novel and useful properties and are characterized by spatially anisotropic and inhomogeneous order on nanometer scales. This complex structure, along with instrumental optics, act as a convolution [12] on an instrument source profile to create a similarly complex diffracted intensity distribution frequently at odds with the previously mentioned simple models [13, 14]. The failure of traditional crystallography based assumptions in this case has been called "the nanostructure problem" [15]. It represents a significant roadblock for materials scientists and engineers [16], and its solution requires a new approach.

The first true steps away from traditional assumptions were made by Cheary and Coelho in the fundamental parameters (FP) approach [9]. This technique uses the physical parameters of the diffractometer, such as the divergent slit angle, the length of the X-ray anode, or the angular aperture of the Soller slits, directly within physical models to compute the instrumental effect on the measured intensity distribution. These models provide a complete and physical description of the instrumental line-profile shape, position-shift, and relative intensity across the full angular range of the diffractometer. A FP instrumental line-profile then shows all the anisotropy and asymmetry entailed by the specific diffractometer set-up without the need to invoke empirical profiles.

While the work of Cheary and Coelho as implemented in the TOPAS software package [8] has allowed crystallographers to physically model the *instrumental* effect on diffracted intensity distributions, simple empirical models are still frequently used to represent the *sample-related* contribution to these intensity distributions. The trend in full width at half maximum (FWHM) or integral breadth β (the ratio of the peak intensity to the peak area) associated with the fitted sample signal is then often related to the microstrain and the average size of the coherently scattering domains (CSDs) through rather simple models [17–19]. The

choice of *which* empirical profile to use is however quite arbitrary, and could bias the result of the analysis [19, 20]. Furthermore, the exact details of the sample nanostructure are hidden subtly in profile asymmetries, shifts, and other fine details, which are themselves masked by the effect of the instrument. Assuming an empirical profile shape to represent the sample signal can obscure these details completely. Using more complex models including asymmetric and shifted (but still empirical) profiles introduces further complications, as the relationship between asymmetries/position shifts and structure/microstructure must be arduously derived explicitly for each material [21].

Surprisingly, the theoretical foundations for computing sample-related diffracted intensity distributions directly without empirical approximations have existed for many years. In general each is based on expressing how a physical phenomena perturbs the ideal crystal lattice or unit cell, and then propagating the perturbation to the Fourier transform (FT) of the crystal. In 1940 Ewald first suggested directly evaluating the FT of a crystal to obtain the diffracted intensity [22]. Shortly after, Stokes and Wilson presented a strategy (and several formulas) for directly computing the anisotropic line-profiles due to finite crystals with various morphologies and arbitrary atomic structure [23]. Wilkens later provided expressions for the anisotropic line-profile shapes associated with microstrain due to dislocations [24]. In his book originally published in 1969, Warren outlined an approach to computing the line-profile associated with planar defects in close packed structures [21]. A more general approach for one-dimensional disorder was outlined even earlier by Hendricks and Teller [25]. Probably owing to a lack of computational power, most of these approaches have been used *only* to arrive at explicit expressions for the *change* in profile position, FWHM, or asymmetry associated with these phenomena. These changes are extracted from powder diffraction data by pattern decomposition (empirical profile fitting) and then fed into the explicit expressions.

Recently in a series of papers, Scardi and Leoni outlined the collection and implementation of many of these approaches in what they have called whole powder pattern modelling (WPPM), where parameters of the sample, such as the shape of the CSDs and the associated CSD size distribution, are used directly within the above physical models to compute the sample line-profile without invoking empirical profile

functions [20, 26, 27]. This was followed quickly by a similar approach proposed by Ribárik *et al.* [28]. The two techniques have been implemented in the PM2K [29] and MWP-fit [28] software packages and have proven to be rather useful at extracting real microstructural information from materials [30–38], but are unfortunately not yet as pervasive as the FP approach.

Within this work, Chapter 2 gives a review of some above-mentioned strategies to derive direct expressions for diffracted intensity distributions from nanocrystalline or one-dimensionally disordered samples. The general paths followed there can be used to derive intensity distribution equations considering other perturbations to ideal crystal structures. This is in fact the route taken at the end of this chapter, where a new generalized model is presented for polydisperse nanocrystalline materials showing extensive stacking disorder.

In Chapter 3 the direct expressions presented in Chapter 2 are tested in several virtual diffraction experiments. The methods of virtual powder "synthesis" are outlined, along with the approach for carrying out a virtual diffraction experiment using the Debye scattering equation (DSE). The synthetic powder diffraction patterns from virtual powders with various nano and microstructures are compared and discussed. These powder patterns are then characterized following different approaches from Chapter 2 to assess the validity and accuracy of those different models.

In Chapter 4, a number of different samples of industrially relevant boron nitride are considered. Two different hypotheses regarding the nature of the nanostructure of these samples are tested, entailing the use of two different diffraction data fitting approaches from Chapter 2. This chapter provides for the first time clear conclusions regarding the nature of the nanostructure of these samples. After suggesting a most probable model for nanostructure, this model is used to track the details of the boron nitride phase transformation under high pressure, as a function of synthesis temperature.

Chapter 2

Modeling diffraction

The diffracted intensity distribution from a collection of atoms can be computed directly by following two general routes. With what are typically called direct-space (DS) approaches, all atomic positions within each domain are specified explicitly and used directly to build the intensity distribution without any assumptions regarding long-range order. While DS approaches allow for true atomic scale control over the intensity distribution, the required computational overhead scales quadratically with the number of scatterers (atoms) [39] and with the sixth power of the domain linear dimensions. This can lead to intractable computation times if the mean domain size is large and the atomic-configuration space of the sample is broad, as with broad crystal size distributions or complex stacking disorder. DS approaches are explored in Chapter 3.

The presence of three-dimensional translational periodicity such as that characterizing traditional crystals can be exploited to achieve significant mathematical simplifications and a reduction of computational overhead. This entails working in a Fourier transformed space, or reciprocal-space (RS), where the elastic scattering of periodic objects can be represented more simply. Imperfections can be treated as perturbations to the crystal lattice or unit cell, and their effect on the diffracted intensity distribution can be treated. Understanding such perturbations is the primary focus of this chapter.

In both DS and RS approaches, the starting point is the elastic scattering of X-rays from an electron, reviewed in Section 2.2, yielding the

polarization correction. Following this, in Section 2.3 a review of X-ray scattering from an isolated atom is given, leading to the typical atomic form factor description. Next, a mathematical description of a perfect, spatially infinite crystal, and its associated kinematic diffraction behavior is presented in Section 2.4. It is here that the traditional structure factor of the unit cell appears, as well Bragg's law [5] for calculating line-profile positions. Following this, a review of the mathematical description of otherwise perfect, spatially finite crystal is given in Section 2.5, along with the elastic scattering and interference that results from such objects. A general approach for representing an ensemble-averaged crystal showing *disorder* in one direction is shown in Section 2.6, with expressions for computing the associated diffracted intensity distribution. This section offers some novel extensions to previous work in the field. In Section 2.7 the general and physical models for crystal size, elaborated in Section 2.5, are used with the models for stacking disorder, outlined in Section 2.6, to give a novel and general RS description of diffraction from polydispersed, nanocrystalline materials showing extensive linear disorder.

Any of the above described scattering models can be used to understand real samples. By assuming a specific model with appropriate initial parameters, a theoretical intensity distribution can be computed. An attempt can be made to minimize the total (weighted and/or squared) difference between the observed and calculated intensity distributions by refining the model parameters as constrained by the model assumptions. If a suitable solution is found, it can provide a best guess for the crystal structure (Rietveld analysis [11]) or the sample microstructure and defect content (line-profile analysis (LPA) [12, 17–19]). If a suitable solution is not found, it can be necessary to start the process over, altering or abandoning some of the initial assumptions regarding crystal structure, unit cell symmetry, or empirical profile shape.

2.1 Practical examples: Nickel

Throughout the next two chapters various highly theoretical concepts are explored. To cast these abstract concepts in a more concrete manner, following a general treatment, many are presented in the specific

case of metallic nickel. This choice was made based on the relative simplicity of the nickel structure, as complex abstract concepts can be demonstrated without introducing additional structural complications.

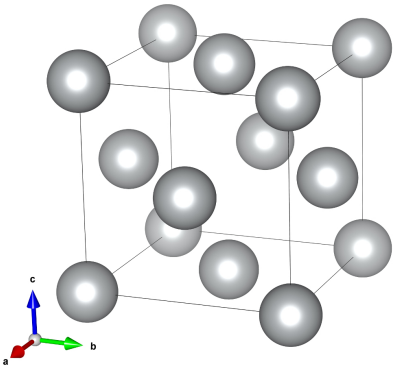

Figure 2.1: A perspective view of the face-centered cubic (fcc) unit cell for metallic nickel.

In the bulk form, metallic nickel adopts the fcc structure, with space group $Fm\bar{3}m$ and a lattice parameter of 3.52 Å[40, 41]. A perspective view of a bulk nickel unit cell is shown in Figure 2.1. Interestingly, *nanocrystalline* nickel is stable in both the fcc and hexagonal close packed (hcp) polytypes [42], strongly suggesting the possibility of both polytypes existing simultaneously interlayered within single nanocrystals.

Such polytype interlayering is an extreme case of stacking disorder which manifests in close-packed structures in a more dilute form as stacking faults, namely twin or deformation faults. Projections of the fcc unit cell and an idealized hcp unit cell along the $[\bar{2}20]$ or [310] directions are shown in Figures 2.2a or 2.2c, respectively. From these views, it is simple to identify a common layer structure: Warren [21] pointed out that both the fcc and hcp polytypes are composed of layers of atoms arranged in a primitive hexagonal lattice, with bi-dimensionally periodic unit cell vectors $\mathbf{a}_l$, and $\mathbf{b}_l$, and layer thickness c_l that can be

written as

$$\mathbf{a}_l = -\frac{\mathbf{a}_c}{2} + \frac{\mathbf{b}_c}{2} \tag{2.1a}$$

$$\mathbf{b}_l = -\frac{\mathbf{b}_c}{2} + \frac{\mathbf{c}_c}{2} \tag{2.1b}$$

$$c_l = \frac{1}{3} \left\| \mathbf{a_c} + \mathbf{b_c} + \mathbf{c_c} \right\|, \tag{2.1c}$$

where $\mathbf{a}_c$, $\mathbf{b}_c$, and $\mathbf{c}_c$ are the typical cubic unit cell vectors. This layer *does not* have a third lattice vector, as it shows only two-dimensional periodicity. It is however a three-dimensional object with a layer thickness c_l. The symmetry of this new layer unit cell is best described with the sub-periodic layer group $p6/mmm$ (number 80) [43], with one nickel atom at Wyckoff position $1a$. This layer unit cell is shown in Figure 2.2b.

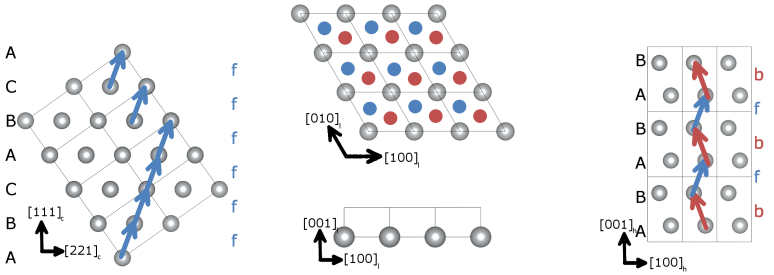

(a) fcc unit cells

(b) common layer unit cell

(c) hcp unit cells

Figure 2.2: In (a), a projected view of several fcc nickel unit cells is shown, with the Warren layer type identified at left, and relative translation identified at right. The same is shown in (c) for several idealized hcp nickel unit cells. In (b), the layer unit cell common to both polytypes is shown, both in a top and front view. The indicated directions are with respect to the lattice of the closest pictured structure. Forward or backward relative translations are indicated by the color blue or red, respectively

If only the *relative* horizontal positions of two adjacent layers are considered, it is clear that there are only two possibilities: either the layers

are related by a "forward" shift, represented by the relative position vector $\mathbf{R}_f = \frac{\mathbf{a}_l}{3} - \frac{\mathbf{b}_l}{3} + c_l\hat{\mathbf{z}}$, or the layers are related by a "backward" shift, represented by the relative position vector $\mathbf{R}_b = -\frac{\mathbf{a}_l}{3} + \frac{\mathbf{b}_l}{3} + c_l\hat{\mathbf{z}}$. This description is consistent with the Hägg approach [44], where "forward" and "backward" are represented by "+" and "-," and can be contrasted with the work of Warren, who described the two polytypes based on the three *absolute* positions of the atomic scale layers, describing the fcc polytype as an $\ldots ABCABC \ldots$ sequence and the hcp polytype as an $\ldots ABAB \ldots$ sequence [21]. These relative and absolute notations are also shown in Figure 2.2.

2.2 A single scattering center

To begin, scattering from a single free electron is considered, as depicted schematically in Figure 2.3. If a plane-wave of X-ray radiation with wavelength λ and wave-vector $\mathbf{k}_0$, where $\|\mathbf{k_0}\| = k_0 = 1/\lambda$, interacts with a free electron, the electron oscillates due to the electric field $\mathbf{E}_0$ of the incident X-ray and radiates X-rays with electric field $\mathbf{E}_f$. If the spherical wave is observed at a distance r and scattering angle 2θ with respect to $\mathbf{k}_0$, then it appears as a plane-wave with wave-vector $\mathbf{k}_f$ and electric field $\mathbf{E}_f/r$. The momentum transfer vector or *scattering vector* $\mathbf{s}$ can be defined as the difference between the final and initial wave-vectors, $\mathbf{s} = \mathbf{k}_f - \mathbf{k}_0$. If the interaction is purely elastic (Thomson scattering) then $k_0 = k_f$, with $\|\mathbf{s}\| \equiv s = \frac{2\sin\theta}{\lambda}$. In the elastic case, the electric field of the scattered radiation can be written in terms of $\mathbf{E}_0$ and the Thomson scattering cross section, $\mathbf{E}_f = \frac{e^2}{m_e c^2 r}\mathbf{E}_0$. Inelastic (Compton) scattering is not considered in this work.

The degree and direction of linear polarization of the incident beam Q can be written in terms of components of the time averaged squared electric field, or intensity, that are parallel ($\|$) and perpendicular ($\perp$) to the plane of incidence

$$Q = \frac{\langle \mathbf{E}_{0\perp} \rangle^2 - \langle \mathbf{E}_{0\|} \rangle^2}{\langle \mathbf{E}_{0\|} \rangle^2 + \langle \mathbf{E}_{0\perp} \rangle^2} = \frac{I_{0\perp} - I_{0\|}}{I_{0\perp} + I_{0\|}} = \frac{I_{0\perp} - I_{0\|}}{I_0}. \tag{2.2}$$

Q ranges from -1 (linearly polarized parallel to the incident plane) to 1 (linearly polarized perpendicular to the incident plane).

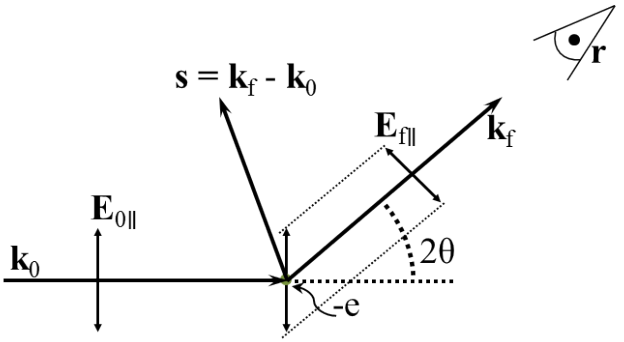

Figure 2.3: An X-ray with wave-vector $\mathbf{k}_0$ and electric field $\mathbf{E}_0$ impinging on a free electron with charge -e and mass m_e. The radiation, with electric field $\mathbf{E}_f$, is elastically scattered to $\mathbf{k}_f$. The geometric meanings of the scattering vector $\mathbf{s}$ and of the scattering angle 2θ are also shown.

By geometrical arguments (Figure 2.3) the scattered intensity components can be written in terms of the incident intensity components as $I_{f\parallel} = \frac{e^4}{{m_e}^2 c^4 r^2} I_{0\parallel} \cos^2 2\theta$ and $I_{f\perp} = \frac{e^4}{{m_e}^2 c^4 r^2} I_{0\perp}$. The total scattered intensity I_f can then be written as a sum of its components as a function of the scattering vector or angle,

$$\begin{aligned} I_f(\theta) &= I_{f\perp} + I_{f\parallel} \\ &= \frac{e^4}{{m_e}^2 c^4 r^2} I_{0\perp} + \frac{e^4}{{m_e}^2 c^4 r^2} I_{0\parallel} \cos^2 2\theta \\ &= \frac{e^4}{{m_e}^2 c^4 r^2} \left(I_{0\perp} + I_{0\parallel} \cos^2 2\theta \right) \\ &= \frac{e^4}{{m_e}^2 c^4 r^2} I_0 \left(\frac{(1+Q) + (1-Q)\cos^2 2\theta}{2} \right). \end{aligned} \tag{2.3}$$

The last factor in equation 2.3 is typically called the polarization factor PF, and it indicates that the elastically scattered intensity is *not* dependent on the wavelength, but rather on *both* the scattering angle 2θ *and* the degree and direction of linear polarization of the incident beam Q. When the incident radiation is completely unpolarized, the case for most laboratory X-ray sources, then $Q = 0$ and $PF = \frac{1+\cos^2 2\theta}{2}$. Here

PF is initially 1 at $\theta = 0$, decreasing to a minimum of 1/2 when $\theta = 45°$, and increasing again to 1 at $\theta = 90°$. When the incident radiation is polarized completely perpendicular to the plane of incidence, such as in most synchrotron X-ray sources, then $Q = 1$ and $PF = 1$, showing no dependence on the scattering angle.

While these results are absolutely essential for correctly interpreting diffraction data, they generally lead to fluctuations in the diffracted intensity distribution which are dependent *only* on the experimental configuration. These dependencies include the initial beam intensity or polarization rather than the atomic, nano, or microstructure of the sample. It is however precisely this sample-specific information that is the focus of this work. For the sake of compactness then, the polarization factor, initial beam intensity, and Thomson cross section terms are omitted from the equations within the following sections, where the elastically diffracted intensity distributions from various different types of crystals are elaborated. In practice, only factors that vary with scattering angle, such as the polarization factor, need be considered explicitly. The other constant terms involving the Thomson cross section can be effectively absorbed into a general scale factor.

2.3 An isolated atom

While an individual electron can often be handled as an isolated point charge, an atom is a collection of electrons best described in terms of a number density function $U(\mathbf{r})$, where $\mathbf{r}$ is a position vector relative to the origin, here taken as the center of the atom. The total number of electrons contained in a volume element $\mathrm{d}V$ at position $\mathbf{r}$ of such an atom is $U(\mathbf{r})\,\mathrm{d}V$, while the total charge in this volume element is $e\,U(\mathbf{r})\,\mathrm{d}V$. Figure 2.4 shows a hypothetical two-dimensional projection of a possible electron density function along with a scattering event.

If an X-ray with wave-vector $\mathbf{k}_0$ scatters elastically from the charge element $e\,U(\mathbf{r})\,\mathrm{d}V$ to a new wave-vector $\mathbf{k}_f$, the scattering event is again characterized by the scattering vector $\mathbf{s}$ as in Section 2.2. The phase difference of the scattered X-ray, relative to an X-ray scattered with the same scattering vector $\mathbf{s}$ from the atom origin, is a function of the total path difference between the two X-rays. If the scattered waves are both observed at point $\mathbf{r}_P$, and $\|\mathbf{r_P}\| \gg \|\mathbf{r}\|$, then the path

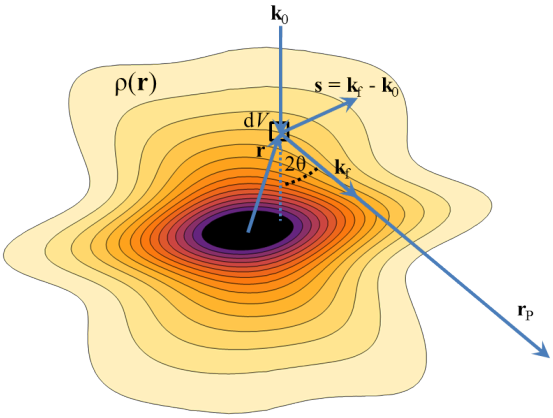

Figure 2.4: A schematic depiction of an X-ray with wave-vector $\mathbf{k}_0$ impinging on an isolated atom. The X-ray scatters elastically from the charge element $e\,U\,(\mathbf{r})\,\mathrm{d}V$ at position $\mathbf{r}$ to the new wave-vector $\mathbf{k}_f$.

difference can be approximated by considering only the spatial distance $\mathbf{r}$ between the two charge elements. Through geometric arguments, the phase difference is then $-2\pi\mathbf{r}\cdot\mathbf{s}$. It is much more convenient to adopt the time-invariant complex phasor notation and write the phase difference as $e^{-2\pi\imath\mathbf{r}\cdot\mathbf{s}}$. This allows the scattered wave amplitude as observed at $\mathbf{r}_P$, resulting from the superposition of the two scattered waves, to be written as $e\,U\,(\mathbf{r})\,e^{-2\pi\imath\mathbf{r}\cdot\mathbf{s}}\mathrm{d}V$. As mentioned at the end of Section 2.2, a factor including Thomson cross section and polarization effect has been suppressed for brevity.

The electron density function is extended in space, so the phase difference from all volume elements must be considered by integration. In this way, the scattered wave amplitude as a function of the scattering vector is

$$\varphi\,(\mathbf{s}) = \int U\,(\mathbf{r})\,e^{-2\pi\imath\mathbf{r}\cdot\mathbf{s}}\mathrm{d}V. \tag{2.4}$$

and can be recognized as the FT of the electron density $\mathcal{F}\,[U\,(\mathbf{r})]\,(\mathbf{s})$, explicitly specifying the functional dependence on $\mathbf{s}$, the scattering vector. This explicit notation is suppressed in further equations. This definition of the wave amplitude scattered from an isolated atom is

typically called the atomic form factor $f(\mathbf{s}) \equiv \varphi(\mathbf{s})$. If the atom is spherically symmetric, then the atomic electron density depends only on the magnitude of the position vector, $\|\mathbf{r}\| = r$, and the atomic form factor depends only on the magnitude of the scattering vector.

It should be mentioned that the treatment of the atom in this way assumes classical scattering. In reality, atoms are quantum objects with sharp absorption lines at well-defined energies, associated with intra-atomic electronic excitations. These absorption lines necessitate what is called *anomalous scattering* and dictate that the atomic form factor formally depends on *both* the scattering vector $\mathbf{s}$ and the energy of the incident X-rays $\hbar\omega$. This phenomena can be handled by introducing a perturbation to the amplitude and phase of the atomic form factor. The new anomalous atomic form factor can be written as

$$f_0(s, \hbar\omega) = f_0(s) + \Delta f'(\hbar\omega) + \imath \Delta f''(\hbar\omega), \tag{2.5}$$

where $f_0(s)$ represents the typical, spherically symmetric atomic form factor, while $\Delta f'(\hbar\omega)$ and $\imath\Delta f''(\hbar\omega)$ indicate the effect of anomalous scattering on the magnitude and phase of the form factor, respectively. Energy dependent values for $\Delta f'(\hbar\omega)$ and $\imath\Delta f''(\hbar\omega)$ for various isolated atoms and ions can be found tabulated in the *International Tables for Crystallography Volume C* [45] or, perhaps more conveniently, online [46].

Practically, the spherically symmetric atomic form factor is approximated analytically in the scattering vector range $0 < s < \frac{25}{2\pi}$ Å^{-1} as a sum of s dependent Gaussian functions following Cromer and Mann [47]. Using this approach, the atomic form factor can be can be written as

$$f(s) = \sum_{i=1}^{4} a_i e^{-b_i \frac{s^2}{4}} + c. \tag{2.6}$$

Equation 2.6 has been fit using spherically-averaged electron density maps computed with quantum theory for the most common isolated atoms and ions [48–50]. Tabulated values for a_i, b_i, and c are used throughout this work [45], without anomalous scattering corrections.

An example of the spherically symmetric atomic scattering factor of a nickel atom as represented by equation 2.6 is shown in Figure 2.5. For forward scattering, the scattering factor evaluates to the total number

of electrons in a nickel atom ($f\,(s=0)=28$). The scattering factor then decreases monotonically with increasing scattering vector s or scattering angle θ.

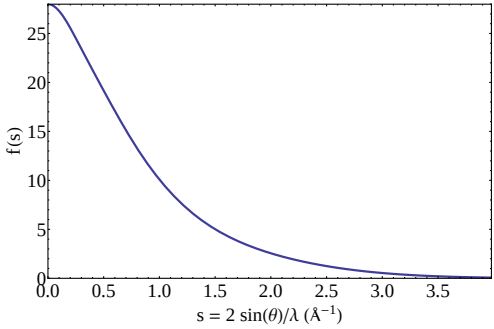

Figure 2.5: The spherically symmetric atomic form factor $f\,(s)$ of an isolated nickel atom, as approximated by equation 2.6

2.4 Defect free, spatially infinite crystals

In this section, a mathematical description for kinematic diffraction from spatially infinite (unbounded) perfect crystals is outlined. It is clear that truly infinite objects do not exist practically, but in the context of this work, a crystal can be considered "spatially infinite" if it is much larger than the coherence length of the probe radiation. For typical laboratory diffractometers, this is about 100 nm, while for synchrotron X-ray sources, the coherence length varies by beamline. While it may seem impractical a discussion of this type helps to introduce some general topics such as DS and RS lattices, Bragg's law, the structure factor of the unit cell, and the so-called powder averaging of the diffracted intensity distribution. In general these concepts alone are sufficient in some cases to interpret diffraction data.

2.4.1 Electron density

To mathematically represent the electron density of an infinite, perfect crystal, the first step is to represent a three-dimensionally periodic crys-

tal lattice. The Dirac delta distribution $\delta(\mathbf{r})$ facilitates this description, and it is useful to review some properties of these distributions:

$$\int_{-\infty}^{\infty} g(\mathbf{r})\,\delta(\mathbf{r}-\mathbf{T})\;\mathrm{d}V_{\mathbf{r}} = g(\mathbf{T}) \tag{2.7a}$$

$$\int_{-\infty}^{\infty} a\delta(\mathbf{r}-\mathbf{T})\;\mathrm{d}V_{\mathbf{r}} = a \tag{2.7b}$$

$$g(\mathbf{r}) * \delta(\mathbf{r}-\mathbf{T}) = \int_{-\infty}^{\infty} g(\boldsymbol{\tau})\,\delta(\mathbf{r}-\mathbf{T}-\boldsymbol{\tau})\;\mathrm{d}V_{\boldsymbol{\tau}} = g(\mathbf{r}-\mathbf{T})\,, \tag{2.7c}$$

where $*$ represents the convolution operation, a is a scalar, $\mathbf{T}$ is a real valued position vector, and $\mathrm{d}V_{\mathbf{r}}$ indicates that the integration is over volume elements with respect to the spatial coordinate $\mathbf{r}$.

Ewald conveniently represented a lattice function as an infinite sum of these distributions, where each term represents one lattice point and is translated by a scaled lattice vector, $u\mathbf{a}+v\mathbf{b}+w\mathbf{c}$ [22], where u, v, and w are integers. The lattice function is written with this description as

$$z(\mathbf{r}) \equiv \sum_{u=-\infty}^{\infty}\sum_{v=-\infty}^{\infty}\sum_{w=-\infty}^{\infty} \delta(\mathbf{r}-u\mathbf{a}-v\mathbf{b}-w\mathbf{c}) = \sum_{uvw}\delta(\mathbf{r}-\mathbf{r}_{uvw})\,, \tag{2.8}$$

and represents a three-dimensionally periodic lattice that is described by one of the 14 possible three-dimensional Bravais lattices. The lattice function in equation 2.8 evaluates to one of two values, either

$$z(\mathbf{r} \neq u\mathbf{a}+v\mathbf{b}+w\mathbf{c}) = 0$$

or

$$z(\mathbf{r} = u\mathbf{a}+v\mathbf{b}+w\mathbf{c}) = \delta(0)\,,$$

Further, each term in the lattice sum of equation 2.8 obeys the integration properties outlined in equations 2.7a, 2.7b, and 2.7c, properties that will be exploited in the following.

Equation 2.8 represents only a crystal *lattice*. To represent a spatially infinite crystal, the lattice must be "dressed" or tiled with scattering

potential; for X-ray scattering, this is electron density. The block used to dress the lattice is called the unit cell electron density, and contains n atoms. It can be represented as a sum of the electron densities $U_p(r)$ of each isolated, spherically symmetric atom p, translated by the position vector of the atom $\mathbf{r}_p = x_p\mathbf{a} + y_p\mathbf{b} + z_p\mathbf{c}$ where $x_p, y_p,$ andz_p are fractional coordinates. Using this approach, the electron density of the unit cell can be written as

$$\sum_{p=1}^{n} U_p\left(\|\mathbf{r} - \mathbf{r_p}\|\right). \tag{2.9}$$

The symmetry within the unit cell outlined in equation 2.9 is described by one of the 230 three-dimensional space groups. A spatially infinite crystal is then represented mathematically as the convolution of the unit cell and crystal lattice, written as

$$\rho(\mathbf{r}) = \sum_{p=1}^{n} U_p\left(\|\mathbf{r} - \mathbf{r_p}\|\right) * z(\mathbf{r}). \tag{2.10}$$

The convolution in equation 2.10 exploits the convolution property of the Dirac distributions shown in equation 2.7c to translate one unit cell to each lattice point, and creates a perfect, spatially infinite crystal. With this, the electron density can be written as

$$\rho(\mathbf{r}) = \sum_{uvw}\sum_{p=1}^{n} U_p\left(\|\mathbf{r} - \mathbf{r_p} - \mathbf{r_{uvw}}\|\right). \tag{2.11}$$

In the next section the elastic scattering behavior of this object is investigated.

2.4.2 Scattering

The wave amplitude elastically scattered from the object represented in equation 2.11 is found by the same process as outlined in Section 2.3. By integrating the product of the crystal electron density and the associated phasor term over all space, the scattered wave amplitude is written as the FT of equation 2.11, or as

$$\varphi(\mathbf{s}) = \mathcal{F}\left[\sum_{uvw}\sum_{p=1}^{n} U_p\left(\|\mathbf{r} - \mathbf{r_p} - \mathbf{r_{uvw}}\|\right)\right]. \tag{2.12}$$

Recalling that $\mathcal{F}\left[f\left(\|\mathbf{r}-\mathbf{a}\|\right)\right]=\mathcal{F}\left[f\left(r\right)\right]e^{-2\pi\imath\mathbf{a}\cdot\mathbf{s}}$, equation 2.12 can be written as

$$\varphi\left(\mathbf{s}\right)=\sum_{uvw}\sum_{p=1}^{n}\mathcal{F}\left[U_p\left(r\right)\right]e^{-2\pi\imath\mathbf{r}_p\cdot\mathbf{s}}e^{-2\pi\imath\mathbf{r}_{uvw}\cdot\mathbf{s}}. \tag{2.13}$$

However, $\mathcal{F}\left[U_p\left(r\right)\right]$ is the scattered amplitude from an isolated atom or the atomic form factor $f_p\left(s\right)$ as presented in equation 2.4 in Section 2.3, while $\sum_{p=1}^{n}\mathcal{F}\left[U_p\left(r\right)\right]e^{-2\pi\imath\mathbf{r}_p\cdot\mathbf{s}}$ represents the FT of the unit cell electron density in equation 2.9. This FT is usually called the structure factor of the unit cell $F\left(\mathbf{s}\right)$, and is defined as

$$F\left(\mathbf{s}\right)\equiv\sum_{p=1}^{n}\mathcal{F}\left[U_p\left(r\right)\right]e^{-2\pi\imath\mathbf{r}_p\cdot\mathbf{s}}=\sum_{p=1}^{n}f_p\left(s\right)e^{-2\pi\imath\mathbf{r}_p\cdot\mathbf{s}}. \tag{2.14}$$

With this definition, the scattered wave amplitude in equation 2.12 can be rewritten as

$$\varphi\left(\mathbf{s}\right)=F\left(\mathbf{s}\right)\sum_{uvw}e^{-2\pi\imath\mathbf{r}_{uvw}\cdot\mathbf{s}}. \tag{2.15}$$

The diffracted intensity distribution is the squared modulus of this complex wave amplitude, and can be written as

$$\begin{aligned}I\left(\mathbf{s}\right)=\left|\varphi\left(\mathbf{s}\right)\right|^2&=\left(F\left(\mathbf{s}\right)\sum_{uvw}e^{-2\pi\imath\mathbf{r}_{uvw}\cdot\mathbf{s}}\right)\left(F\left(\mathbf{s}\right)\sum_{uvw}e^{-2\pi\imath\mathbf{r}_{uvw}\cdot\mathbf{s}}\right)^*\\&=\left|F\left(\mathbf{s}\right)\right|^2\left(\sum_{uvw}e^{-2\pi\imath\mathbf{r}_{uvw}\cdot\mathbf{s}}\right)\left(\sum_{u'v'w'}e^{2\pi\imath\mathbf{r}_{u'v'w'}\cdot\mathbf{s}}\right)\\&=\left|F\left(\mathbf{s}\right)\right|^2\sum_{u'v'w'}\sum_{uvw}e^{-2\pi\imath\left(\mathbf{r}_{uvw}-\mathbf{r}_{u'v'w'}\right)\cdot\mathbf{s}},\end{aligned} \tag{2.16}$$

where the superscript * indicates the complex conjugate, and the sums in each factor are explicitly over *different* sets unit cell translation indices, either uvw or $u'v'w'$. The double lattice summation of phase terms in equation 2.16 can be transformed into a new RS lattice function following Guinier [51], defined as

$$Z\left(\mathbf{s}\right)\equiv\sum_{h=-\infty}^{\infty}\sum_{k=-\infty}^{\infty}\sum_{l=-\infty}^{\infty}\delta\left(\mathbf{s}-h\mathbf{a}^*-k\mathbf{b}^*-l\mathbf{c}^*\right)=\sum_{hkl}\delta\left(\mathbf{s}-\mathbf{s}_{hkl}\right), \tag{2.17}$$

where the triple sum is abbreviated $\sum_{hkl}$, and $h\mathbf{a}^* + k\mathbf{b}^* + l\mathbf{c}^*$ is defined as $\mathbf{s}_{hkl}$, or the scattering vector associated with the hkl RS lattice point. By convention, the integers h, k, and l are called Miller indices, and each $\mathbf{s}_{hkl}$ point is often called a Bragg point. The RS lattice vectors, $\mathbf{a}^*$, $\mathbf{b}^*$, and $\mathbf{c}^*$ are defined as cyclic cross products of the DS lattice vectors, normalized by the unit cell volume, and can be written explicitly as

$$\mathbf{a}^* \equiv \frac{\mathbf{b} \times \mathbf{c}}{(\mathbf{b} \times \mathbf{c}) \cdot \mathbf{a}}, \; \mathbf{b}^* \equiv \frac{\mathbf{c} \times \mathbf{a}}{(\mathbf{c} \times \mathbf{a}) \cdot \mathbf{b}}, \; \mathbf{c}^* \equiv \frac{\mathbf{a} \times \mathbf{b}}{(\mathbf{a} \times \mathbf{b}) \cdot \mathbf{c}}. \tag{2.18}$$

With this, the intensity distribution in equation 2.16 can be written as

$$I(\mathbf{s}) = |F(\mathbf{s})|^2 \sum_{hkl} \delta(\mathbf{s} - \mathbf{s}_{hkl}). \tag{2.19}$$

Typically this equation is separated into the sum of intensity contribution arising from each individual hkl Bragg point, and equation 2.19 is written as

$$I(\mathbf{s}) = \sum_{hkl} I_{hkl}(\mathbf{s}) \tag{2.20}$$

where

$$I_{hkl}(\mathbf{s}) = |F(\mathbf{s})|^2 \delta(\mathbf{s} - \mathbf{s}_{hkl}).$$

By equation 2.20, the diffracted intensity distribution in RS due to a spatially unbounded perfect crystal can be visualized as an infinite, periodic RS lattice of Dirac distributions, where each distribution is weighted by the squared magnitude of the structure factor of the unit cell, evaluated at the lattice point $\mathbf{s}_{hkl}$. The periodicity of the RS lattice describing the intensity distribution is dependent upon the DS lattice describing the crystal, while the total intensity weighting each lattice point is dependent upon the type and arrangement of atoms in the crystal unit cell.

2.4.3 Powder averaging

Equation 2.20 gives the diffracted intensity in three-dimensional RS resulting from a perfect, oriented, spatially infinite crystal. Materials

scientists are often more interested collections of many independently scattering crystals, such as a polycrystalline body or a powder. The following section will assume an ideal powder sample composed of the objects described in the previous section. In the context of this work an ideal powder is composed of many crystals showing a smooth uniform distribution of spatial orientations.

The diffracted intensity from such a powder represents the *average* intensity over all possible crystal orientations. Rather than averaging the electron density of the crystal as expressed in equation 2.11, the orientation average is typically performed on the diffracted intensity distribution itself, as expressed in equation 2.20. The intensity distribution obtained from a powder then retains no information on the direction of the scattering vector $\mathbf{s}$, and depends only on its magnitude s.

The averaging is done by evaluating the surface integral of equation 2.20 over a sphere with constant radius s. This is easiest in spherical coordinates, where the differential surface element is $\mathrm{d}S = s^2 \sin\theta \, \mathrm{d}\theta \, d\phi$. The integration surface is typically called the powder diffraction sphere. The maximum radius of the sphere is determined by the wavelength of radiation used, and gives the portion of reciprocal space that can be explored with a given diffraction experiment. It is found by setting the scattering angle to 180°, $s_{max} = 2/\lambda$. Within the powder integration, a weighting factor of $1/4\pi s^2$ is used to account for the decreasing likelihood of a diffraction event occurring as s increases. This weighting term is often called the Lorentz factor, but it is not usually maintained in this form following integration. The powder intensity is then written as

$$\begin{aligned} I(s) &= \frac{1}{4\pi s^2} \iint_S I(\mathbf{s}) \, \mathrm{d}S \\ &= \frac{1}{4\pi s^2} \int_0^{2\pi} \int_0^{\pi} I(\mathbf{s}) \, s^2 \sin\theta \, \mathrm{d}\theta \, \mathrm{d}\phi \\ &= \frac{1}{4\pi} \sum_{hkl} \int_0^{2\pi} \int_0^{\pi} \delta(\mathbf{s} - \mathbf{s}_{hkl}) \left|F(\mathbf{s})\right|^2 \sin\theta \, \mathrm{d}\theta \, \mathrm{d}\phi \end{aligned} \tag{2.21}$$

The Dirac distribution $\delta(\mathbf{s} - \mathbf{s}_{hkl})$, can be rewritten in spherical coordinates as $\frac{1}{s^2 \sin\theta} \delta(s - s_{hkl}) \, \delta(\theta - \theta_{hkl}) \, \delta(\phi - \phi_{hkl})$. With this, the

integration on θ and ϕ is analytic, and equation 2.21 can be rewritten as

$$\begin{aligned} I(s) &= \frac{1}{4\pi} \sum_{hkl} \int_0^{2\pi} \int_0^{\pi} \delta(\mathbf{s} - \mathbf{s}_{hkl}) |F(\mathbf{s})|^2 \sin\theta \, \mathrm{d}\theta \, \mathrm{d}\phi \\ &= \frac{1}{4\pi} \sum_{hkl} \int_0^{2\pi} \int_0^{\pi} \frac{|F(\mathbf{s})|^2}{s^2 \sin\theta} \delta(s - s_{hkl}) \delta(\theta - \theta_{hkl}) \delta(\phi - \phi_{hkl}) \sin\theta \, \mathrm{d}\theta \, \mathrm{d}\phi \\ &= \frac{1}{4\pi s^2} \sum_{hkl} \delta(s - s_{hkl}) |F(\mathbf{s}_{hkl})|^2 \end{aligned} \tag{2.22}$$

This gives the result that the diffracted intensity of an ideal powder of perfect, spatially infinite crystals is a sum of Dirac delta distributions with positions given by the RS lattice. The diffracted intensity is *infinite* when $s = s_{hkl}$, while it is exactly zero at all other points, when $s \neq s_{hkl}$, that is

$$I(\mathbf{s}) = \begin{cases} \delta(0) \frac{|F(\mathbf{s}_{hkl})|^2}{4\pi s^2}, & \text{if } \mathbf{s} = h\mathbf{a}^* + k\mathbf{b}^* + l\mathbf{c}^* = \mathbf{s}_{hkl} \\ 0, & \text{if } \mathbf{s} \neq \mathbf{s}_{hkl} \end{cases}. \tag{2.23}$$

This is not particularly useful, but is a direct result of considering a powder of perfect infinite crystals completely bathed in X-rays.

Speaking more empirically, it is known that instrumental aberrations and deviations from perfect crystallinity both act as convolutions to smear the diffracted intensity [12], leading to measured powder diffraction data that never contains Dirac delta distributions. If an empirical profile function $P(s)$ is adopted to approximate this effect, the smeared powder intensity distribution can be written as

$$I_{\text{empirical}}(s) = P(s) * I(s) = \sum_{hkl} \frac{|F(\mathbf{s}_{hkl})|^2}{4\pi s_{hkl}^2} P(s - s_{hkl}). \tag{2.24}$$

Physically this implies that the total observable intensity of a Bragg point is finite and proportional to the squared magnitude of the structure factor evaluated at the Bragg point.

The factor of $1/s_{hkl}^2$ is a different form of the Lorentz factor, resulting from the convolution with an empirical profile. It is more frequently expressed in terms of the scattering angle as $\lambda^2/4\sin^2(\theta_{hkl})$. Strictly

speaking this form of the Lorentz factor is only accurate under the assumptions of an ideal powder of perfect, spatially infinite crystals. Defects and spatial boundedness entail a different form of equation 2.20 and a different approach to powder integration, leading to a different Lorentz factor. This is reviewed in Sections 2.5 and 2.6.

Each delta distribution in equation 2.22 or each profile function in equation 2.24 is located at the scattering vector s_{hkl}. Recalling the definition of the scattering vector from Section 2.2, this location can be converted to the more observable scattering angle through the relationship $s_{hkl} = \frac{2\sin\theta_{hkl}}{\lambda}$. Recognizing that the nature of the FT operation dictates that the hkl Bragg point corresponds to the distances between (hkl) set of crystal planes implies that $s_{hkl} = 1/d_{hkl}$; where d_{hkl} is the spacing between the (hkl) set of crystal planes. This in turn leads to Bragg's law $\lambda = 2d_{hkl}\sin\theta_{hkl}$, relating inter-atomic distances to measurable quantities in the observed powder diffraction pattern [5].

Two example powder intensity distributions, simulated assuming metallic nickel as outlined in Section 2.1, are shown in Figure 2.6. Both were computed by assuming unpolarized incident radiation, requiring a polarization factor given by equation 2.3 with $Q = 0$. A wavelength of 1.54059 Å was assumed, as it is a common condition in laboratory diffraction instruments where characteristic copper radiation is often used. In Figure 2.6a, equation 2.22 was used, and each Delta distributions representing a Bragg peak is shown with an artificial width of 0.5° 2θ and a height proportional to the relative intensity of the Bragg peak. In Figure 2.6b, the unrealistic intensity distribution presented in Figure 2.6a has been empirically broadened as per equation 2.24 by a Cauchy distribution with unit area and FWHM of 1° 2θ. The symmetry of the nickel DS lattice dictates that a number of Bragg peaks (e.g. the {111} family) are degenerate in both powder position s_{hkl} and integrated intensity. The symmetry of the nickel unit cell entails that some Bragg peaks (e.g. the {110} family) lead to a structure factor that is exactly zero, causing systematic absences in the intensity distributions shown in Figure 2.6.

The representation of the diffracted intensity distribution presented in Figure 2.6b and the mathematics behind it form the fundamental basis for much of standard diffraction data analysis. While analysis

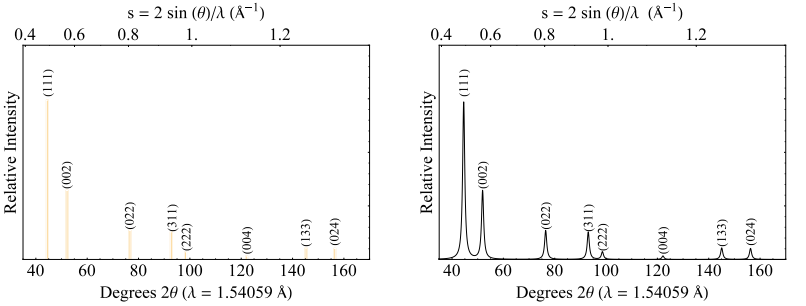

(a) Dirac profiles

(b) Cauchy profiles

Figure 2.6: The diffracted intensity distributions due to an ideal powder of perfect, spatially infinite nickel crystals is shown, assuming unpolarized copper $K\alpha_1$ radiation, leading to a polarization factor $\frac{1+\cos 2\theta}{2}$, as per equation 2.3. Bragg peaks are either shown as Dirac distribution with an artificial width of 0.5° 2θ, as per equation 2.22, or as Cauchy distributions with a FWHM of 1° 2θ, as per equation 2.24.

of this kind has been hugely and undeniably successful at furthering material science, it was highlighted in Section 1.2 that the intrinsic assumptions on which it is based can be limiting when characterizing nanomaterials [16]. It is with these limiting assumptions in mind that the next section is presented, focusing on a physical representation of line-profile shapes due to the finite spatial extent of crystals.

2.5 Defect free, spatially finite crystals

This section begins by acknowledging that real crystals are never perfect nor spatially infinite, but are always finite objects. In the context of this work, a spatially finite crystal that scatters coherently is called a coherently scattering domain (CSD), or often just a domain. In the context of real samples, a domain can represent a mosaic block within a larger polycrystalline particle, a individual crystal within a powder, or an individual grain in a polycrystalline monolith. The only important point is that the atoms within each domain scatter *coherently* (wave amplitudes add), while the domains themselves scatter *independently*

(intensities add). Gelisio and Scardi studied the effect upon diffracted intensity of positional and rotational correlation between adjacent domains, finding that for domains larger than just a few nanometers domain-domain interference effects were negligible with only a slight degree of misorientation between domains, possibly only detectable by advanced synchrotron light sources [52].

Many authors have sought to describe the diffraction effect of the finite spatial extent of a CSD. Scherrer developed the so-called Scherrer formula. In 1918 he suggested that the FWHM of the diffraction line profile, in units of the scattering vector, is inversely proportionate to the thickness of the crystal [17]. This was extended in 1942 by Stokes and Wilson, who derived a strategy (and several formulas) for directly computing the anisotropic line-profiles due to finite crystals with various morphologies and arbitrary atomic structure [23]. This has only recently been employed to directly compute line-profile shapes [20, 26–28]. The following section reviews some of these strategies and offers some novel extensions.

2.5.1 Electron density

To model spatially finite crystals, it is convenient to directly modify the spatially infinite electron density represented in equation 2.10. In 1940, Ewald proposed the use of a shape function for this modification [22], piecewise defined as either 1 inside or 0 outside the shape volume V_c, written as

$$\sigma(\mathbf{r}) = \begin{cases} 1, & \text{if } \mathbf{r} \in V_c \\ 0, & \text{if } \mathbf{r} \notin V_c \end{cases}. \tag{2.25}$$

Applying $\sigma(\mathbf{r})$ to the electron density function must be done with forethought, as the mathematical route employed has a direct impact on the surface termination of the domain, as pointed out by Ino and Minami [13]. If the shape function is applied after the lattice has been tiled with electron density, as proposed by Patterson and Ewald, the electron density is written [22, 53]

$$\rho(\mathbf{r}) = \left(\sum_{p=1}^{n} U_p \left(\|\mathbf{r} - \mathbf{r_p}\| \right) * z(\mathbf{r}) \right) \sigma(\mathbf{r}), \tag{2.26}$$

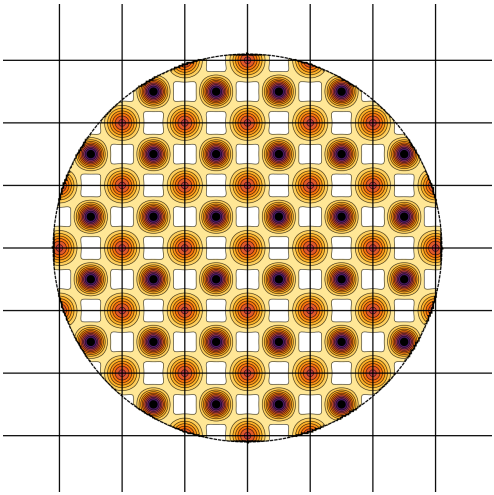

Figure 2.7: When the shape function acts on the infinite crystal electron density as in equation 2.26 the resulting spatially finite crystal has a "hard" boundary.

and the resulting density function represents the spatially infinite electron density cut abruptly at the shape function boundaries, as seen in Figure 2.7. Using this description, some atoms with local origins completely *outside* the domain volume V_c contribute electron density to the finite crystal, while the electron density of surface atoms with local origins *inside* V_c is suddenly cut off. Although it may seem unphysical, this description is sufficiently accurate for large domains to a first approximation, where the fraction of surface atoms is small [13, 54].

An alternative approach was proposed by Hosemann and Bagchi. First the shape function is applied to the lattice, which is then dressed or tiled with the unit cell electron density. With such an approach the domain electron density is written as [55]

$$\rho\left(\mathbf{r}\right) = \sum_{p=1}^{n} U_p\left(\left\|\mathbf{r} - \mathbf{r_p}\right\|\right) * \Big(z\left(\mathbf{r}\right)\sigma(\mathbf{r})\Big). \tag{2.27}$$

This density function represents the complete electron density from all

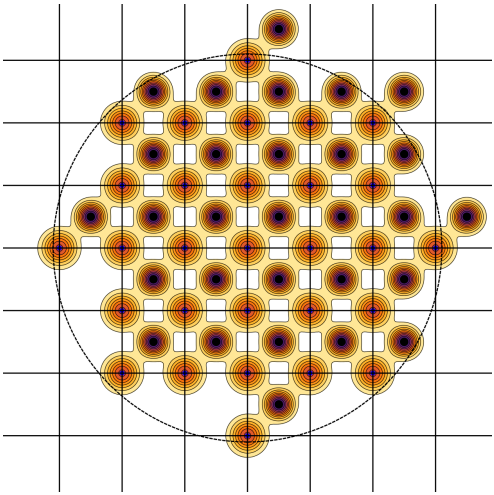

Figure 2.8: When the shape function acts on the infinite crystal electron density as in equation 2.27 the resulting spatially finite crystal includes only electron density from the atoms within unit cells associated with a lattice point within the crystal volume.

atoms in each unit cell associated with a lattice point within V_c, as seen in Figure 2.8. A domain described in this way also shows some strange features. Some atoms with local origins outside V_c are included fully in the domain, while some atoms with local origins fully inside V_c are not included, as the unit cell they belong to was removed by the shape function.

Ino and Minami suggested that the atom be considered the most fundamental building block of a finite crystal, thus they proposed a domain electron density function where the shape function removes all electron density from all atoms with a local origin outside V_c, but that retains the complete electron density of all atom with local origins inside V_c, even if the diffuse electron density extends beyond the borders of V_c [13]. An example is presented in Figure 2.9. Mathematically, this requires translating the lattice function, rather than the atoms, by the fractional coordinate $\mathbf{r}_p$ of the p^{th} atom in the unit cell. The translated lattice function is then convolved with the isolated atom electron

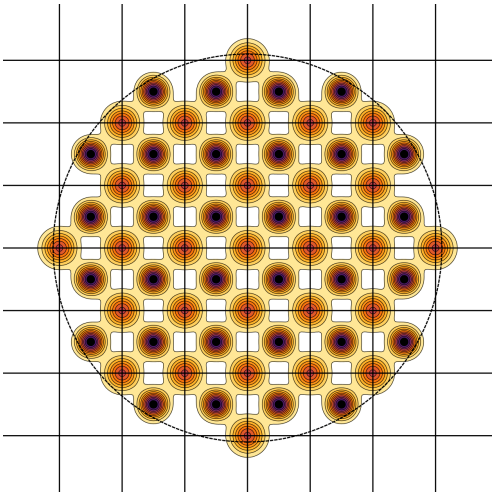

Figure 2.9: When the shape function acts on the infinite crystal electron density as in equation 2.28 the resulting spatially finite crystal retains all electron density from all atoms with local origin inside the crystal volume.

density of the p^{th} atom $U_p(r)$. A sum is then taken over all atoms in the unit cell. Following this route, the electron density is written [13]

$$\rho(\mathbf{r}) = \sum_{p=1}^{n} U_p(r) * \Big(z(\mathbf{r} - \mathbf{r}_p)\, \sigma(\mathbf{r}) \Big). \tag{2.28}$$

This approach is the most intuitive and physically realistic for describing the shape of domains in nanomaterials, as it most accurately reproduces the "intended" shape of the domain as represented by the shape function. It does not introduce any unphysical features at the surface of the domain, such as those seen in Figure 2.7 or Figure 2.8. Thus equation 2.28 is the preferred form of the domain electron density for the following derivation of the intensity distribution. It should be pointed out that the mathematical definition of the finite crystal *does* have an impact on the form of the diffracted intensity equation. This point is discussed only briefly in the next section; a more detailed discussion was presented by Ino and Minami [13].

2.5.2 Scattering

Again, the scattered wave amplitude is represented by the FT of the electron density. Equation 2.28 can be transformed and the RS lattice in equation 2.17 can be substituted. Following this approach the scattered wave amplitude can be written as

$$\begin{aligned}\varphi(\mathbf{s}) &= \mathcal{F}\left[\sum_{p=1}^{n} U_p(r) * \left(z(\mathbf{r}-\mathbf{r}_p)\,\sigma(\mathbf{r})\right)\right] \\ &= \sum_{p=1}^{n} \mathcal{F}\left[U_p(r)\right]\left(\mathcal{F}\left[z(\mathbf{r}-\mathbf{r}_p)\right] * \mathcal{F}\left[\sigma(\mathbf{r})\right]\right) \\ &= \sum_{p=1}^{n} f_p(s)\left(\left(Z(\mathbf{s})\,e^{-2\pi\imath\mathbf{r}_p\cdot\mathbf{s}}\right) * \mathcal{F}\left[\sigma(\mathbf{r})\right]\right). \end{aligned} \tag{2.29}$$

By making the definition $S(\mathbf{s}) \equiv \mathcal{F}[\sigma(\mathbf{r})]$ equation 2.29 can be rewritten as

$$\begin{aligned}\varphi(\mathbf{s}) &= \sum_{p=1}^{n} f_p(s)\left(\left(Z(\mathbf{s})\,e^{-2\pi\imath\mathbf{r}_p\cdot\mathbf{s}}\right) * S(\mathbf{s})\right) \\ &= \sum_{p=1}^{n} f_p(s)\left(\sum_{hkl} e^{-2\pi\imath\mathbf{r}_p\cdot\mathbf{s}_{hkl}} S(\mathbf{s}-\mathbf{s}_{hkl})\right) \\ &= \sum_{hkl}\sum_{p=1}^{n} f_p(s)\,e^{-2\pi\imath\mathbf{r}_p\cdot\mathbf{s}_{hkl}} S(\mathbf{s}-\mathbf{s}_{hkl}). \end{aligned} \tag{2.30}$$

The sum $\sum_{p=1}^{n} f_p(s)\,e^{-2\pi\imath\mathbf{r}_p\cdot\mathbf{s}_{hkl}}$ in equation 2.30 is similar to structure factor outlined in Section 2.4.2 and written in equation 2.14, but here it depends on *both* the scattering vector magnitude s and the location of the Bragg point $\mathbf{s}_{hkl}$. This summation is here called the IM structure factor and identified as $F(s, \mathbf{s}_{hkl})$, after Ino and Minami [13]. The dual dependence is a result of the new definition of the electron density function (equation 2.28). By substituting $F(s, \mathbf{s}_{hkl})$ into equation 2.30 the scattered wave amplitude can be written as

$$\varphi(\mathbf{s}) = \sum_{hkl} F(s, \mathbf{s}_{hkl})\, S(\mathbf{s}-\mathbf{s}_{hkl}). \tag{2.31}$$

The scattered wave amplitude is a sum in RS of the FT of the shape function translated to each Bragg point and weighted by the IM structure factor. The squared magnitude of equation 2.31 represents the diffracted intensity distribution, and can be written as

$$I(\mathbf{s}) = |\varphi(\mathbf{s})|^2 = \left(\sum_{hkl} F(s, \mathbf{s}_{hkl})\, S(\mathbf{s} - \mathbf{s}_{hkl})\right)\left(\sum_{h'k'l'} F(s, \mathbf{s}_{h'k'l'})\, S(\mathbf{s} - \mathbf{s}_{h'k'l'})\right)^*. \tag{2.32}$$

Where each sum is explicitly over different sets of Miller incices, either hkl or $h'k'l'$. The product can be grouped into the sum of two different products: those where $hkl = h'k'l'$ and those where $hkl \neq h'k'l'$, allowing equation 2.32 to be re-written as

$$I(\mathbf{s}) = \sum_{hkl} |F(s, \mathbf{s}_{hkl})\, S(\mathbf{s} - \mathbf{s}_{hkl})|^2 + \sum_{hkl \neq h'k'l'} \sum F(s, \mathbf{s}_{hkl})\, F(s, \mathbf{s}_{h'k'l'})^* S(\mathbf{s} - \mathbf{s}_{hkl})\, S(\mathbf{s} - \mathbf{s}_{h'k'l'})^*. \tag{2.33}$$

The second group of terms in equation 2.33 where $hkl \neq h'k'l'$ is not necessarily zero. Since $S(\mathbf{s})$ generally has spatial extent (it is not a Delta distribution), $S(\mathbf{s} - \mathbf{s}_{hkl})$ and $S(\mathbf{s} - \mathbf{s}_{h'k'l'})^*$ could overlap if the hkl and $h'k'l'$ Bragg points are close in RS. It would be convenient however to ignore the second group of terms in equation 2.33, as it is much too computationally expensive in its full form.

The approach shown so far in this section intrinsically assumes that the shape function and lattice function have coincident origins. A special case of equation 2.33 exists, where the domain under investigation is considered as an "average," constructed by considering a uniform distribution of all relative shape function origins. That is, equation 2.33 is worked out again by considering a shape function with an arbitrary shift $\mathbf{t}$, re-written as $\sigma(\mathbf{r} - \mathbf{t})$. By integrating over all $\mathbf{t}$, it can be said that the $hkl \neq h'k'l'$ terms in equation 2.33 are exactly zero. This is the so called "random shift treatment" or the "ξ-average" as outlined by Ino and Minami or Hosemann and Bagchi, respectively [13, 55].

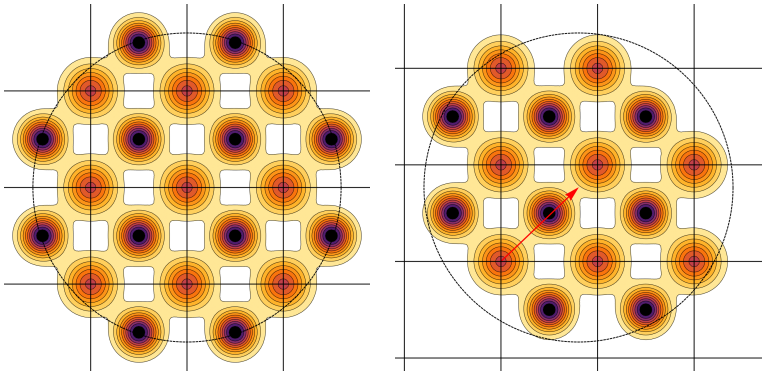

(a) no shift (b) random shift

Figure 2.10: Schematic projections of the electron density from two domains cut with the same shape function with different relative shape function translations.

In general the domain electron density as expressed in equation 2.28 is *not invariant* under a translation of the shape function by $\mathbf{t}$. Two crystals formed by applying otherwise identical shape functions can show different surface termination, and even a different number of scattering centers or atoms, due to a different choice of shape function origin. Physically the averaging over all shits acts to "blur" the surface of the domain, dictating that the real domain under consideration consists of an average of all possible surface terminations. This point is highlighted in Figure 2.15, which shows two distinct finite crystals, cut from the same infinite crystal by the same shape function with different relative displacements.

As an additional point, with increasing domain size, $S(\mathbf{s})$ becomes more spatially compact, and as a result the cross terms in equation 2.33 become increasingly negligible. This was explicitly highlighted by Guinier [51], but it is a generalization of the Scherrer formula [17].

Thus, if the domain has no specific preferred surface termination, or the domain is sufficiently large, the cross terms in equation 2.33 where $hkl \neq h'k'l'$ can safely be ignored. Equation 2.33 can be re-written as

$$I(\mathbf{s}) = \sum_{hkl} \left| F(s, \mathbf{s}_{hkl})\, S(\mathbf{s} - \mathbf{s}_{hkl}) \right|^2 \tag{2.34}$$

and visualized as a RS lattice where each *hkl* Bragg point is locally represented by what is called here the *shape profile function* $|S(\mathbf{s})|^2$, weighted by the squared magnitude of the IM structure factor $|F(s, \mathbf{s}_{hkl})|^2$.

As pointed out earlier, the IM structure factor in equation 2.34 is functionally dependent on *both* the Bragg position of the peak $\mathbf{s}_{hkl}$ *and* the scattering vector magnitude s. As a result, the weighting *varies across the breadth of the shape profile function.* This can lead to an asymmetry and *apparent shift* out of Bragg position [13]. The direction and magnitude of this shift and the amount of asymmetry both depend heavily on the behavior of $F(s, \mathbf{s}_{hkl})$ (the atomic structure) and the width of the profile (the microstructure). Holding other factors constant, the shift is generally inversely proportionate to the domain size and proportionate to the unit cell size [13].

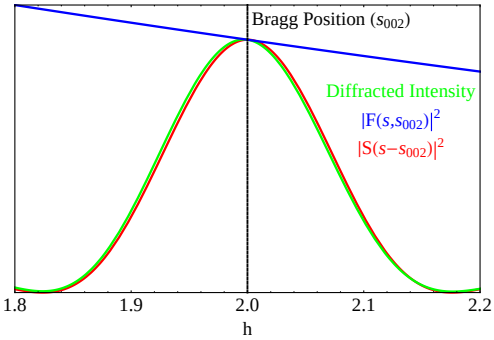

Figure 2.11: The $h00$ section of RS, showing the diffracted intensity, shape profile function $|S(\mathbf{s} - \mathbf{s}_{hkl})|^2$, and squared IM structure factor $|F(s, \mathbf{s}_{hkl})|^2$ from the $h00$ section of RS, simulated by assuming a spherical domain of fcc nickel with a diameter of 10 nm. The asymmetry and shift in the 200 profile is highlighted. All function values have been normalized by their value at $h = 2$ to facilitate plotting on the same scale.

Figure 2.11 highlights this effect, assuming a 10 nm spherical domain of fcc nickel as outlined in Section 2.1. The squared magnitude of

the IM structure factor, the shape profile function, and the diffracted intensity distribution are shown considering the $h00$ section of RS. To be clear, the diffracted intensity plotted in Figure 2.11 results from choosing equation 2.28 to represent the domain electron density.

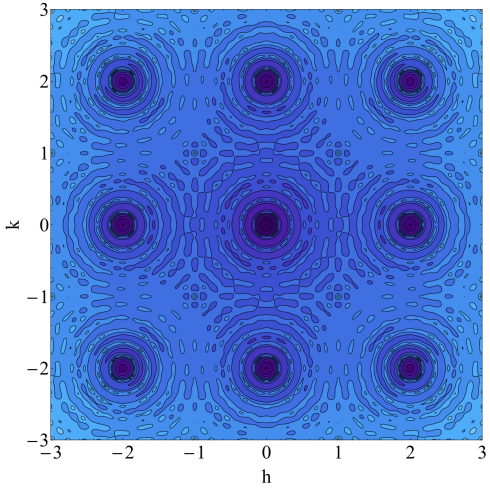

Figure 2.12: A schematic of the diffracted intensity map from the $hk0$ section of RS from a 10 nm domain of fcc nickel. Colors and contours represent logarithmic changes in intensity, to highlight subtle features.

Putting it all together, equation 2.34 allows for the calculation of the diffracted intensity in RS of a spatially finite, oriented, perfect domain with an "averaged" surface termination. A schematic of the diffracted intensity from the $hk0$ section of RS due to a 10 nm domain of fcc nickel is shown as a log contour plot in Figure 2.12. Equation 2.34 was used directly without employing any empirical profile functions. It is apparent that each Bragg spot is itself spherically *asymmetric*, while the entire intensity map shows the symmetry of the $m\bar{3}m$ Laue-class, inherited from the parent DS lattice.

2.5.3 Shape profile function

The shape profile function $I_{V_{hkl}}(\mathbf{s}) \equiv |S(\mathbf{s}-\mathbf{s}_{hkl})|^2$ in equation 2.34 has been revisited many times. It is the direct result of using a shape function $\sigma(\mathbf{r})$ to describe a finite crystal. First proposed by Ewald in 1940 [22], the shape function was later employed by Stokes and Wilson to derive a general strategy and several formulas for modeling anisotropic line-profiles resulting from nonspherical domain morphologies [23].

Recalling the definition of $S(\mathbf{s})$ can help shed some light on the physical meaning of $I_{V_{hkl}}(\mathbf{s})$, which can be re-written as

$$\begin{aligned} I_{V_{hkl}}(\mathbf{s}) &= |S(\mathbf{s}-\mathbf{s}_{hkl})|^2 = S(\mathbf{s}-\mathbf{s}_{hkl})\, S(\mathbf{s}-\mathbf{s}_{hkl})^* \\ &= \mathcal{F}\left[\sigma(\mathbf{r})e^{-2\pi\imath\mathbf{r}\cdot\mathbf{s}_{hkl}}\right] \mathcal{F}\left[\sigma(\mathbf{r})e^{2\pi\imath\mathbf{r}\cdot\mathbf{s}_{hkl}}\right] \\ &= \mathcal{F}\left[\left(\sigma(\mathbf{r})e^{-2\pi\imath\mathbf{r}\cdot\mathbf{s}_{hkl}}\right) * \left(\sigma(\mathbf{r})e^{2\pi\imath\mathbf{r}\cdot\mathbf{s}_{hkl}}\right)\right] \\ &= \mathcal{F}\left[\left(\sigma(\mathbf{r}) * \sigma(\mathbf{r})\right) e^{-2\pi\imath\mathbf{L}\cdot\mathbf{s}_{hkl}}\right]. \end{aligned} \tag{2.35}$$

In other words, $I_{V_{hkl}}(\mathbf{s})$ represents FT of the *autocorrelation* or *self-convolution* of the shape function, with an additional phase term associated with the translation to the *hkl* Bragg point. This self-convolution can be explicitly defined as

$$\sigma(\mathbf{r}) * \sigma(\mathbf{r}) = \int_{-\infty}^{\infty} \sigma(\mathbf{r})\sigma(\mathbf{r}-\mathbf{L})\,\mathrm{d}V_{\mathbf{r}} \equiv A(\mathbf{L}). \tag{2.36}$$

Such a self-convolution has been called the common volume function (CVF), as it is conveniently envisioned as the common volume between two identical objects where one (the domain "ghost," $\sigma(\mathbf{r}-\mathbf{L})$) is translated relative to the other (the domain, $\sigma(\mathbf{r})$) by the vector $\mathbf{L}$, following the work of Stokes and Wilson [23]. A schematic depiction of this physical meaning behind the CVF is shown in Figure 2.13; both a square and circle shape function and their ghosts are shown for various displacement vectors $\mathbf{L}$. The common area between the two shapes is also highlighted in red, and the CVF is plotted for each.

This definition is used to rewrite equation 2.35 as

$$\begin{aligned} I_{V_{hkl}}(\mathbf{s}) &= \mathcal{F}\left[A(\mathbf{L})\, e^{-2\pi\imath\mathbf{L}\cdot\mathbf{s}_{hkl}}\right] \\ &= \int_{-\infty}^{\infty} A(\mathbf{L})\, e^{-2\pi\imath\mathbf{L}\cdot(\mathbf{s}-\mathbf{s}_{hkl})}\,\mathrm{d}V_{\mathbf{L}}. \end{aligned} \tag{2.37}$$

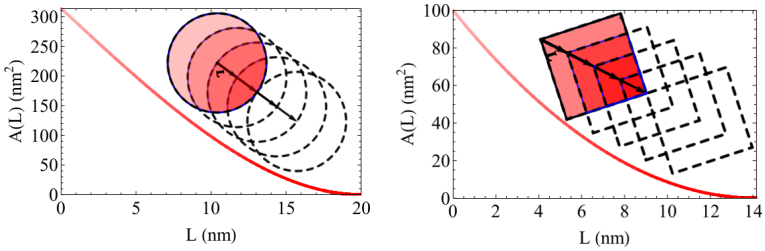

(a) Circle, 10 nm radius

(b) Square, 10 nm side length

Figure 2.13: Two-dimensional schematics highlighting the physical meaning behind the CVF for two different shapes. The shape function is represented by a solid boundary, while the ghost is represented by a dashed line. The common area (analogous to the common volume) is enclosed by a blue line and shaded different tints of red depending on the length of the autocorrelation vector **L**.

Much work has been done outlining analytic expressions for the CVF of basic shapes. As an example, the expression for a sphere of diameter D depends only on the magnitude of **L**, and can be written in a volume normalized form as

$$A(L) = \left(1 - \frac{3L}{2D} + \frac{L^3}{2D^3}\right). \tag{2.38}$$

Figure 2.15 shows a plot of this function and its FT for a sphere with a diameter of 10 nm. Expressions for $A(\mathbf{L})$ have also been derived for other regular polyhedrons including cubes, tetrahedrons, octahedron [23], cylinders [56], and hexagonal prisms [57]. Leonardi *et al.* have worked out a general algorithm for computing the CVF for any polyhedron shape, including hollow objects, tripods and tetrapods [58]. By using the CVF approach, the line-profile component associated with nearly any finite crystal shape and size can be computed directly from physical models without the need to use any empirical peak-shaped functions.

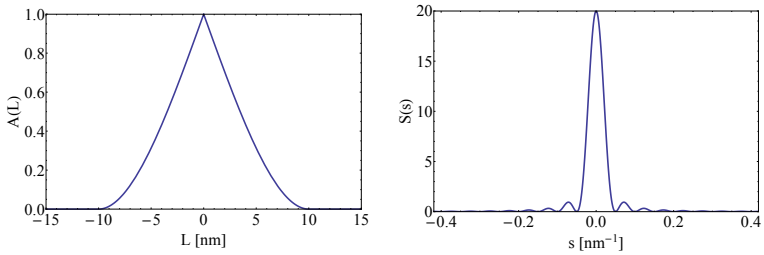

(a) CVF (b) Shape profile function

Figure 2.14: CVF and shape profile function associated with a sphere with a diameter of 10 nm

2.5.4 Polydispersed shape profile function

It is likely that the domains of interest are not characterized by identical shapes but rather show some distribution in the size parameters describing the shape. If the structure of the lattice and the unit cell are assumed to be uncorrelated with the domain size, such a situation can be handled by suitably modifying $S(\mathbf{s})$ and directly substituted it into equation 2.34.

Scardi and Leoni addressed such a situation by considering a general distribution weighted shape profile function for any arbitrary distribution of objects *described by one length parameter* [26], but it is possible to generalize such an approach to objects with any number of length parameters. The first step is to recognize that the shape function $\sigma(\mathbf{r})$ is actually dependent on both the spatial coordinate vector $\mathbf{r}$ and the parameters defining the boundaries of the volume V_c, here represented as the entries of the vector $\mathbf{D}$. In general, the dimension of the vector $\mathbf{D}$ depends on the nature of V_c.

For a spherical shape function, $\mathbf{D}$ is unidimensional and contains only information on the diameter D of the sphere; in this case the shape function is written

$$\sigma(r, D) = \begin{cases} 1, & \text{if } r \leq D \\ 0, & \text{if } r > D \end{cases}. \tag{2.39}$$

For parallelepiped shape function, $\mathbf{D}$ contains three entries, the par-

allelepiped edge lengths. If a simple case is taken where the parallelepiped is aligned with edges parallel to the three principle Cartesian axes, then $\mathbf{D} = (L_x, L_y, L_z)$, and the shape function is written as

$$\sigma\left(\mathbf{r} = x\hat{\mathbf{x}} + y\hat{\mathbf{y}} + z\hat{\mathbf{z}}, \mathbf{D} = (L_x, L_y, L_z)\right) = \begin{cases} 1, & \text{if } (0 \leq x \leq L_x) \wedge (0 \leq y \leq L_y) \wedge (0 \leq z \leq L_z) \\ 0, & \text{if } (0 > x > L_x) \vee (0 > y > L_y) \vee (0 > z > L_z)\,. \end{cases} \tag{2.40}$$

This formalism can however be applied for more complex objects with any number of size parameters. The new general shape function is then written $\sigma(\mathbf{r}, \mathbf{D})$, while the autocorrelation of this shape function, or the CVF, can be rewritten as $A(\mathbf{L}, \mathbf{D})$. The FT of this new CVF represents the shape profile function of a perfect, spatially finite crystal described by the vector of length parameters $\mathbf{D}$, and can be written as

$$I_{V_{hkl}}(\mathbf{s}, \mathbf{D}) = \mathcal{F}\left[A(\mathbf{L}, \mathbf{D})\, e^{-2\pi\imath \mathbf{L}\cdot\mathbf{s}_{hkl}}\right] = \int_{-\infty}^{\infty} A(\mathbf{L}, \mathbf{D})\, e^{-2\pi\imath \mathbf{L}\cdot(\mathbf{s}-\mathbf{s}_{hkl})}\, \mathrm{d}V_{\mathbf{L}} \tag{2.41}$$

For a polydisperse system, the presence of domains with the same shape but different size parameters $\mathbf{D}$ can be described by a multivariate probability density distribution of the length parameters $g(\mathbf{D})$. The shape profile function arising in such a system is the *volume weighted* ensemble-averaged profile considering all different sizes. The new shape profile function is written as

$$\begin{aligned} I_{V_{hkl}}(\mathbf{s}) &= \frac{\int_0^\infty I_{V_{hkl}}(\mathbf{s}, \mathbf{D})\, g(\mathbf{D}) V_c(\mathbf{D})\, \mathrm{d}\mathbf{D}}{\int_0^\infty g(\mathbf{D}) V_c(\mathbf{D})\, \mathrm{d}\mathbf{D}} \\ &= \frac{\int_0^\infty \mathcal{F}\left[A(\mathbf{L}, \mathbf{D})\, e^{-2\pi\imath \mathbf{L}\cdot\mathbf{s}_{hkl}}\right] g(\mathbf{D}) V_c(\mathbf{D})\, \mathrm{d}\mathbf{D}}{\int_0^\infty g(\mathbf{D}) V_c(\mathbf{D})\, \mathrm{d}\mathbf{D}} \end{aligned} \tag{2.42}$$

Where $V_c(\mathbf{D})$ represents the volume of a domain with shape parameters $\mathbf{D}$. Substituting for $\mathcal{F}[A(\mathbf{L}, \mathbf{D})]$ and defining the volume weight function as $w(\mathbf{D}) \equiv g(\mathbf{D}) V_c(\mathbf{D})$ gives

$$I_{V_{hkl}}(\mathbf{s}) = \frac{\int_0^\infty \int_{-\infty}^\infty A(\mathbf{L}, \mathbf{D})\, e^{-2\pi\imath \mathbf{L}\cdot(\mathbf{s}-\mathbf{s}_{hkl})}\, \mathrm{d}V_{\mathbf{L}}\, w(\mathbf{D})\, \mathrm{d}\mathbf{D}}{\int_0^\infty w(\mathbf{D})\, \mathrm{d}\mathbf{D}} \tag{2.43}$$

Swapping the order of integration yields

$$I_{V_{hkl}}(\mathbf{s}) = \frac{\int_{-\infty}^{\infty}\int_{0}^{\infty} A(\mathbf{L},\mathbf{D})\, w(\mathbf{D})\,\mathrm{d}\mathbf{D} e^{-2\pi\imath\mathbf{L}\cdot(\mathbf{s}-\mathbf{s}_{hkl})}\,\mathrm{d}V_{\mathbf{L}}}{\int_{0}^{\infty} w(\mathbf{D})\,\mathrm{d}\mathbf{D}} \tag{2.44}$$

The volume weighted CVF, independent of the vector of size parameters $\mathbf{D}$, can be defined as

$$A(\mathbf{L}) \equiv \frac{\int_{0}^{\infty} A(\mathbf{L},\mathbf{D})\, w(\mathbf{D})\,\mathrm{d}\mathbf{D}}{\int_{0}^{\infty} w(\mathbf{D})\,\mathrm{d}\mathbf{D}}. \tag{2.45}$$

With this the volume-weighted shape profile function expressed in equation 2.44 can be rewritten as

$$\begin{aligned} I_{V_{hkl}}(\mathbf{s}) &= \mathcal{F}\left[A(\mathbf{L})\, e^{-2\pi\imath\mathbf{L}\cdot\mathbf{s}_{hkl}}\right] \\ &= \int_{-\infty}^{\infty} A(\mathbf{L})\, e^{-2\pi\imath\mathbf{L}\cdot(\mathbf{s}-\mathbf{s}_{hkl})}\,\mathrm{d}V_{\mathbf{L}}. \end{aligned} \tag{2.46}$$

This approach allows for the computation of the shape profile function arising from a polydisperse system of domains independently of the integrated intensity of the profile, proportional to $|F(s,\mathbf{s}_{hkl})|^2$.

In some specific cases equation 2.45 can be written analytically. Scardi and Leoni elaborated analytic expressions for log-normal and Poisson distributions of spheres, cubes, and regular tetrahedra and octahedra [26]. For example, by assuming an ensemble of spherical domains with diameters described by a log-normal distribution with log-normal mean and standard deviation of μ and σ respectively, the CVF can be written analytically as [26]

$$\begin{aligned} A(L) = \operatorname{erfc}\frac{\ln L-\mu-3\sigma^2}{\sqrt{2}\sigma} - \frac{3}{4}\operatorname{erfc}\frac{\ln L-\mu-2\sigma^2}{\sqrt{2}\sigma} e^{-\mu-\frac{5}{2\sigma^2}} L + \\ \frac{1}{2}\operatorname{erfc}\frac{\ln L-\mu}{\sqrt{2}\sigma} e^{-3\mu-\frac{9}{2\sigma^2}} L^3 \end{aligned} \tag{2.47}$$

where erfc represents the complementary error function. The FT of this expression can then be evaluated numerically to obtain the associated shape profile function. Examples of such profiles are presented in Figures 2.15b and 2.17.

Handling of the diffraction effect of domain size distributions directly in this way can help to highlight some issues with traditional LPA techniques, which typically rely on understanding either the Bragg peak FWHM or integral breadth β (the ratio of the Bragg peak area to the intensity) as a function of scattering vector. In what is often called Williamson-Hall analysis, a straight line is fit to $\beta(s)$ data, and the $s = 0$ value of β is retrieved through extrapolation [18]. Under a certain set of assumptions, this integral breadth is inversely proportionate to the volume weighted mean column length (MCL) $\langle L \rangle_V$ of the domains in the powder, $\beta(s = 0) = 1/\langle L \rangle_V$. In the absence of other profile broadening effects, $\beta(s) = \beta(s = 0)$ ($\beta(s)$ is a line with zero slope).

By assuming a domain morphology the MCL $\langle L \rangle_V$ can be translated to an average domain dimension. As an example, by assuming an ensemble of spherical domains, $\langle L \rangle_V$ can be related to the volume weighted mean diameter as $\langle L \rangle_V = 4/3 \langle D \rangle_V$, where $\langle D \rangle_V$ represents the volume-weighted mean diameter. The volume-weighted mean diameter however in most cases does not itself uniquely establish the shape of the distribution of diameters.

This can be made more clear if a powder of spherical domains with log-normally distributed diameters is specifically considered. In this case, the shape profile functions can be computed using equation 2.47, and $\langle D \rangle_V$ is the ratio of the fourth distribution moment to the third distribution moment, leading to the expression $\langle D \rangle_V = e^{\mu + 7/2\sigma^2} = \frac{4}{3\beta(s=0)}$ [59, 60]. There are an infinite number of values of σ and μ that yield the *same* $\langle D \rangle_V$ and thus the same $\beta(s = 0)$. An example is shown in Figure 2.15, where three different log-normal distributions are considered, pictured in Figure 2.15a. Each distribution possesses a different algebraic mean diameter $\langle D \rangle$, leading to three completely distinct profile functions, shown in Figure 2.15b.

Each distribution however shows an *identical* volume weighted mean diameter, $\langle D \rangle_V = 300$ Å, and thus each profile shows an identical integral breadth, $\beta = 0.00444$ Å^{-1}. This suggests that techniques relying on integral breadth alone are unlikely to provide *unambiguous* statistical information on the domain size. This is explored in more detail in Section 3.3.1.

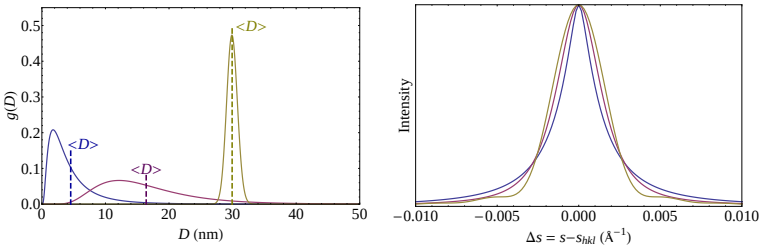

(a) Size distributions (b) Profile functions

Figure 2.15: Three different log-normal distributions are shown, each with a different mean diameter $\langle D \rangle$, but an identical volume weighted mean $\langle D \rangle_V$. Also shown are the associated line-profiles, computed using equation 2.47. Since each distribution has an identical volume weighted mean, the integral breadth of each profile is identical

2.5.5 Powder averaging

To obtain the powder-averaged diffracted intensity distribution of an ideal powder of perfect, spatially finite crystals, equation 2.34 must be integrated over powder diffraction spheres as in Section 2.4.3. Figure 2.16 gives a schematic depiction of a cross section of this powder integration sphere, considering the diffracted intensity distribution originally shown in Figure 2.12. Adopting this approach, the intensity distribution can be rewritten as

$$I(s) = \frac{1}{4\pi s^2} \iint_S I(\mathbf{s}) \, \mathrm{d}S \tag{2.48}$$

$$= \sum_{hkl} \frac{|F(s, \mathbf{s}_{hkl})|^2}{4\pi s^2} \int_0^{2\pi} \int_0^{\pi} |S(\mathbf{s} - \mathbf{s}_{hkl})|^2 \, s^2 \sin\theta \, \mathrm{d}\theta \, \mathrm{d}\phi$$

$$=$$

$$\sum_{hkl} \frac{|F(s, \mathbf{s}_{hkl})|^2}{4\pi} \int_0^{2\pi} \int_0^{\pi} \int_{-\infty}^{\infty} A(\mathbf{L}) \, e^{-2\pi i \mathbf{L} \cdot (\mathbf{s} - \mathbf{s}_{hkl})} \, \mathrm{d}V_{\mathbf{L}} \sin\theta \, \mathrm{d}\theta \, \mathrm{d}\phi. \tag{2.49}$$

The orientation average in equation 2.49 applies only to $e^{-2\pi i \mathbf{L} \cdot \mathbf{s}}$, and has the analytical solution of $\sin(2\pi Ls)/2\pi Ls = \mathrm{sinc}(2\pi Ls)$. Equation

2.49 can be rewritten as

$$I(s) = \sum_{hkl} |F(s, \mathbf{s}_{hkl})|^2 \int_{-\infty}^{\infty} A(\mathbf{L})\, e^{-2\pi\imath \mathbf{L}\cdot\mathbf{s}_{hkl}} \mathrm{sinc}(2\pi L s)\ \mathrm{d}V_{\mathbf{L}}. \quad (2.50)$$

The integral in equation 2.50 contains the even functions $A(\mathbf{L})$ and $\mathrm{sinc}(2\pi L s)$ along with the complex function $e^{-2\pi\imath \mathbf{L}\cdot\mathbf{s}_{hkl}}$. The complex function can be written as the sum of the even, real component $\cos(-2\pi\mathbf{L}\cdot\mathbf{s}_{hkl})$, and the odd, imaginary component $\imath\sin(-2\pi\mathbf{L}\cdot\mathbf{s}_{hkl})$, using Euler's relation. The integral can then be expanded into the sum of two integrals, with one integral being entirely even and real and the other being entirely odd and imaginary. The integration range is symmetric over all space, and thus the odd component of the sum is explicitly zero. With this, the integral in equation 2.50 can be rewritten as

$$I(s) = \sum_{hkl} |F(s, \mathbf{s}_{hkl})|^2 \int_{-\infty}^{\infty} A(\mathbf{L}) \cos(-2\pi\mathbf{L}\cdot\mathbf{s}_{hkl}) \mathrm{sinc}(2\pi L s)\ \mathrm{d}V_{\mathbf{L}}. \quad (2.51)$$

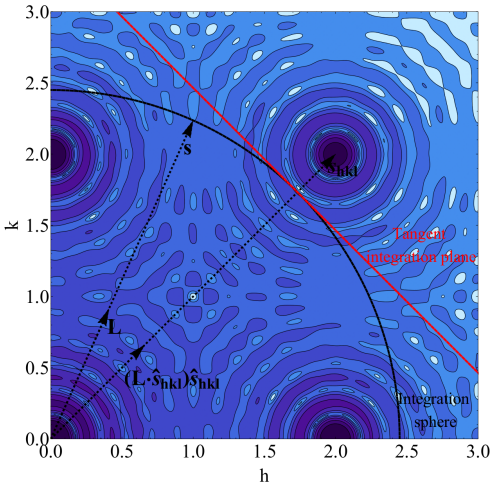

Figure 2.16: A schematic to illustrate the concept of the powder integration sphere and its approximation by tangent planes

Analytic solutions for the integral in equation 2.51 only exist for special forms of $A(\mathbf{L})$. A number of alternative, approximate solutions exist for computing the powder integral for spatially finite crystals, including integration on planes which are tangent to the powder integration sphere. This is done by using the differential surface $\mathrm{d}S = \hat{\mathbf{s}} \cdot \hat{\mathbf{s}}_{hkl}\, \mathrm{d}A/s$ rather than $\mathrm{d}S = s^2 \sin\theta\, \mathrm{d}\theta\, \mathrm{d}\phi$ in equation 2.48. Using this approach, Stokes and Wilson wrote the powder intensity as [23]

$$I(s) = \sum_{hkl} \frac{|F(s, \mathbf{s}_{hkl})|^2}{4\pi s^2} \int A\left(\left(\mathbf{L} \cdot \hat{\mathbf{s}}_{hkl}\right) \hat{\mathbf{s}}_{hkl}\right) \cos\left(2\pi \left(\mathbf{s} \cdot \hat{\mathbf{s}}_{hkl} - s_{hkl}\right) L\right) \mathrm{d}L. \tag{2.52}$$

Within this expression, the profile shape is represented by a one-dimensional cosine FT of the CVF evaluated along the vector parallel to $\hat{\mathbf{s}}_{hkl}$

Ino and Minami corrected this expression to consider very small domains, writing the powder integral as [61]

$$I(s) = \sum_{hkl} \frac{|F(s, \mathbf{s}_{hkl})|^2}{4\pi s s_{hkl}} \int A\left(\left(L \cdot \hat{\mathbf{s}}_{hkl}\right) \hat{\mathbf{s}}_{hkl}\right) \Big(\cos\left(2\pi \left(\mathbf{s} \cdot \hat{\mathbf{s}}_{hkl} - s_{hkl}\right) L\right) - \cos\left(2\pi \left(\mathbf{s} \cdot \hat{\mathbf{s}}_{hkl} + s_{hkl}\right) L\right) \Big) \mathrm{d}L. \tag{2.53}$$

Figure 2.16 helps to illustrate the meaning of these integration approximations. Shown is a schematic of a two-dimensional ($hk0$) section of RS with diffracted intensity contours, originally pictured in Figure 2.12. Superimposed are sections of powder integration surfaces used in equation 2.49 (sections of a sphere) and equation 2.52 (sections of a plane) when considering the (110) Bragg spot. Also shown are the geometric meanings of the vectors in both equations.

For smaller domains, showing more diffuse diffraction spots, approximating the powder integration sphere as tangent planes as in equation 2.52 and equation 2.53 introduces significant inaccuracies. In this case, numerical integration in reciprocal space may be preferred, as proposed by Beyerlein *et al.* [62]. Another alternative is to abandon the RS-based approaches reviewed in this chapter and rely instead on a DS approach, as reviewed in Chapter 3.

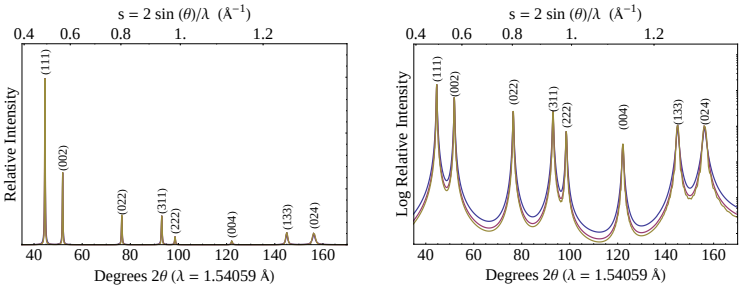

(a) Linear scale

(b) Log scale

Figure 2.17: The ensemble-averaged diffracted intensity distribution resulting from a nickel powder composed of spherical domains, with diameters described by the three distributions shown in Figure 2.15a, on both a linear scale and a log scale.

All of the powder intensity distributions proposed above (equations 2.50, 2.52, and 2.53) show some distinctive features that are often neglected in traditional pattern fitting or decomposition, discussed briefly in Section 1.2. Each shows a unique form of the Lorentz factor, that is in turn also *different* from that seen in Section 2.4.3, further reinforcing the point that the form of this powder correction depends strongly on both the form of the initial diffracted intensity distribution and the method of powder integration.

While the integral in equation 2.52 is symmetric with respect to $\mathbf{s}_{hkl}$, the same is not true for the integrals within equations 2.53 and 2.50, implying an intrinsic profile asymmetry when using these equations. Furthermore, within all three equations *both* the Lorentz factor *and* the structure factor vary across the entire profile, compounding line-profile asymmetries and shifts already present due to an asymmetric integral. Finally, the transformation from scattering vector s to the more commonly observed scattering angle 2θ is not linear, leading to further asymmetries in the profiles. These effects depend on both the nature of the diffraction experiment and the fine details of the both the atomic and microstructure, and act together to create an asymmetric and shifted line-profile. It can be possible to retrieve the degree of asymmetry and shift from an intensity distribution through empirical

profile decomposition with an unconstrained model and a carefully chosen profile function, but linking the retrieved parameters to the fine details of the atomic and nanostructure requires the arduous derivation of structure specific analytic expressions [21].

Much more useful is a direct computation of the powder-averaged diffracted intensity distribution. An example of this is presented in Figure 2.17, where equation 2.47 is used with equation 2.52 to simulate data from three different samples of nanocrystalline nickel (Section 2.1). Shown are the powder-averaged diffracted intensity distributions of three hypothetical nickel powder samples, composed of otherwise perfect spherical domains, with diameters described by the log-normal size distributions presented in Figure 2.15a. The line-profiles representing each Bragg peak are computed directly, and each line-profile shows an identical integral breadth expressed in units of scattering vector both across the scattering vector range and between the different datasets. Thus, if only integral breadth based LPA methods were used to estimate the average domain size of the samples simulated in Figure 2.17, each would appear identical.

2.6 Spatially infinite crystals with one-dimensional disorder

Analytic expression for crystal electron densities can also be found if the condition of three-dimensional periodicity, imposed in Section 2.4 and Section 2.5, is relaxed. When periodicity is removed along one direction, crystals are said to be characterized by *one-dimensional disorder* or *stacking disorder*, used interchangeably within this text. Such disorder can manifest as in a number of forms, such as mistakes in a simple polytype sequence, fluctuations in layer-layer relative positions, layer-layer mutual rotation defects, or as polytype interlayering. A common feature of all such manifestations is that crystals are composed of bi-dimensionally periodic atomic scale layers, arranged by stacking along a third direction. The diffracted intensity distribution from a large collection of such crystals is the incoherent ensemble-average of the diffracted intensity distribution from *each* arrangement, weighted by the occurrence likelihood of the arrangement.

Following routes outlined in Sections 2.4.2 or 2.5.2, it would be straight-

forward to express the diffracted intensity distribution for any *individual* layer arrangement, but explicitly considering *all possible* arrangements in the weighted ensemble-average can be prohibitively expensive, from a computational standpoint. Furthermore, it is not straightforward to compute the likelihood or weight of each individual layer arrangement within the weighted ensemble-average. Thus the problem is two-fold: the ensemble-average contains many terms and a convenient and accurate weighting scheme must be found.

A great deal of effort has been put forward in solving these two problems. In 1937, Landau first proposed explicit formulas for the diffracted intensity distribution from ensembles of crystals composed of mutually shifted coherently scattering lamellar domains of different thicknesses [63]. The treatment was extended in the same year by Lifschitz who generalized the approach to lamellar domains with different atomic content and variable spacings [64].

In 1942, Wilson presented a difference equation method, later extended by Paterson, where a correlation function, giving the probability that layers are separated by certain distances, is used to compute the diffracted intensity [65–67]. This approach forms the basis of the most common treatments of diffraction from linearly disordered close-packed crystals [21, 68]. It has been widely employed in studying twin and deformation faults within close-packed structures, and has led to the concept of "fault probabilities." Several authors later reviewed and adapted the difference equation methods [69, 70], presenting simplified explicit expressions for specific structures [71].

In 1942, Hendricks and Teller developed a much more general treatment, using a probability matrix to describe nearest neighbor layer-layer correlations, rather than considering fault probabilities. This approach also allowed for variable layer contents and layer-layer stacking vectors [25]. It was used successfully to explain diffuse intensity from layered materials such as disordered graphite [72], mica [14] and other close-packed structures. Many authors have since worked with the Hendricks-Teller description, elaborating on mathematical methods [73–81] or deriving explicit solutions for specific structure types [82, 83]. Over several papers, Jagodzinski [84–87] obtained explicit solutions within the Hendricks-Teller formalism for various ranges of interaction between layers, beyond the simple layer-layer case outlined

by Hendricks and Teller, and allowing for clustering or extended correlations between stacking sequences.

In 1991, Treacy *et al.* developed a simple and general approach for computing the averaged intensity distribution from ensembles of linearly disordered crystals [88]. It is based on the same general structure description as the Hendricks-Teller formalism, also using a probability matrix to describe nearest neighbor layer-layer correlations. Treacy *et al.* however exploited the self-similarity of stacking sequences to recursively write the ensemble-averaged scattered wave function as entries within vectors, rather than matrices, reducing the computational overhead and making the mathematics more transparent.

The approach of Treacy and colleagues is the simplest and most mathematically transparent yet mentioned. It is also just as general as the Hendricks-Teller matrix based approach, allowing for interactions between an arbitrary number of layer-nearest neighbors, with minimal restrictions on the atomic contents or mutual arrangement of the layers [25]. For these reasons it is the preferred starting point in this study. In the original work, Treacy and colleagues did not explicitly consider a lattice function and no analytic expressions for the powder intensity distribution were presented. Furthermore, points in reciprocal space which are unaffected by one-dimensional disorder were analytically broadened by an unphysical "detuning" of the intensity equation.

This section then details a novel extension of the work of Treacy and colleagues, leading to a new powder intensity equation which can be used to directly compute the diffracted intensity from a powder of infinite crystals showing extensive stacking disorder without the need for detuning. Also shown is a methodology to approximate the diffracted intensity from a powder of finite crystals showing extensive stacking disorder, without employing empirical profile functions.

2.6.1 Electron density

To begin, an electron density function of a three-dimensional layer with only two-dimensional periodicity must be considered. This is done by first modifying the lattice function as presented in equation 2.8. The sum on w, associated with the third dimension of periodicity, is removed, resulting in a double sum associated with the layer lattice

vectors **a** and **b**, following Drits and Tchoubar [14]. The lattice function is then written as

$$z\left(\mathbf{r}\right) \equiv \sum_{u=-\infty}^{\infty} \sum_{v=-\infty}^{\infty} \delta\left(\mathbf{r} - u\mathbf{a} - v\mathbf{b}\right) = \sum_{uv} \delta\left(\mathbf{r} - \mathbf{r}_{uv}\right), \tag{2.54}$$

The symmetry of this two-dimensional lattice can be described by one of the 5 two-dimensional Bravais lattices [89]. To impose coherence between all layers within the crystal, it is assumed that **a** and **b** in equation 2.54 are identical for every layer throughout the crystal. Further, they are defined such that the plane they span is perpendicular to the Cartesian direction $\hat{\mathbf{z}}$, that is, $\left(\mathbf{a} \times \mathbf{b}\right) / \left\|\mathbf{a} \times \mathbf{b}\right\| = \hat{\mathbf{z}}$.

This lattice function can be dressed with unit cell electron density by a convolution, as in Section 2.4. The electron density of the atomic scale layer is then written

$$\rho_{layer}\left(\mathbf{r}\right) = \left(\sum_{p_{layer}=1}^{n_{layer}} U_{p_{layer}}\left(\left\|\mathbf{r} - \mathbf{r}_{\mathbf{p_{layer}}}\right\|\right) \right) * z\left(\mathbf{r}\right). \tag{2.55}$$

In the case of the three-dimensionally periodic crystals outlined in Sections 2.4 and 2.5, the position vector of the p^{th} atom in the unit cell was defined in terms of fractions of the three lattice vectors, $\mathbf{r}_p = x_p\mathbf{a} + y_p\mathbf{b} + z_p\mathbf{c}$. However, for crystals described in this section, there is no assumption of periodicity along a third dimension, and thus there is no third lattice vector. As a result in equation 2.55 the position vector of the p^{th} atom in the layer unit cell must be redefined as $\mathbf{r}_{p_{layer}} \equiv x_{p_{layer}}\mathbf{a} + y_{p_{layer}}\mathbf{b} + z_{p_{layer}}c_{layer}\hat{\mathbf{z}}$, where c_{layer} is the *spatial extent*, or thickness, of the layer unit cell along $\hat{\mathbf{z}}$, and $z_{p_{layer}}$ is the fractional atomic coordinate of atom p within the layer unit cell, with respect to this layer thickness. The symmetry within the two-dimensionally periodic layer unit cell as written in equation 2.55 can be described by one of the 80 sub-periodic *layer groups* [43].

Thus equation 2.55 represents a bi-periodic, three-dimensional layer of electron density. To build a three-dimensional crystal these layers are stacked along the direction perpendicular to their periodicity. Summing translated layer electron densities yields the partially disordered

crystal, which can be written as

$$\rho\left(\mathbf{r}\right)=\rho_{layer1}\left(\mathbf{r}\right)+\rho_{layer2}\left(\mathbf{r}-\mathbf{R}_{12}\right)+\rho_{layer3}\left(\mathbf{r}-\mathbf{R}_{12}-\mathbf{R}_{23}\right)+\cdots, \tag{2.56}$$

where $\mathbf{R}_{12}$ and $\mathbf{R}_{23}$ represent translation vectors, spanning the origins between adjacent layers. By proceeding as in Section 2.4 and taking the squared magnitude of the FT of equation 2.56, it would be possible to arrive at an analytic expression for the diffracted intensity of this specific configuration. As mentioned at the beginning of this section, a huge number of configurations would need to be explicitly considered to accurately represent the diffracted intensity distribution of a polycrystalline ensemble.

Many authors have shown that adopting a minimal set of objects and set of assembly instructions can reduce the computational overhead (see for example the introduction to this section). To achieve this here, it is assumed that the stacking of layers can be modeled by a discrete-time Markov chain, a practice which has a long history within the literature [14, 88, 90–92]. That is, each layer in the crystal stack is one of a finite number of layer types represented by one of M total states of a Markov process. Each layer type i is characterized by a common crystal lattice $z\left(\mathbf{r}\right)$ shared between all layer types, but is permitted to have a unique unit cell $\sum_{p_i=1}^{n_i}U_{p_i}\left(\left|\mathbf{r}-\mathbf{r}_{p_i}\right|\right)$ and layer thickness c_i. In this way the electron density of the layer of general type i can be written as

$$\rho_i\left(\mathbf{r}\right)=\left(\sum_{p_i=1}^{n_i}U_{p_i}\left(\left\|\mathbf{r}-\mathbf{r}_{\mathbf{p_i}}\right\|\right)\right)*z\left(\mathbf{r}\right)=\sum_{uv}\sum_{p_i=1}^{n_i}U_{p_i}\left(\left\|\mathbf{r}-\mathbf{r}_{\mathbf{p_i}}-\mathbf{r}_{\mathbf{uv}}\right\|\right), \tag{2.57}$$

Each layer type i is further associated with transition vectors $\mathbf{R}_{ij}$ defining each transition from state i to state j. These transition vectors serve to relate adjacent layers spatially, spanning the two origins of the layers. They are defined here in terms of fractions of the common lattice vectors and unique layer thicknesses $\mathbf{R}_{ij}\equiv x_{ij}\mathbf{a}+y_{ij}\mathbf{b}+z_{ij}c_i\hat{\mathbf{z}}$. Thus when describing a general N-layer crystal, built as a stack of the arbitrary layer types $ijk\ldots$, the crystal electron density can be written as

$$\rho_{ijk\ldots}^{(N)}\left(\mathbf{r}\right)=\rho_i\left(\mathbf{r}\right)+\rho_j\left(\mathbf{r}-\mathbf{R}_{ij}\right)+\rho_k\left(\mathbf{r}-\mathbf{R}_{ij}-\mathbf{R}_{jk}\right)+\cdots. \tag{2.58}$$

For "traditional" Markov processes, called first-order Markov processes, the transition probabilities depend only on the identity of the current state. Here these transition probabilities are defined as $\alpha_{ij} \equiv \Pr\left(X_{n+1} = \rho_j\left(\mathbf{r} + \mathbf{R}_{ij}\right) | X_n = \rho_i\left(\mathbf{r}\right)\right)$, or in plain terms the probability that a layer of type i will be spatially adjacent to a layer of type j with mutual translation $\mathbf{R}_{ij}$. Higher order Markov processes can be considered in this formalism and are discussed more in Section 3.1.1.

The transition probabilities populate the right stochastic probability matrix for the Markov process, $\mathbf{P} \equiv [\alpha_{ij}]$. If the Markov process described by $\mathbf{P}$ is irreducible and aperiodic, then there exists a stationary distribution vector $\boldsymbol{\pi}$. This stationary distribution vector is the 1-normalized left eigenvector of $\mathbf{P}$ associated with the left eigenvalue of 1, and correspondingly satisfies the characteristic equation $\boldsymbol{\pi}\mathbf{P} = \boldsymbol{\pi} = [p_i]$, where p_i is the intrinsic probability of Markov state or layer type i. A Markov process that is not irreducible and aperiodic is usually an indication that the stacking sequences being described are in fact periodic in some fashion. While the approached outlined here can accommodate such a situation by assuming a uniform initial distribution ($[p_i] = 1/M$), it may be more appropriate to revert to the models outlined in Sections 2.4 or 2.5.

Under this Markov framework, the probability of any crystal in the ensemble showing a first layer of type i is p_i. The probability that this layer of type i is followed by a layer of type j is α_{ij}, while the probability of the specific layer sequence $ij\ldots$ is the product $p_i\alpha_{ij}\ldots$. A crystal described by the general layer sequences $ijk\ldots$, as outlined in equation 2.58, then occurs with a probability $p_i\alpha_{ij}\alpha_{jk}\ldots$. This conveniently provides a compact framework for computing the probability weights in the ensemble averaged, addressing one problem mentioned in the introduction.

There exist exactly M^N possible ways of permuting M layer types to build crystals with exactly N total layers. While some of these configurations may be equivalent according to the combined symmetry of the stacking operations and the layers, the most general case, where each permutations is unique, will be considered here.

2.6.2 Scattering

As in all previous sections on scattering, the scattered wave amplitude is the FT of the electron density of the crystal. To begin, only the general crystal built by the $ijk\ldots$ layer sequence presented in equation 2.58 is considered, after this a weighted sum will be expanded. Using this general crystal, the scattered wave amplitude can be written as

$$\begin{aligned}\varphi^{(N)}_{ijk\ldots}(\mathbf{s}) &= \mathcal{F}\left[\rho^{(N)}_{ijk\ldots}(\mathbf{r})\right] \\ &= \mathcal{F}\left[\rho_i(\mathbf{r})\right] + \mathcal{F}\left[\rho_j(\mathbf{r}-\mathbf{R}_{ij})\right] + \mathcal{F}\left[\rho_k(\mathbf{r}-\mathbf{R}_{ij}-\mathbf{R}_{jk})\right] + \cdots \\ &= \mathcal{F}\left[\rho_i(\mathbf{r})\right] + e^{-2\pi\imath\mathbf{R}_{ij}\cdot\mathbf{s}}\mathcal{F}\left[\rho_j(\mathbf{r})\right] + e^{-2\pi\imath(\mathbf{R}_{ij}+\mathbf{R}_{jk})\cdot\mathbf{s}}\mathcal{F}\left[\rho_k(\mathbf{r})\right] + \cdots.\end{aligned} \tag{2.59}$$

In equation 2.59, $\mathcal{F}\left[\rho_i(\mathbf{r})\right]$ represents the scattered wave from only layer type i, and can be expanded as

$$\begin{aligned}\mathcal{F}\left[\rho_i(\mathbf{r})\right] &= \mathcal{F}\left[\sum_{uv}\sum_{p_i=1}^{n_i} U_{p_i}\left(\|\mathbf{r}-\mathbf{r}_{\mathbf{p_i}}-\mathbf{r}_{\mathbf{uv}}\|\right)\right] \\ &= \sum_{uv}\sum_{p_i=1}^{n_i}\mathcal{F}\left[U_{p_i}(r)\right]e^{-2\pi\imath\mathbf{r}_{p_i}\cdot\mathbf{s}}e^{-2\pi\imath\mathbf{r}_{uv}\cdot\mathbf{s}} \\ &= \sum_{uv}\sum_{p_i=1}^{n_i} f_{p_i}(s)\,e^{-2\pi\imath\mathbf{r}_{p_i}\cdot\mathbf{s}}e^{-2\pi\imath\mathbf{r}_{uv}\cdot\mathbf{s}} \\ &= \sum_{uv} F_i(\mathbf{s})\,e^{-2\pi\imath\mathbf{r}_{uv}\cdot\mathbf{s}}.\end{aligned} \tag{2.60}$$

The lack of three-dimensional periodicity requires that the structure factor of the i-type layer unit cell, $F_i(\mathbf{s})$, in equation 2.60 takes on a different definition than that adopted previously. Within Section 2.4.2, the dot product $\mathbf{r}_p\cdot\mathbf{s}$ in the phase terms $e^{-2\pi\imath\mathbf{r}_p\cdot\mathbf{s}}$ of the unit cell structure factor could be simplified as $x_ph+y_pk+z_pl$ by exploiting the orthogonality conditions of the DS and RS lattices, implied in equation 2.18. However, the one-dimensional disorder assumed in this section entails that no third DS or RS lattice vector is present. As a result, the dot product within the phase terms of the structure factor of a *layer unit cell*, $\mathbf{r}_{p_i}\cdot\mathbf{s}$ simplifies to $x_{p_i}h+y_{p_i}k+z_{p_i}c_il$, where l in this case

is the projection of $\mathbf{s}$ onto the unit vector $\hat{\mathbf{Z}} = \frac{\mathbf{a}^* \times \mathbf{b}^*}{|\mathbf{a}^* \times \mathbf{b}^*|}$, In this section, l represents a continuous Miller index and is *a real number, with units identical to* s.

With these clarifications, the FT of layer type i in equation 2.60 can be substituted into equation 2.59, and the scattered wave amplitude can be written as

$$\varphi^{(N)}_{ijk\ldots}(\mathbf{s}) = \sum_{uv} e^{-2\pi\imath \mathbf{r}_{uv}\cdot\mathbf{s}} \left(F_i(\mathbf{s}) + e^{-2\pi\imath \mathbf{R}_{ij}\cdot\mathbf{s}} F_j(\mathbf{s}) + e^{-2\pi\imath(\mathbf{R}_{ij}+\mathbf{R}_{jk})\cdot\mathbf{s}} F_k(\mathbf{s}) + \cdots \right) \tag{2.61}$$

As mentioned earlier, of real interest is the ensemble-average of *all* M^N sequences with exactly N total layers. This average intensity can be represented as a probability weighted incoherent sum of the scattered intensity of all possible layer configurations. Each individual intensity distributions is represented as the squared magnitude of the complex wave scattered from each configuration. Adopting this approach, the averaged diffracted intensity distribution can be written compactly as

$$I(\mathbf{s}) = \sum_{i,j,k\ldots=1}^{M} p_i \alpha_{ij} \alpha_{jk} \ldots \left(\varphi^{(N)}_{ijk\ldots}(\mathbf{s}) \right) \left(\varphi^{(N)}_{ijk\ldots}(\mathbf{s}) \right)^*, \tag{2.62}$$

where the preceding factor of $p_i \alpha_{ij} \alpha_{jk} \ldots$ represents the probability weighting of each term in the average.

The brevity of equation 2.62 can be somewhat misleading. The summation in equation 2.62 represents an N-tuple sum, with each running over all layer types, leading to M^N total terms in the average. The terms within the average are however a product of sums, each containing N^2 total terms. Substituting the scattered wave amplitude in

equation 2.6.2 directly, the intensity distribution can be written as

$$I(\mathbf{s}) = \sum_{i,j,k\ldots=1}^{M} p_i \alpha_{ij} \alpha_{jk} \ldots \left(\sum_{uv} e^{-2\pi\imath \mathbf{r}_{uv}\cdot\mathbf{s}} \left(F_i(\mathbf{s}) + e^{-2\pi\imath \mathbf{R}_{ij}\cdot\mathbf{s}} F_j(\mathbf{s}) \right.\right.$$
$$\left. + e^{-2\pi\imath(\mathbf{R}_{ij}+\mathbf{R}_{jk})\cdot\mathbf{s}} F_k(\mathbf{s}) + \cdots \right) \left) \left(\sum_{u'v'} e^{2\pi\imath \mathbf{r}_{u'v'}\cdot\mathbf{s}} \left(F_i(\mathbf{s}) + e^{-2\pi\imath \mathbf{R}_{ij}\cdot\mathbf{s}} F_j(\mathbf{s}) \right.\right.\right.$$
$$\left. \left. + e^{-2\pi\imath(\mathbf{R}_{ij}+\mathbf{R}_{jk})\cdot\mathbf{s}} F_k(\mathbf{s}) + \cdots \right)^* \right)$$
$$I(\mathbf{s}) = \sum_{i,j,k\ldots=1}^{M} p_i \alpha_{ij} \alpha_{jk} \ldots \left(\sum_{u'v'} \sum_{uv} e^{-2\pi\imath(\mathbf{r}_{uv}-\mathbf{r}_{u'v'})\cdot\mathbf{s}} \left| F_i(\mathbf{s}) + e^{-2\pi\imath \mathbf{R}_{ij}\cdot\mathbf{s}} F_j(\mathbf{s}) \right.\right.$$
$$\left. \left. + e^{-2\pi\imath(\mathbf{R}_{ij}+\mathbf{R}_{jk})\cdot\mathbf{s}} F_k(\mathbf{s}) + \cdots \right|^2 \right), \tag{2.63}$$

However, the double lattice sum of phase terms can be rewritten as a single RS lattice sum of Dirac distributions (a RS lattice function), by arguments similar to those adopted in Section 2.4.2 for equation 2.16. This new RS lattice is however not identical to that employed in Sections 2.4.2 and 2.5.2. The RS lattice employed here is written as

$$Z(\mathbf{s}) \equiv \sum_{h=-\infty}^{\infty} \sum_{k=-\infty}^{\infty} \delta(\mathbf{s}_0 - h\mathbf{a}^* - k\mathbf{b}^*) = \sum_{hk} \delta(\mathbf{s}_0 - \mathbf{s}_{hk}), \tag{2.64}$$

where $\mathbf{s}_0$ is the projection of $\mathbf{s}$ onto the plane spanned by $\mathbf{a}^*$ and $\mathbf{b}^*$,

$$\mathbf{s}_0 \equiv \mathbf{s} - \mathbf{s} \cdot \frac{\mathbf{a}^* \times \mathbf{b}^*}{|\mathbf{a}^* \times \mathbf{b}^*|}. \tag{2.65}$$

Within this definition, $\frac{\mathbf{a}^* \times \mathbf{b}^*}{|\mathbf{a}^* \times \mathbf{b}^*|}$ is equivalent to the third Cartesian unit vector in RS, $\hat{\mathbf{Z}}$, and $\mathbf{s} \cdot \frac{\mathbf{a}^* \times \mathbf{b}^*}{|\mathbf{a}^* \times \mathbf{b}^*|}$ can be rewritten simply as $l\hat{\mathbf{Z}}$, where l is again the new continuous Miller index. With this, the reciprocal lattice of a finite layer can be rewritten as

$$Z(\mathbf{s}) = \sum_{hk} \delta\left(\mathbf{s} - \mathbf{s}_{hk} - l\hat{\mathbf{Z}}\right) = \sum_{hk} \delta(\mathbf{s} - \mathbf{s}_{hkl}). \tag{2.66}$$

Thus, the RS lattice of the layer is a sum of Dirac delta distributions, periodic in two-dimensions, and extended along the third dimension such that $Z\left(\mathbf{s} = h\mathbf{a}^* + k\mathbf{b}^* + t\hat{\mathbf{Z}}\right) = \delta(0)$ for all t when h and k are both integers. A RS lattice of this type, along with the associated DS lattice, is depicted schematically in Figure 2.18 as a two-dimensionally periodic lattice of "Dirac rods."

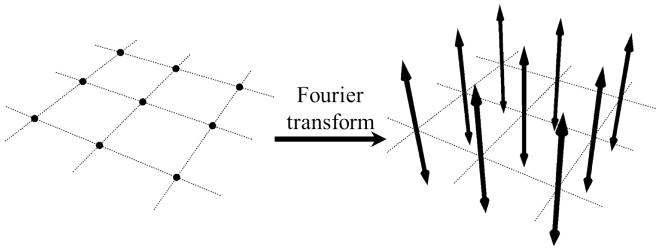

Figure 2.18: At left, a schematic representation of a DS lattice of two-dimensionally periodic, three-dimensional layer is shown. The FT of this object represents a RS lattice of Dirac rods, shown schematically at right. Here these rods are given an artificial spatial extent (width), in reality the rods haven no width and evaluate to $\delta(0)$ when $\mathbf{s} = h\mathbf{a}^* + k\mathbf{b}^* + t\hat{\mathbf{Z}}$ for all t when h and k are both integers

Substituting this RS lattice into equation 2.63 gives a new expression for the diffracted intensity distribution

$$I(\mathbf{s}) = \sum_{hk} \delta(\mathbf{s} - \mathbf{s}_{hkl}) \sum_{i,j,k\ldots=1}^{M} p_i \alpha_{ij} \alpha_{jk} \ldots \left| F_i(\mathbf{s}) + e^{-2\pi\imath \mathbf{R}_{ij}\cdot\mathbf{s}} F_j(\mathbf{s}) + e^{-2\pi\imath(\mathbf{R}_{ij}+\mathbf{R}_{jk})\cdot\mathbf{s}} F_k(\mathbf{s}) + \cdots \right|^2 \tag{2.67}$$

$$\begin{aligned} &= \sum_{hk} \delta(\mathbf{s} - \mathbf{s}_{hkl}) \sum_{i,j,k\ldots=1}^{M} p_i \alpha_{ij} \alpha_{jk} \ldots \Big(|F_i(\mathbf{s})|^2 \\ &+ F_i(\mathbf{s}) F_j(\mathbf{s})^* e^{2\pi\imath \mathbf{R}_{ij}\cdot\mathbf{s}} + F_i(\mathbf{s})^* F_j(\mathbf{s}) e^{-2\pi\imath \mathbf{R}_{ij}\cdot\mathbf{s}} + |F_j(\mathbf{s})|^2 \\ &+ F_j(\mathbf{s}) F_k(\mathbf{s})^* e^{2\pi\imath \mathbf{R}_{jk}\cdot\mathbf{s}} + F_j(\mathbf{s})^* F_k(\mathbf{s}) e^{-2\pi\imath \mathbf{R}_{jk}\cdot\mathbf{s}} + |F_k(\mathbf{s})|^2 \\ &+ F_k(\mathbf{s}) F_i(\mathbf{s})^* e^{-2\pi\imath(\mathbf{R}_{ij}+\mathbf{R}_{jk})\cdot\mathbf{s}} + F_k(\mathbf{s})^* F_i(\mathbf{s}) e^{2\pi\imath(\mathbf{R}_{ij}+\mathbf{R}_{jk})\cdot\mathbf{s}} + \cdots \Big) \end{aligned} \tag{2.68}$$

It is not practical to explicitly evaluate equation 2.68, but it can be rewritten by recognizing the recursive relationship of nested layer sequences, following the work of Treacy *et al.* [88]. The ensemble-averaged scattered wave amplitude from all N-layer crystals starting with a layer of type i can be written as a nested sum

$$\varphi_i^{(N)}(\mathbf{s}) = F_i(\mathbf{s}) + \sum_{j=1}^{M} \alpha_{ij} e^{-2\pi\imath \mathbf{R}_{ij}\cdot\mathbf{s}} \Bigg(F_j(\mathbf{s}) + \sum_{k=1}^{M} \alpha_{jk} e^{-2\pi\imath \mathbf{R}_{jk}\cdot\mathbf{s}} \left(F_k(\mathbf{s}) + \cdots \right) \Bigg). \quad (2.69)$$

The nested terms in equation 2.69 can be recognized as the averaged scattered wave amplitude from all $(N-1)$-layer crystals that start with a layer of type j, and equation 2.69 can be rewritten as

$$\varphi_i^{(N)}(\mathbf{s}) = \left(F_i(\mathbf{s}) + \sum_{j=1}^{M} \alpha_{ij} e^{-2\pi\imath \mathbf{R}_{ij}\cdot\mathbf{s}} \varphi_j^{(N-1)}(\mathbf{s}) \right), \quad (2.70)$$

giving a recursive relationship between $\varphi_i^{(N)}(\mathbf{s})$ and $\varphi_j^{(N-1)}(\mathbf{s})$ provided that $\varphi_i^{(0)}(\mathbf{s}) = 0$. Using equation 2.70 allows equation 2.68 to be rewritten as

$$\begin{aligned} I(\mathbf{s}) = \sum_{hk} \delta(\mathbf{s} - \mathbf{s}_{hkl}) \Bigg(& \sum_{i=1}^{M} p_i \left(F_i(\mathbf{s})^* \varphi_i^{(N)}(\mathbf{s}) + F_i(\mathbf{s}) \varphi_i^{(N)}(\mathbf{s})^* - |F_i(\mathbf{s})|^2 \right) \\ & + \sum_{i,j=1}^{M} p_i \alpha_{ij} \left(F_j(\mathbf{s})^* \varphi_j^{(N-1)}(\mathbf{s}) + F_j(\mathbf{s}) \varphi_j^{(N-1)}(\mathbf{s})^* - |F_j(\mathbf{s})|^2 \right) \\ & + \sum_{i,j,k=1}^{M} p_i \alpha_{ij} \alpha_{jk} \left(F_k(\mathbf{s})^* \varphi_k^{(N-2)}(\mathbf{s}) + F_k(\mathbf{s}) \varphi_k^{(N-2)}(\mathbf{s})^* - |F_k(\mathbf{s})|^2 \right) + \cdots \Bigg). \end{aligned} \quad (2.71)$$

The properties of the Markov process can here be exploited. The transition probabilities associated with each Markov state i must sum to

unity, specifically, $\sum_{j=1}^{M} \alpha_{ij} = 1$. This relationship allows for a collection of terms in equation 2.71, and it can be rewritten as

$$I(\mathbf{s}) = \sum_{hk} \delta(\mathbf{s} - \mathbf{s}_{hkl}) \left(\sum_{i=1}^{M} p_i \left(F_i(\mathbf{s})^* \varphi_i^{(N)}(\mathbf{s}) + F_i(\mathbf{s}) \varphi_i^{(N)}(\mathbf{s})^* - |F_i(\mathbf{s})|^2 \right) + \sum_{i=1}^{M} p_i \left(F_i(\mathbf{s})^* \varphi_i^{(N-1)}(\mathbf{s}) + F_i(\mathbf{s}) \varphi_i^{(N-1)}(\mathbf{s})^* - |F_i(\mathbf{s})|^2 \right) + \sum_{i=1}^{M} p_i \left(F_i(\mathbf{s})^* \varphi_i^{(N-2)}(\mathbf{s}) + F_i(\mathbf{s}) \varphi_i^{(N-2)}(\mathbf{s})^* - |F_i(\mathbf{s})|^2 \right) + \cdots \right). \tag{2.72}$$

Within this equation, there are N individual sums on i, with each successive sum including averaged scattered wave amplitude terms considering crystals with one less layer, from N layers ($\varphi_i^{(N)}(\mathbf{s})$) down to 0 layers ($\varphi_i^{(0)}(\mathbf{s})$). This allows for a further collection of terms, and equation 2.72 can be rewritten as

$$I(\mathbf{s}) = \sum_{hk} \delta(\mathbf{s} - \mathbf{s}_{hkl}) \sum_{m=0}^{N-1} \sum_{i=1}^{M} p_i \left(F_i(\mathbf{s})^* \varphi(\mathbf{s})_i^{(N-m)}(\mathbf{s}) + F_i(\mathbf{s}) \varphi(\mathbf{s})_i^{(N-m)}(\mathbf{s})^* - |F_i(\mathbf{s})|^2 \right). \tag{2.73}$$

The summations can be further simplified if some quantities are rewritten as vectors and matrices, again following the work of Treacy *et al.* [88]. The vector $\mathbf{F}$ of dimension M is defined as $[F_i(\mathbf{s})]$. Weighting each entry of $\mathbf{F}$ by the intrinsic probability of the associated layer type p_i gives the probability weighted structure factor vector, $\mathbf{G} \equiv [p_i F_i(\mathbf{s})]$. The $M \times M$ matrix $\mathbf{T}$ is defined as the transition probability matrix $\mathbf{P}$ weighted by the phase differences introduced by the transitions, $[\alpha_{ij} e^{-2\pi\imath \mathbf{R}_{ij} \cdot \mathbf{s}}]$. With these matrix definitions, the recursive relationship expressed in equation 2.70 can be specified in a vector format as

$$\boldsymbol{\varphi}^{(N)} = \sum_{n=0}^{N-1} \mathbf{T}^n \mathbf{F}, \tag{2.74}$$

where the vector $\boldsymbol{\varphi}^{(N)}$ of dimension M is defined as $[\varphi_i^{(N)}(\mathbf{s})]$.
Using these new vector definitions, equation 2.73 can be rewritten as

$$I(\mathbf{s}) = \sum_{hk} \delta(\mathbf{s} - \mathbf{s}_{hkl}) \left(\mathbf{G}^{*T} \sum_{m=0}^{N-1} \sum_{n=0}^{N-m-1} (\mathbf{T}^n \mathbf{F}) + \mathbf{G}^T \sum_{m=0}^{N-1} \sum_{n=0}^{N-m-1} (\mathbf{T}^n \mathbf{F})^* - \sum_{m=0}^{N-1} \mathbf{G}^{*T} \mathbf{F} \right), \quad (2.75)$$

where the superscript ^{T} indicates a transpose operation.
Of interest here however are spatially infinite crystals, and thus it is necessary to evaluate $\lim_{N\to\infty} I(\mathbf{s})$. In this situation, the sum $\sum_{m=0}^{N-1} \sum_{n=0}^{N-m-1} \frac{1}{N} \mathbf{T}^n$ is a geometric series that converges to $(\mathbf{I} - \mathbf{T})^{-1}$, where $\mathbf{I}$ is the identity matrix, if and only if the spectral radius (the largest eigenvalue λ_i in absolute value) of $\mathbf{T}$ is less than 1, that is $|\lambda_i| < 1$. To substitute $\lim_{N\to\infty} \sum_{m=0}^{N-1} \sum_{n=0}^{N-m-1} \frac{1}{N} \mathbf{T}^n$ into equation 2.75, it is necessary to consider the intensity *per layer*. With this the diffracted intensity in equation 2.75 can be rewritten as

$$I(\mathbf{s}) = \sum_{hk} \delta(\mathbf{s} - \mathbf{s}_{hkl}) \left(\mathbf{G}^{*T} (\mathbf{I} - \mathbf{T})^{-1} \mathbf{F} + \mathbf{G}^T \left((\mathbf{I} - \mathbf{T})^{-1} \mathbf{F} \right)^* - \mathbf{G}^{*T} \mathbf{F} \right). \quad (2.76)$$

Each entry i in the vector $(\mathbf{I} - \mathbf{T})^{-1}\mathbf{F}$ in equation 2.76 physically represents the average wave interference introduced in transitioning from layer i to all other layers. Here this vector is labeled $\boldsymbol{\varphi}^{(\infty)}$. Thus the intensity equation can be rewritten as

$$I(\mathbf{s}) = \sum_{hk} \delta(\mathbf{s} - \mathbf{s}_{hkl}) \left(\mathbf{G}^{*T} \boldsymbol{\varphi}^{(\infty)} + \mathbf{G}^T \boldsymbol{\varphi}^{(\infty)*} - \mathbf{G}^{*T} \mathbf{F} \right). \quad (2.77)$$

The second factor in equation 2.77 is here denoted $\boldsymbol{\Psi}(\mathbf{s})$ for brevity. This is a similar result as that obtained in the case of perfect spatially infinite crystals explored in Section 2.4.2, where the diffracted intensity was found to be a three-dimensionally periodic lattice of *hkl* Bragg points, where each is represented by a structure factor weighted Dirac

distribution. In this case, equation 2.77 represents a *two-dimensionally* periodic RS lattice of hk Bragg rods, where each is represented by a Dirac rod weighted along the third RS direction by the continuous intensity distribution $\mathbf{\Psi}(\mathbf{s})$.

Similar to the case of the perfect crystals, the intensity equation can be written as a sum on these Dirac rods

$$I(\mathbf{s}) = \sum_{hk} I_{hk}(\mathbf{s}) \tag{2.78}$$

where

$$I_{hk}(\mathbf{s}) = \delta(\mathbf{s} - \mathbf{s}_{hkl})\, \mathbf{\Psi}(\mathbf{s}).$$

Interpreting this equation, it can be seen that there are two possible cases: either the scattering vector $\mathbf{s}$ is coincident with a Bragg rod, or not. With this it is possible to write equation 2.78 piecewise as

$$I(\mathbf{s}) = \begin{cases} \delta(0)\, \mathbf{\Psi}(\mathbf{s}_{hkl}), & \text{if } \mathbf{s} = h\mathbf{a}^* + k\mathbf{b}^* + l\hat{\mathbf{Z}} = \mathbf{s}_{hkl} \\ 0, & \text{if } \mathbf{s} \neq \mathbf{s}_{hkl} \end{cases}. \tag{2.79}$$

It is interesting to look at the behavior of $\mathbf{\Psi}(\mathbf{s}_{hkl})$, which weights each (hk) Dirac rod along its length. Again, the practical example of nickel, outlined in Section 2.1, is considered. A simple Markov chain model is adopted for the one-dimensional disorder, where only the probability of a forward transition α_f between two layers is given. Adopting this approach, $\mathbf{\Psi}(\mathbf{s}_{hkl})$ can be computed as a function of the continuous Miller index l, for fixed values of h and k. It should noted that representing the nickel structure as an assembly of an hexagonal mesh of nickel atoms, as in Section 2.1, rather than the traditional cubic unit cell, entails a remapping of the Miller indices such that [21]

$$h_l = -h_c/2 + k_c/2 \tag{2.80}$$
$$k_l = -k_c/2 + l_c/2 \tag{2.81}$$
$$l_l = h_c/3 + k_c/3 + l_c/3, \tag{2.82}$$

where, h_l, k_l, and l_l are Miller indices associated with the layer description of nickel, while h_c, k_c, and l_c are Miller indices associated with the traditional fcc description of nickel.

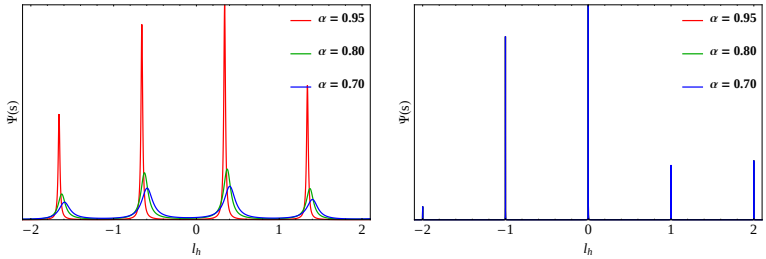

(a) $[12l]_l$ (b) $[00l]_l$

Figure 2.19: Diffracted intensity for two Bragg rods with different (listed) probabilities of a forward transition

Figure 2.19 shows $\mathbf{\Psi}(\mathbf{s}_{hkl})$ computed as a function of l for two (hk) rods, considering three different values for α_f. Figure 2.19a shows the $(12)_l$ rod, where it can be see that decreasing α_f leads to both a broadening and a shift of what would be considered "Bragg spots" in an ideal structure. The same effect is however not seen in the case of the $(00)_l$ Bragg rod, shown in Figure 2.19b. This rod shows sharp, periodic, spikes in intensity, and the shape of this intensity distribution does not appear to depend on α_f.

There is both a physical and mathematical explanation for this behavior. Mathematically, the sharp features in Figure 2.19b correspond to scattering vectors that cause the geometric series in equation 2.75 to diverge. Treacy *et al.* pointed out that this occurs at $\mathbf{s}$ values where all origin invariant quantities $\mathbf{R}_{ii}\cdot\mathbf{s}$, $(\mathbf{R}_{ij}+\mathbf{R}_{ji})\cdot\mathbf{s}$, $(\mathbf{R}_{ij}+\mathbf{R}_{jk}+\mathbf{R}_{ki})\cdot\mathbf{s}\ldots$ are integers. They also pointed out that when this condition is satisfied, the determinant of $\mathbf{I}-\mathbf{T}$ is zero [88].

The necessary and sufficient condition for convergence of the geometric series is that the spectral radius (the largest eigenvalue λ_i in absolute value) of the phase-factor weighted transition probability matrix $\mathbf{T}$ is less than 1, $|\lambda_i| < 1$. While it is also *necessary* that the determinant of $\mathbf{I}-\mathbf{T}$ does not equal zero, as suggested by Treacy *et al.* [88], this condition is generally not *sufficient* to guarantee convergence of the series.

The RS points $\mathbf{s}$ where the geometric series diverges correspond to sharp Bragg-like spots with infinite intensity, identical in form to the

Dirac delta distributions in equations 2.20 and 2.22. Practically speaking, the presence of Dirac delta distributions in equation 2.78 is no more of a problem than those in equation 2.20, as these delta distributions have a finite integrated intensity [88]. This point will be addressed further in the next section. Within Figure 2.19b, Bragg peaks associated with a divergent geometric series in equation 2.75 have been given an artificial observable width by introducing a detuning parameter of 0.001, following Treacy *et al.* [88]

Physically, the divergence of the geometric series indicates that the correlations between the (hkl) atomic planes in DS, corresponding to the RS direction $\mathbf{s}$, remain periodic, or are generally unaffected by the stacking disorder. The sharp spots on the $(00)_l$ rod in Figure 2.19b correspond to the $(111)_c$ set of lattice planes in the nickel structure, and indicate that the periodicity between the atomic planes along the $[111]_c/[001]_l$ direction is not affected by the disorder. This is reasonable conclusion, as both a forward and backward transition in this Markov chain description of the stacking disorder entail an identical translation along the $[111]_c/[001]_l$ direction.

2.6.3 Powder averaging

Equation 2.78 gives the diffracted intensity in three-dimensional RS for an infinite average crystal showing stacking disorder. Again, it may be more interesting to consider a powder; it is then necessary to take a weighted orientation average over all $\mathbf{s}$ at constant s. The powder intensity is

$$\begin{aligned} I(s) &= \frac{1}{4\pi s^2} \iint_S I(\mathbf{s}) \, \mathrm{d}S \\ &= \frac{1}{4\pi s^2} \sum_{hk} \int_0^{2\pi} \int_0^{\pi} \delta(\mathbf{s} - \mathbf{s}_{hkl}) \, \mathbf{\Psi}(\mathbf{s}) \, s^2 \sin\theta \, \mathrm{d}\theta \, \mathrm{d}\phi \end{aligned} \tag{2.83}$$

By rewriting the delta distribution in cylindrical coordinates the integral is analytic and the powder intensity is

$$I(s) = \sum_{hk} \frac{\mathbf{\Psi}(\mathbf{s}_{hkl})}{4\pi l s}. \tag{2.84}$$

where the $1/4\pi ls$ represents the Lorentz factor appropriate in this case, and is a result of the powder averaging of rods.

The intensity distribution in equation 2.84 contains "hidden" delta distributions, associated with the both the Lorentz factor and the divergence of the geometric series in equation 2.75. In the case of the former, as $l \to 0$, then $I(\mathbf{s}) \to \delta(0) \frac{\boldsymbol{\Psi}(\mathbf{s}_{hkl})}{4\pi s_{hkl}^2}$, while in the case of the latter if $|\lambda_i| \geq 1$, then $I(\mathbf{s}) \to \delta(0) \frac{\mathbf{G}^{*T}\mathbf{TF}}{4\pi s_{hkl}^2}$, where λ_i is the largest eigenvalue of the phase-weighted transition probability matrix $\mathbf{T}$. These points are however manageable, as they show a *finite* integrated intensity, just as those in equation 2.22 in Section 2.4.3.

With this, the intensity distribution in equation 2.84 can be written in a piecewise fashion as

$$I(s) = \frac{1}{4\pi s_{hkl}} \begin{cases} \frac{\boldsymbol{\Psi}(\mathbf{s}_{hkl})}{l}, & \text{if } s = s_{hkl} \wedge l \neq 0 \wedge |\lambda_i| < 1 \\ \delta(0) \frac{\boldsymbol{\Psi}(s_{hkl})}{s_{hkl}}, & \text{if } s = s_{hkl} \wedge l = 0 \wedge |\lambda_i| < 1 \\ \delta(0) \frac{\mathbf{G}^{*T}\mathbf{TF}}{s_{hkl}}, & \text{if } s = s_{hkl} \wedge |\lambda_i| \geq 1 \\ 0, & \text{if } s \neq s_{hkl} \end{cases}. \quad (2.85)$$

Equation 2.85 allows the powder pattern to be plotted directly. Several examples of this for the pervasive example of nickel, outlined in Section 2.1, are presented in Figure 2.20. The intensity distributions shown were simulated by assuming unpolarized characteristic radiation of copper (equation 2.3 with $Q = 0$ and $\lambda = 1.54059$ Å). Figure 2.20 features the same three theoretical nickel samples featured in Figure 2.19. Rather than showing the diffracted intensity as a function of $\mathbf{s}$ as in Figure 2.19, Figure 2.20 shows the powder intensity as a function of s or θ. Bragg peaks associated with a delta distributions in equation 2.85 have again been given an artificial observable width by introducing a detuning parameter of 0.001, following Treacy *et al.* [88].

Speaking more empirically, it is known that instrumental aberrations and deviations from perfect crystallinity both act as convolutions to smear the diffracted intensity [12]. If an empirical profile function $P(s)$ is adopted to approximate this effect, the smeared powder intensity distribution can be written as

$$I_{\text{empirical}}(s) = P(s) * I(s) = \sum_{hk} \int P(s - s_{hkl}) I(s_{hkl}) \, \mathrm{d}s_{hkl}. \quad (2.86)$$

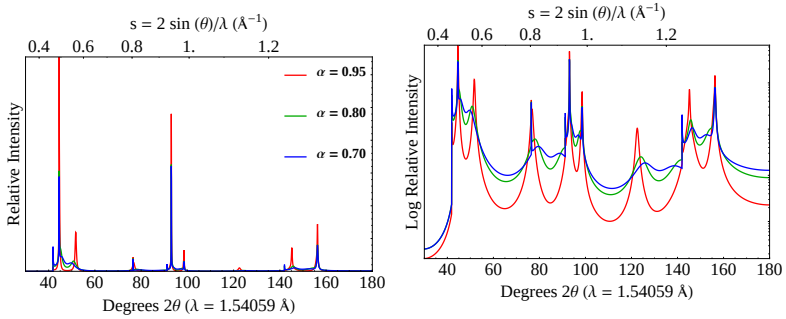

(a) Linear scale

(b) Log scale

Figure 2.20: Different ensemble-averaged diffraction datasets, from powders of linearly disordered, infinite nickel crystals. Each dataset corresponds to a different likelihood of a forward transition.

It is possible to substitute any broadening function for $P(s)$ in equation 2.86. If an entirely empirical approach is sought, simple empirical profiles can be substituted. If a semi-empirical approach is desired, and the additional broadening is assumed to be due to the finite size of the domains, the shape profile function associated with the tangent plane approximation from equation 2.52 in Section 2.5.5 can be substituted into equation 2.86, allowing the broadened intensity to be written as

$$I_{CVF}(s) = \sum_{hk} \int \int A\left(\left(\mathbf{L} \cdot \hat{\mathbf{s}}_{hkl}\right) \hat{\mathbf{s}}_{hkl}\right) \cos\left(2\pi \left(\mathbf{s} \cdot \hat{\mathbf{s}}_{hkl} - s_{hkl}\right) L\right) \mathrm{d}L \, I\left(s_{hkl}\right) \, \mathrm{d}s_{hkl}. \tag{2.87}$$

For scattering vectors which cause equation 2.84 to evaluate to a Delta distribution (see equation 2.85), the convolution in equations equation 2.86 and equation 2.87 act to shift the broadening profile to that specific scattering vector. For other scattering vectors, the convolution must be evaluated numerically.

If finite domains are assumed to show a spherical morphology with a log-normal distribution of diameters, equation 2.47 can be substituted

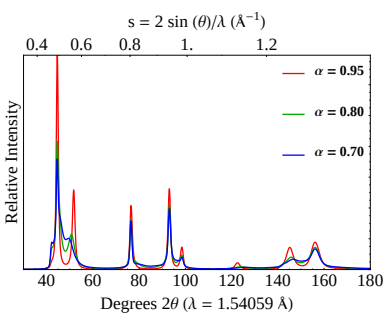

(a) Linear scale

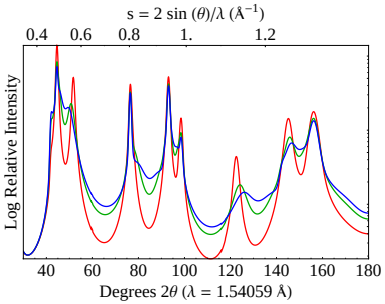

(b) Log scale

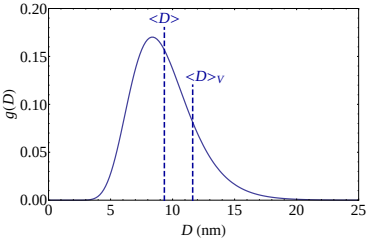

(c) Log-normal distribution describing domain diameter

Figure 2.21: The ensemble-averaged diffracted intensity distribution resulting from nickel powders composed of one-dimensionally disordered, spatially finite nickel crystals. Shown are three different likelihoods of a forward transition. Each diffracted intensity distribution has been convolved by a shape profile function corresponding to the distribution in (c), assuming a spherical morphology. This serves to approximate the diffraction effect of finite domain size.

into equation 2.87. Examples of this specific case are presented in Figure 2.21. Shown are the same intensity distributions depicted in Figure 2.20 after semi-empirically broadening assuming that the domains in the sample show a spherical morphology with the log-normal distribution of diameters shown in Figure 2.21c. The approach provides a physical method with which to approximate ensemble-averaged diffracted intensity from powders of finite domains showing different degrees of one-dimensional disorder.

Using a similar approach, the amount of stacking disorder can be held constant and the effect of changing the domain size distribution can be shown. This is the focus of Figure 2.22, where the likelihood of a forward transition in a nickel powder is held constant at a 0.95. The single intensity distribution is then broadened as per equation 2.87 by assuming spherical domain morphologies with diameters governed by the three different size distributions in Figure 2.22c.

By closely observing the log and linear scale plots in Figures 2.22b and 2.22a, respectively, it is possible to notice that small differences exist in the three resulting intensity distributions. The convolution acts to broaden the delta distributions extensively, while the portion of the powder intensity already broadened by the effect of the disorder are also broadened, but to a lesser extent. It should be emphasized that all differences between the plots in Figure 2.22c are due only to the powder diffraction effect of domain size. By adopting this approach, it is should be possible to discern the independent effects of stacking disorder and finite domain size in experimental data.

2.7 Spatially finite crystals with one-dimensional disorder

In this section, a general three-dimensional shape function as as proposed by Ewald [22] and shown in Section 2.5.1 is applied to the electron density of a stack of layers composing a infinite crystal. This has the effect of mixing some features of various different, existing diffraction modeling approaches [93]. Previous work along this line has employed only a two-dimensional shape function to alter only the domain layers, leading to a restriction to only prismatic shapes [14, 94], or introduced unnecessary and unphysical complications into the

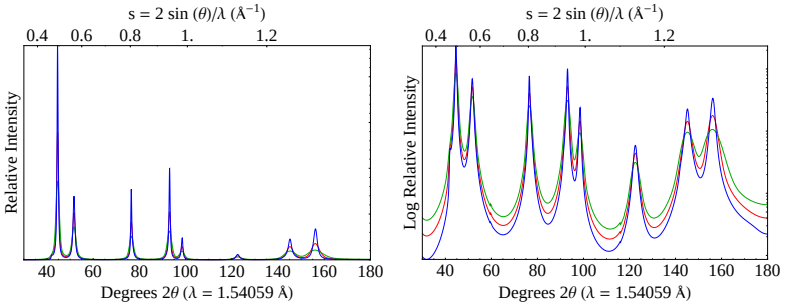

(a) Linear scale (b) Log scale

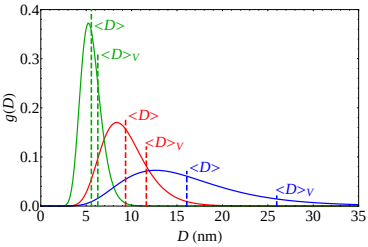

(c) Log-normal distributions describing domain diameters

Figure 2.22: The ensemble-averaged diffracted intensity distribution resulting from a nickel powder composed of one-dimensionally disordered, spatially finite nickel crystals. For each distribution, a 0.95 likelihood of a forward transition was assumed. Each diffracted intensity distribution has been convolved with a different shape profile function, corresponding in color to the distributions in (c), assuming a spherical morphology. This serves to approximate the powder diffraction effect of finite domain size.

definition of a atomic layer [95]. By using a three-dimensional shape function, all of the previous principles outlined in Section 2.5 can be used for finite crystals showing one-dimensional disorder.

2.7.1 Electron density

As in Section 2.5, this section begins by acknowledging that crystals are finite, not infinite objects. To create a spatially bound crystal characterized by stacking disorder, the general three-dimensional shape function $\sigma(\mathbf{r})$ as described by equation 2.25 in Section 2.5.1 is applied to the electron density of the spatially infinite, disordered crystal detailed in Section 2.6.1 and identified by equation 2.58.

It should be specified that an initial assumption is that the total number of layers in the domain N is large enough that the spatial extent of the stack is greater than the spatial extent of domain volume V_c along the stacking direction $\hat{\mathbf{z}}$. In practice this is trivial, as the diffracted intensity will in any case be taken as $\lim_{N\to\infty}$. It is also useful to translate the shape function to an arbitrary point $\mathbf{t}$ to ensure that it is within the spatial extent of the domain.

The same Markov chain description outlined in Section 2.6.1 is used to handle layer stacking. The atoms rather than the unit cell are taken as the smallest building block of the layer. This entails a redefinition of the electron density function for layer type i as

$$\rho_i(\mathbf{r}) = \sum_{p_i=1}^{n_i} U_{p_i}(r) * \Big(z(\mathbf{r} - \mathbf{r}_{p_i})\, \sigma(\mathbf{r} - \mathbf{t}) \Big), \tag{2.88}$$

similar to the new definition of the spatially finite perfect crystal provided by Ino and Minami [13] outlined in Section 2.5.1

This modified layer electron density can again be used to build a linearly disordered crystal, as in Section 2.6, by summing translated layers. Thus to describe a general N-layer domain, where N is large, built as a stack of the arbitrary layer types $ijk\ldots$, the domain electron density can be written as a sum of translated modified layer electron

densities

$$\rho^{(N)}_{ijk\ldots}(\mathbf{r}) = \sum_{p_i=1}^{n_i} U_{p_i}(r) * \Big(z(\mathbf{r}-\mathbf{r}_{p_i})\,\sigma(\mathbf{r}-\mathbf{t}) \Big) + \sum_{p_j=1}^{n_j} U_{p_j}(r) * \Big(z(\mathbf{r}-\mathbf{r}_{p_j}-\mathbf{R}_{ij})\,\sigma(\mathbf{r}-\mathbf{t}) \Big) + \sum_{p_k=1}^{n_k} U_{p_k}(r) * \Big(z(\mathbf{r}-\mathbf{r}_{p_k}-\mathbf{R}_{ij}-\mathbf{R}_{jk})\,\sigma(\mathbf{r}-\mathbf{t}) \Big) + \cdots \quad (2.89)$$

again, occurring with $p_i\alpha_{ij}\alpha_{jk}\ldots$ probability.

2.7.2 Scattering

As in all previous sections on scattering, the kinematic scattered wave amplitude is the FT of the electron density of the domain, and can be written as

$$\varphi^{(N)}_{ijk\ldots}(\mathbf{s}) = \mathcal{F}\left[\rho^{(N)}_{ijk\ldots}(\mathbf{r})\right] = \mathcal{F}\left[\sum_{p_i=1}^{n_i} U_{p_i}(r) * \Big(z(\mathbf{r}-\mathbf{r}_{p_i})\,\sigma(\mathbf{r}-\mathbf{t}) \Big)\right] + \mathcal{F}\left[\sum_{p_j=1}^{n_j} U_{p_j}(r) * \Big(z(\mathbf{r}-\mathbf{r}_{p_j}-\mathbf{R}_{ij})\,\sigma(\mathbf{r}-\mathbf{t}) \Big)\right] + \mathcal{F}\left[\sum_{p_k=1}^{n_k} U_{p_i}(r) * \Big(z(\mathbf{r}-\mathbf{r}_{p_k}-\mathbf{R}_{ij}-\mathbf{R}_{jk})\,\sigma(\mathbf{r}-\mathbf{t}) \Big)\right] + \cdots \quad (2.90)$$

Each term of the sum in equation 2.90 can be rewritten

$$\begin{aligned}
&\mathcal{F}\left[\sum_{p_j=1}^{n_j} U_{p_j}(r) * \left(z\left(\mathbf{r}-\mathbf{r}_{p_j}-\mathbf{R}_{ij}\right)\sigma(\mathbf{r}-\mathbf{t})\right)\right] \\
&= \sum_{p_j=1}^{n_j} \mathcal{F}\left[U_{p_j}(r)\right]\left(\mathcal{F}\left[z\left(\mathbf{r}-\mathbf{r}_{p_j}-\mathbf{R}_{ij}\right)\right] * \mathcal{F}\left[\sigma(\mathbf{r}-\mathbf{t})\right]\right) \\
&= \sum_{p_j=1}^{n_j} f_{p_j}(s)\left(\left(Z(\mathbf{s})\, e^{-2\pi\imath\mathbf{r}_{p_j}\cdot\mathbf{s}} e^{-2\pi\imath\mathbf{R}_{ij}\cdot\mathbf{s}}\right) * \left(S(\mathbf{s})\, e^{-2\pi\imath\mathbf{t}\cdot\mathbf{s}}\right)\right).
\end{aligned} \tag{2.91}$$

A word should be devoted to the second factor in equation 2.91. It represents a RS convolution between the lattice of Dirac rods, as shown in Figure 2.18, and the three-dimensional shape profile function. It can be written explicitly as

$$\begin{aligned}
&\left(Z(\mathbf{s})\, e^{-2\pi\imath\mathbf{r}_{p_j}\cdot\mathbf{s}} e^{-2\pi\imath\mathbf{R}_{ij}\cdot\mathbf{s}}\right) * \left(S(\mathbf{s})\, e^{-2\pi\imath\mathbf{t}\cdot\mathbf{s}}\right) = \\
&\sum_{hk}\int\left(\delta(\boldsymbol{\tau}-\mathbf{s}_{hkl})\, e^{-2\pi\imath\mathbf{r}_{p_j}\cdot\boldsymbol{\tau}} e^{-2\pi\imath\mathbf{R}_{ij}\cdot\boldsymbol{\tau}}\right)\left(S(\mathbf{s}-\boldsymbol{\tau})\, e^{-2\pi\imath\mathbf{t}\cdot(\mathbf{s}-\boldsymbol{\tau})}\right)\mathrm{d}V_{\boldsymbol{\tau}},
\end{aligned} \tag{2.92}$$

where $\mathbf{s}_{hkl}$ implicitly depends on $\boldsymbol{\tau}$, as $\mathbf{s}_{hkl} = \mathbf{s}_{hk} - l\hat{\mathbf{Z}}$ (equation 2.66), and l represents the component of $\boldsymbol{\tau}$ which does not lie in the plane spanned by $\mathbf{a}^*$ and $\mathbf{b}^*$.

Unlike the convolution involving the RS lattice of Dirac distributions in equation 2.30, the convolution in equation 2.92 is not completely analytic. It can be evaluated analytically *only* in the dimensions associated with the periodicity of the lattice of Dirac rods, along $\mathbf{a}^*$ and $\mathbf{b}^*$, when $\boldsymbol{\tau} = h\mathbf{a}^* + k\mathbf{b}^* + l\hat{\mathbf{Z}}$. The convolution in the dimension along the rods $\hat{\mathbf{Z}}$ is however *not* analytic and must be left unevaluated. The

convolution can be rewritten as

$$\left(Z\left(\mathbf{s}\right)e^{-2\pi\imath\mathbf{r}_{p_j}\cdot\mathbf{s}}e^{-2\pi\imath\mathbf{R}_{ij}\cdot\mathbf{s}}\right)*\left(S\left(\mathbf{s}\right)e^{-2\pi\imath\mathbf{t}\cdot\mathbf{s}}\right)=$$
$$\sum_{hk}\int S\left(\mathbf{s}-\mathbf{s}_{hkl}\right)e^{-2\pi\imath\mathbf{r}_{p_j}\cdot\mathbf{s}_{hkl}}e^{-2\pi\imath\mathbf{R}_{ij}\cdot\mathbf{s}_{hkl}}e^{-2\pi\imath\mathbf{t}\cdot\mathbf{s}}e^{2\pi\imath\mathbf{t}\cdot\mathbf{s}_{hkl}}\,\mathrm{d}l$$

This convolution can be substituted back into equation 2.91 to rewrite the FT of the atomic layer as

$$\sum_{p_j=1}^{n_j}f_{p_j}\left(s\right)\left(\left(Z\left(\mathbf{s}\right)e^{-2\pi\imath\mathbf{r}_{p_j}\cdot\mathbf{s}}e^{-2\pi\imath\mathbf{R}_{ij}\cdot\mathbf{s}}\right)*\left(S\left(\mathbf{s}\right)e^{-2\pi\imath\mathbf{t}\cdot\mathbf{s}}\right)\right)=$$
$$\sum_{hk}\int S\left(\mathbf{s}-\mathbf{s}_{hkl}\right)\sum_{p_j=1}^{n_j}f_{p_j}\left(s\right)e^{-2\pi\imath\mathbf{r}_{p_j}\cdot\mathbf{s}_{hkl}}e^{-2\pi\imath\mathbf{R}_{ij}\cdot\mathbf{s}_{hkl}}e^{-2\pi\imath\mathbf{t}\cdot\mathbf{s}}e^{2\pi\imath\mathbf{t}\cdot\mathbf{s}_{hkl}}\,\mathrm{d}l. \tag{2.93}$$

However the sum on atoms in the unit cell of layer type j in equation 2.93, $\sum_{p_i=1}^{n_j}f_{p_j}\left(s\right)e^{-2\pi\imath\mathbf{r}_{p_j}\cdot\mathbf{s}_{hkl}}$, can be recognized as the IM structure factor $F_j\left(s,\mathbf{s}_{hkl}\right)$, with a new definition $\mathbf{s}_{hkl}$, incorporating the continuous Miller index l. Using these definitions, the scattered wave amplitude in equation 2.90 can be rewritten as

$$\varphi^{(N)}_{ijk\ldots}\left(\mathbf{s}\right)=\sum_{hk}\int e^{-2\pi\imath\mathbf{t}\cdot\mathbf{s}}e^{2\pi\imath\mathbf{t}\cdot\mathbf{s}_{hkl}}S\left(\mathbf{s}-\mathbf{s}_{hkl}\right)\Big(F_i\left(s,\mathbf{s}_{hkl}\right)+$$
$$F_j\left(s,\mathbf{s}_{hkl}\right)e^{-2\pi\imath\mathbf{R}_{ij}\cdot\mathbf{s}_{hkl}}+F_k\left(s,\mathbf{s}_{hkl}\right)e^{-2\pi\imath(\mathbf{R}_{ij}+\mathbf{R}_{jk})\cdot\mathbf{s}_{hkl}}+\cdots\Big)\,\mathrm{d}l \tag{2.94}$$

The diffracted intensity from this domain is the squared modulus of the scattered wave amplitude, but as in Section 2.6, rather than a domain with any specific $ijk\ldots$ sequence, the true interest is an ensemble-averaged domain considering all layer sequences. In this case an incoherent sum is again taken where each intensity term is weighted by the probability of the specific sequence. Expressed in this way the diffracted intensity distribution can be written as

$$I\left(\mathbf{s}\right)=\sum_{i,j,k\ldots}p_i\alpha_{ij}\alpha_{jk}\ldots\varphi^{(N)}_{ijk\ldots}\left(\mathbf{s}\right)\varphi\left(\mathbf{s}\right)^{(N)}_{ijk\ldots}\left(\mathbf{s}\right)^{*}. \tag{2.95}$$

Writing this explicitly,

$$I(\mathbf{s}) = \sum_{i,j,k\ldots} p_i \alpha_{ij} \alpha_{jk} \ldots \sum_{hk} \int e^{-2\pi\imath \mathbf{t}\cdot\mathbf{s}} e^{2\pi\imath \mathbf{t}\cdot\mathbf{s}_{hkl}} S(\mathbf{s}-\mathbf{s}_{hkl}) \Big(F_i(s,\mathbf{s}_{hkl}) + F_j(s,\mathbf{s}_{hkl}) e^{-2\pi\imath \mathbf{R}_{ij}\cdot\mathbf{s}_{hkl}} + F_k(s,\mathbf{s}_{hkl}) e^{-2\pi\imath(\mathbf{R}_{ij}+\mathbf{R}_{jk})\cdot\mathbf{s}_{hkl}} + \cdots \Big) \,\mathrm{d}l \sum_{h'k'} \int e^{2\pi\imath \mathbf{t}\cdot\mathbf{s}} e^{-2\pi\imath \mathbf{t}\cdot\mathbf{s}_{h'k'l'}} S(\mathbf{s}-\mathbf{s}_{h'k'l'}) \Big(F_i(s,\mathbf{s}_{h'k'l'}) + F_j(s,\mathbf{s}_{h'k'l'}) e^{-2\pi\imath \mathbf{R}_{ij}\cdot\mathbf{s}_{h'k'l'}} + F_k(s,\mathbf{s}_{h'k'l'}) e^{-2\pi\imath(\mathbf{R}_{ij}+\mathbf{R}_{jk})\cdot\mathbf{s}_{h'k'l'}} + \cdots \Big)^* \,\mathrm{d}l'. \tag{2.96}$$

Again, as in Section 2.5.2, the intensity equation can be expanded and rewritten, grouping terms where $hkl = h'k'l'$ or $hkl \neq h'k'l'$,

$$I(\mathbf{s}) = \sum_{i,j,k\ldots} p_i \alpha_{ij} \alpha_{jk} \ldots \Bigg[\sum_{hk} \int |S(\mathbf{s}-\mathbf{s}_{hkl})|^2 |F_i(s,\mathbf{s}_{hkl}) + F_j(s,\mathbf{s}_{hkl}) e^{-2\pi\imath \mathbf{R}_{ij}\cdot\mathbf{s}_{hkl}} + F_k(s,\mathbf{s}_{hkl}) e^{-2\pi\imath(\mathbf{R}_{ij}+\mathbf{R}_{jk})\cdot\mathbf{s}_{hkl}} + \cdots|^2 \,\mathrm{d}l + \sum_{hk\neq h'k'} \sum \iint e^{2\pi\imath \mathbf{t}\cdot(\mathbf{s}_{hkl}-\mathbf{s}_{h'k'l'})} S(\mathbf{s}-\mathbf{s}_{hkl}) \, S(\mathbf{s}-\mathbf{s}_{h'k'l'})^* \Big(F_i(s,\mathbf{s}_{hkl}) + F_j(s,\mathbf{s}_{hkl}) e^{-2\pi\imath \mathbf{R}_{ij}\cdot\mathbf{s}_{hkl}} + F_k(s,\mathbf{s}_{hkl}) e^{-2\pi\imath(\mathbf{R}_{ij}+\mathbf{R}_{jk})\cdot\mathbf{s}_{hkl}} + \cdots \Big) \Big(F_i(s,\mathbf{s}_{h'k'l'}) + F_j(s,\mathbf{s}_{h'k'l'}) e^{-2\pi\imath \mathbf{R}_{ij}\cdot\mathbf{s}_{h'k'l'}} + F_k(s,\mathbf{s}_{h'k'l'}) e^{-2\pi\imath(\mathbf{R}_{ij}+\mathbf{R}_{jk})\cdot\mathbf{s}_{h'k'l'}} + \cdots \Big)^* \,\mathrm{d}l \,\mathrm{d}l' \Bigg]. \tag{2.97}$$

While equation 2.97 may seem intimidating, it can be simplified significantly if an average over all shape function translations $\mathbf{t}$ is taken, by integration $\int I(\mathbf{s}) \,\mathrm{d}\mathbf{t}$, where the dependence of the intensity equation on $\mathbf{t}$ is implicit. The only portion of the integrand that depends

on $\mathbf{t}$ is $e^{2\pi\imath\mathbf{t}\cdot(\mathbf{s}_{hkl}-\mathbf{s}_{h'k'l})}$, a coefficient of the $hkl \neq h'k'l'$ terms, and the integration of this function over all $\mathbf{t}$ is explicitly zero. This means equation 2.97 can be re-written as

$$I(\mathbf{s}) = \sum_{i,j,k\ldots} p_i\alpha_{ij}\alpha_{jk}\ldots\sum_{hk}\int |S(\mathbf{s}-\mathbf{s}_{hkl})|^2|F_i(s,\mathbf{s}_{hkl}) + F_j(s,\mathbf{s}_{hkl})\,e^{-2\pi\imath\mathbf{R}_{ij}\cdot\mathbf{s}_{hkl}} + F_k(s,\mathbf{s}_{hkl})\,e^{-2\pi\imath(\mathbf{R}_{ij}+\mathbf{R}_{jk})\cdot\mathbf{s}_{hkl}} + \cdots|^2\,\mathrm{d}l. \tag{2.98}$$

This can be considered is the "random shift treatment" in the case of one-dimensionally disordered domain described by a general three-dimensional shape function. While it is similar to the work of Ino and Minami or Hosemann and Bagchi [13, 55], these authors did not consider stacking disorder, and this represents the first time it has been shown applicable in this specific case. This treatment has some implications however. Strictly speaking, it implies that true crystal under consideration is not one with only integer numbers of layers, but one with a uniform distribution of total layers (including fractional layers). This assumption could be a problem in the case of materials known to have specific surface termination, such as mixed layer minerals. In such case, explicit termination of the sum on the total number of layers e.g. in equation 2.75 may be preferred over applying a randomly shifted shape function.

Further simplifications are still possible. The shape profile function $|S(\mathbf{s}-\mathbf{s}_{hkl})|^2$ and the RS lattice sum are independent of the specific layer sequence being considered, and can be factored outside the sum on layer types

$$I(\mathbf{s}) = \sum_{hk}\int |S(\mathbf{s}-\mathbf{s}_{hkl})|^2\sum_{i,j,k\ldots} p_i\alpha_{ij}\alpha_{jk}\ldots|F_i(s,\mathbf{s}_{hkl}) + F_j(s,\mathbf{s}_{hkl})\,e^{-2\pi\imath\mathbf{R}_{ij}\cdot\mathbf{s}_{hkl}} + F_k(s,\mathbf{s}_{hkl})\,e^{-2\pi\imath(\mathbf{R}_{ij}+\mathbf{R}_{jk})\cdot\mathbf{s}_{hkl}} + \cdots|^2\,\mathrm{d}l. \tag{2.99}$$

Immediately it can be recognized that the second factor in equation 2.99, associated with the sums on atomic layer types, is identical to the second factor in equation 2.67. Through a process identical to that

taken in Section 2.6.2, equation 2.99 can then be rewritten as

$$I(\mathbf{s}) = \sum_{hk} I_{hk}(\mathbf{s}) \tag{2.100}$$

where

$$\begin{aligned} I_{hk}(\mathbf{s}) &= \int |S(\mathbf{s}-\mathbf{s}_{hkl})|^2 \left(\mathbf{G}^*\boldsymbol{\varphi}^{(\infty)} + \mathbf{G}\boldsymbol{\varphi}^{*(\infty)} - \mathbf{G}^*\mathbf{F}\right) \mathrm{d}l \\ &= \int |S(\mathbf{s}-\mathbf{s}_{hkl})|^2 \boldsymbol{\Psi}(s, \mathbf{s}_{hkl}) \, \mathrm{d}l, \end{aligned}$$

and the vector intensity has been rewritten as $\boldsymbol{\Psi}(s, \mathbf{s}_{hkl})$.

In this equation, the vectors take on a slightly different definition when compared to those for the infinite crystal case outlined in Section 2.6.2. $\mathbf{F}$ is redefined as a vector of the new *IM layer structure factors* as outlined in Section 2.5.2, here depending on the *continuous* Miller index l, as outlined earlier in this section, $\mathbf{F} \equiv [F_i(s, \mathbf{s}_{hkl})]$. Similarly, $\mathbf{G}$ is redefined as a vector of stationary distribution weighted IM structure factors, $\mathbf{G} \equiv [p_i F_i(s, \mathbf{s}_{hkl})]$. $\boldsymbol{\varphi}^{(\infty)}$ is also redefined as $(\mathbf{I}-\mathbf{T})^{-1}\mathbf{F}$, using the new definition of $\mathbf{F}$ and a new definition of the phase weighted transition matrix $\mathbf{T} = \left[\alpha_{ij} e^{-2\pi\imath \mathbf{R}_{ij}\cdot\mathbf{s}_{hkl}}\right]$.

The two terms in equation 2.100 have both been seen before, $|S(\mathbf{s}-\mathbf{s}_{hkl})|^2$ represents the shape profile function, and can be computed quite generally as outlined in both Section 2.5.3 and Section 2.5.4. The second term in equation 2.100 is nearly identical to the second term in equation 2.78, and represents the diffracted intensity distribution of a perfect, infinite crystal that is disordered along one dimension.

The integral in equation 2.100 has the form of a convolution, and is a result of the Dirac rod form of the RS lattice, as described earlier in this and the previous sections (equation 2.66 and equation 2.93). The convolution is over only one RS direction, namely the continuous Miller index l. Thus each hk rod in equation 2.100 is a convolution of the shape profile function along the length of the rod, expressed by the continuous Miller index l.

An example of the application of equation 2.100 is shown in Figure 2.23, where the typical example of nanocrsytalline nickel, outlined Section 2.1, is again considered. A three-dimensional rendering of the

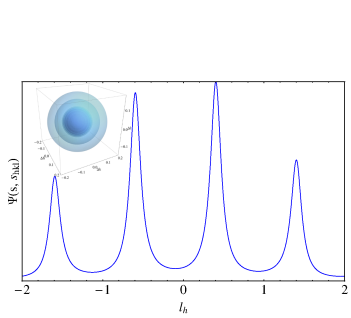

(a) $\mathbf{\Psi}(s, \mathbf{s}_{hkl})$ and $|S(\mathbf{s})|^2$ (inset)

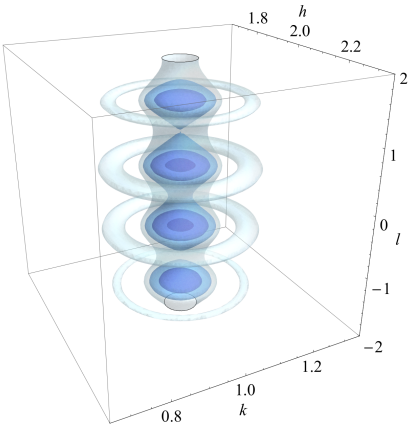

(b) Intensity in RS

Figure 2.23: Averaged diffracted intensity of the $(12)_l$ rod in three-dimensional RS for an ensemble of finite, one-dimensionally disorder nickel domains

shape profile function, $|S(\mathbf{s} - \mathbf{s}_{hkl})|^2$, resulting from a 10 nm spherical domain is shown inset in Figure 2.23a, along with the value of $\mathbf{\Psi}(s, \mathbf{s}_{hkl})$ along the $(12)_l$ rod, considering the remapped Miller indices. The nickel domain considered in the figure shows a 25% chance of an interruption in the normal stacking sequence. Figure 2.23b shows a three-dimensional rendering of the convolution of the two objects shown in Figure 2.23a, representing the averaged diffracted intensity distribution of a partially disordered ensemble of 10 nm nickel domains.

2.7.3 Powder averaging

Again, if a randomly oriented powder rather than a perfectly oriented ensemble is of interested, then it is necessary to take a weighted orientation average of equation 2.100. The the powder intensity is then

written as

$$I(s) = \frac{1}{4\pi s^2} \iint_S I(\mathbf{s}) \, \mathrm{d}S \tag{2.101}$$

$$= \frac{1}{4\pi s^2} \sum_{hk} \int_0^{2\pi} \int_0^{\pi} \int \left| S(\mathbf{s} - \mathbf{s}_{hkl}) \right|^2 \mathbf{\Psi}(s, \mathbf{s}_{hkl}) \, \mathrm{d}l s^2 \sin\theta \, \mathrm{d}\theta \, \mathrm{d}\phi \qquad \int \int_0^{2\pi} \int_0^{\pi} \int_0$$

It is important here to recall the functional dependence of each term. In Section 2.5.5, the structure factor term $F(s, \mathbf{s}_{hkl})$ in the powder integration in equation 2.49 could be factored outside of the integral, as it had no dependence on the direction of the scattering vector $\mathbf{s}$. This is not true in equation **??**, as the recursive intensity distribution $\mathbf{\Psi}(s, \mathbf{s}_{hkl})$ depends implicitly upon $\mathbf{s}$, as $\mathbf{s}_{hkl} = h\mathbf{a}^* + k\mathbf{b}^* + l\hat{\mathbf{Z}}$, where l is the projection of $\mathbf{s}$ along the length of the (hk) rod.

Again, analytic solutions to this integral have not been found, but the powder intensity can be approximated on tangent cylinders. This entails rewriting the differential surface element as $\mathrm{d}S = s \, \mathrm{d}\theta \hat{\mathbf{s}} \cdot \hat{\mathbf{s}}_{hkl}$ rather than $\mathrm{d}S = s^2 \sin\theta \, \mathrm{d}\theta \, \mathrm{d}\phi$. This was originally proposed by Warren [96], but it was only ever applied for the case where each layer was the same shape (i.e prismatic domains).

In practice it is often not necessary to evaluate or approximate equation **??**. Rather, equation 2.87 can be used with the appropriate profile function. This is the approach adopted throughout this work.

2.8 Concluding remarks

Having gone through the extremely repetitive derivations presented in this chapter, at least one thing should be obvious: when attempting to model diffraction for the purpose of data fitting, there are a variety of different approaches which can be taken. The key point however is that each approach is itself based on sets of fundamental assumptions. These assumptions must be kept in mind, as the degree to which they are satisfied essentially governs the accuracy and reliability of the approach. An attempt to apply models in cases where the fundamental assumptions are not satisfied can be at best unproductive, and at worst misleading.

Fundamentally, every equation in this chapter (and this thesis) share some common assumptions. Namely, it is assumed that X-rays scatter elastically and kinematically without anomalous scattering, that the scattered X-rays are observed far from the scattering event, and that atomic electron clouds are spherically symmetric and react to perturbations much more quickly than the static atomic nuclei. Some of these assumptions can be relaxed with a minimum of modifications to the equations contained herein: for example, thermal motion of atoms can be incorporated by assuming a harmonic bond potential, leading to a a Debye-Waller thermal factor, and anomalous scattering can be incorporated by correcting the atomic form factor, as hinted at in Section 2.3. Conversely, fully casting off other assumptions, such as that of kinematical scattering, would require significant re-working of the ideas presented here.

The above common assumptions can be used without further additions if DS approaches are used to compute the diffracted intensity. This is the most general and often most computationally expensive approach, and is covered in Chapter 3. Adopting more computationally efficient models entails the imposition of more specific assumptions. For example, by assuming a degree of periodicity within the domains constituting the samples, it is possible to work in a Fourier transformed reciprocal space. Such RS approaches were the main focus of this chapter.

The equations outlined in Section 2.4 are a result of assuming that the scattering objects are three-dimensionally periodic and spatially unbounded. Practically speaking, it was seen that such objects generally result in a diffracted intensity distribution that is also three-dimensionally periodic and composed of weighted Delta distributions. Powder averaging results in a powder diffraction pattern such as that presented in Figure 2.6b. An empirical broadening function can be applied, as seen in Figure 2.6a, to approximate small deviations from the assumptions of this section. The choice of broadening function is however not generally objective, and most functions have little basis in the actual physics of diffraction. Furthermore, this method of approximation retains a form of the Lorentz factor which is strictly only applicable under the assumptions of this section.

In Section 2.5, the condition of spatial unboundedness was relaxed. It

was assumed that domains can be represented following the work of Ino and Minami [13], and that such spatially finite crystals show an "averaged" surface termination. Under such assumptions, the diffracted intensity distribution is a three-dimensionally periodic lattice composed of weighted shape profile functions, where each shape profile function can be thought of as the FT of the crystal shape autocorrelation function. In this section explicit expressions for the powder diffraction pattern were given under the assumption that the powder integration sphere could be approximated locally as a tangent plane following Stokes and Wilson [23].

It was seen that considering only the finite size of the crystals implied that Bragg peaks can be apparently shifted out of Bragg position in the powder pattern, and that line profiles themselves expressed as a function of scattering angle are intrinsically asymmetric. The degree of shift and asymmetry is dependent on the details of both the atomic scale structure and the morphology of the domains [13]. Such details are necessarily difficult to capture when approximating the profile shape with empirical broadening functions as per Section 2.4.3, as this approach has no intrinsic capability to capture these effects, whereas the models of Section 2.5 handle the effects explicitly.

In Section 2.6, the assumption of three-dimensional periodicity imposed in Sections 2.4 and 2.5 was relaxed. Diffraction from objects built a stacks of two-dimensionally periodic objects was considered. A Markov chain description was adopted to describe the arrangements of the layers [14, 88, 90–92] out of *convenience only*, and allowed for the computation of the diffracted intensity considering a weighted average of *all possible configurations* [88]. It was seen that in such a situation, the diffracted intensity distribution becomes continuously distributed along Bragg rods which extend parallel to the stacking direction in RS, rather than being concentrated in isolated Bragg spots as was seen in the case of Sections 2.4 and 2.5. The nature of this continuously diffracted intensity depends on the atomic scale layers, how they are arranged, and the likelihood of each arrangement. In this way, atomic and nanoscale structure are considered together directly to give the diffracted intensity distribution.

The work of Treacy *et al.* [88] was followed closely to derive new expressions for the powder- and ensemble-averaged intensity from a

linearly disordered spatially infinite crystal. A new physical approach was shown to approximate the powder diffraction effect of finite crystals in the case of one-dimensionally disordered domains. In this way, atomic, nano, and microscale structure are considered together directly to give the powder pattern.

In Section 2.7, the three-dimensional shape function approach used to describe a finite crystal, as proposed by Ino and Minami [13] was applied to the generally linearly disordered spatially infinite crystal outlined in Section 2.6, without introducing unnecessary and unphysical complications into the definition of a atomic layer [95]. By using a Markov framework as in Section 2.6 a weighted average of *all possible configurations* was considered to compute the diffracted intensity. This led to a partially analytic convolution operation, and a new description for the weighted average diffracted intensity of an ensemble of linearly disordered spatially finite crystals. In this situation, powder averaging was only explored briefly.

It is essential to understand that across all the RS approaches discussed in this chapter, an inherit assumption is that sample properties, such as the domain size, the lattice parameters, or the layer-layer transition probabilities, are all *uncorrelated*. For example, when the diffraction effect of a polydisperse domain size was worked out in Section 2.5.4, each domain, regardless of size, is assumed to be characterized by the *same* unit cell. As another example, when the combined diffraction effect of stacking disorder within polydisperse domains was explored in Section 2.7.1, each domain, regardless of size, was assumed to be characterized by the *same* set of layer unit cells and the *same* overall layer-layer correlation properties.

While these assumptions may be valid in large crystals, it is well known that they generally do not hold for nanomaterials. The volume fraction of under-coordinated surface species increases super-linearly as domain size decreases, and these under-coordinated species tend to relax, leading to domain size dependent bond distances and thus lattice parameters of nanomaterials which can deviate significantly from that seen in the bulk [97–100]. Furthermore, the energy needed to interrupt a normal stacking sequence is characteristically described per unit area. As domain size decreases, cross sectional area of the domain also decreases, implying that the energy necessary “per fault”

decreases. This naturally implies that layer-layer correlation probabilities will vary with domain size.

It is possible to approximate correlation between material properties using a RS approach by considering each unique set of properties as describing a separate phases, but for complex systems this is rarely tractable, and the additional model complexity introduced is likely not justified in terms of improved understanding and/or reproduction of experimental data.

This is not to say that the equations in this chapter are useless, it is only to add a grain of salt to the optimism one might experience after seeing such direct modeling approaches. The equations in this chapter are useful insofar as the assumptions are kept in mind, and one is careful not to over interpret the results if they are used to fit real diffraction data. They offer a starting point for understanding, and can shed light on fine details of the atomic, nano, and microstructure of a sample, but this information can be skewed by a plethora of factors and should not be taken literally.

In the next chapter, a series of virtual diffraction experiments are carried out to obtain synthetic (simulated) powder diffraction data from a set of atomistically represented nanocrsytalline nickel powders. Some of the different modeling approaches proposed in this chapter are applied in an attempt to both fit this powder diffraction data and understand the physical characteristics of the powders.

Chapter 3

Virtual powders: proof of concept

While some the expressions and associated derivations in the previous chapter may seem strictly academic, it is in fact possible to use them to explicitly compute the diffracted intensity from an ensemble [20, 26–28]. It is of course interesting and important to compare the accuracy and precision of these computations to what is measured from a real sample, but a real sample itself introduces several other complicating factors that have not been addressed in the previous chapter. For example, nowhere in the previous chapter were the specifics of the measurement instrument reviewed. The physical imperfections or aberrations of the instrument can affect both the shape, position, and relative profile intensity of the measured intensity distribution [9, 10, 101]. Furthermore, the absorption [9, 102] of a real sample measured in both reflection or transmission can also influence these things. However, the ultimate goal of this work is to understand how fine details of the diffracted intensity are influenced by the *sample* and not the *instrument*. For this reason it is desirable to conduct an idealized virtual diffraction experiment, where no instrumental effect is seen.

While eliminating the effect of the instrument is reason enough to conduct a virtual diffraction experiment to test the models in Chapter 2, another unintended benefit of a virtual experiment is *a priori* knowledge of the correct sample characteristics, a benefit exploited by Beyerlein *et al.* in similar work [103]. Few characterization techniques exist that provide accurate and statistically complete information on sample chemistry and structure spanning many length scales [104]. In-

formation of particular interest could include the contents and shape of periodic units, the extent of and type of stacking disorder, or details of domain morphology (domain shape, distribution of size parameters).

Total scattering approaches are often able to provide some information on stacking disorder [105–107] but can fall short at describing the statistics of a sample, often treating the sample as a powder of identical or nearly identical objects [105, 108, 109]. While this approximation is accurate for ensembles with tightly controlled properties, it may not be suitable for powders with broad domain size distributions or significant defect clustering. X-ray absorption spectroscopy can provide a plethora of information on *local* coordination environment, but useful information often does not extend beyond the second or third coordination sphere [110, 111], meaning morphology information or longer range patterns in stacking could be missed.

A common characterization method is scanning or transmission electron microscopy. With automated image analysis [112, 113], these techniques can yield unbiased and accurate morphology information and domains size distributions [114, 115]. It is also possible to locally identify and quantify atomic scale defects, such as twin boundaries and stacking faults [116, 117], two manifestations of the stacking disorder outlined in Section 2.6.

Electron microscopy probes are however not ideally suited for quantifying sample atomic, nano and microstructure. Accurately imaging CSDs or defects can be a quite laborious, expensive, and subjective task, and ultimately provides only two-dimensional projections of three-dimensional objects. Although procedural standards exist [118], micrographs are inevitably collected at the subjective discretion of microscope operator. Furthermore, when the possible configuration space of the specimen is large, as with complex disorder or broad size distributions, the population size necessary to accurately estimate sample properties can easily become unfeasibly large [119]. For these reasons electron micrographs are often presented without quantification, used only to indicate a general morphology or the *presence* of defects [120–124], and quantitative results have even occasionally been the subject of contention [116, 125, 126].

With this motivation, *virtual powder* samples were created. Each virtual powder is a collection of atomistic domains synthesized through a

random sampling of different distributions or stochastic processes, as outlined in Section 3.1. By carrying out a virtual diffraction experiment using these virtual powders as outlined in Section 3.2, synthetic powder diffraction data which approximates the ensemble average is obtained and discussed. In Section 3.3, the accuracy and validity of different approximations utilized in the RS approaches outlined in Chapter 2 is assessed by fitting the synthetic powder diffraction data, a process already established in the literature [103]. This section also discusses the effect on the diffracted intensity of different micro and nanostructural features.

3.1 Synthesis

This section gives an overview of the process of synthesizing a virtual powder sample. As the ultimate goal of this chapter is not characterizing real samples but only comparing RS diffraction models, the characteristics of the specific virtual powder samples are completely invented. It is important to note though that this process could be equally repeated based on characteristics *refined* from actual powder diffraction data. The resulting virtual powder sample could then be utilized within atomistic simulations, driven by classical molecular dynamics or density functional theory. With such an approach, it may be possible to abandon some assumptions imposed by working in RS, such as the lack of correlation between sample parameters.

3.1.1 Selecting the appropriate models

To synthesize virtual powder samples, it is first necessary to select the material of interest. Throughout this thesis nickel metal has been generally adopted as a model system for its relative simplicity, and for its tendency to adopt both the fcc and hcp polytypes within the nanocrystalline form [42]. The atomic structure and stacking scheme of nickel are described at length in Section 2.1.

After the choice of material, the domain morphology and the form of the domain size distribution should be chosen. Here equi-axial (spherical) domains with log-normally distributed diameters are chosen. While this assumption is made in the interest of simplicity, it

also happens that nanocrystalline nickel very frequently adopts an approximately spherical morphology [127–129], and that log-normal distributions have been found to accurately describe the sizes of domains in may cases [59]. These choices introduce considerable simplifications into the actual computation, and conveniently reduce the number of parameters necessary to describe the whole virtual powder. Particularly, the CVF is analytic and isotropic for a log-normal distribution of spheres. The exact form of this was first given by Scardi and Leoni, but is presented in this work in equation 2.47 [26].

It should be highlighted that the methods for directly computing the powder intensity distribution outlined in Chapter 2 are rather general: no restrictions or assumptions were made on the symmetry of the crystal lattice or unit cell, nor on the crystal morphology or distributions of dimension parameters, aside from an assumption that these parameters are all uncorrelated.

For samples showing stacking disorder, as investigated here, it is also necessary to identify constituent layer structures as well as physically and chemically reasonable stacking vectors. For the fcc and hcp polytypes, Warren [21] has done an excellent job of both tasks, and a summary of this was presented in Section 2.1.

Having established constituent layer structures and associated layer-layer translations, an appropriate description of the correlations between adjacent layers must be chosen. For a Markov description as per Section 2.6, this amounts to choosing the order n of the Markov process. In plain terms, in an n^{th}-order Markov process the identity of the i^{th} state is dependent on the identity of n previous states. That is

$$\Pr\left(X_i = x_i | X_{i-1} = x_{i-1}, X_{i-2} = x_{i-2}, X_{i-3} = x_{i-3} \ldots X_{i-n} = n_{i-n}\right)$$

In terms of the application of Markov chains to modeling diffraction, Jagodzinski coined the term "Reichweite number" R for describing the range of the layer-layer interactions [85]. R is equivalent to the order n of the Markov process necessary for modeling the layer sequence.

In the context of the description of nickel outlined in Section 2.1, the Markov process has two states, associated with the two possible transitions, forward f or backward b. The transition probability matrix $\mathbf{P}$ describes the likelihood of state to state transitions, and is a right stochastic matrix, meaning the entries of each row sum to unity.

For zeroth-order Markov process, or $R = 0$ stacking, f and b transitions are equally likely, and the probability matrix can be written as

$$\mathbf{P} = \begin{bmatrix} 0.5 & 0.5 \\ 0.5 & 0.5 \end{bmatrix}. \tag{3.1}$$

This only implies an equal *probability* of either translation, and leads to fcc and hcp that are *on average* just one atomic layer thick. The stochastic nature of the Markov process however *does allow* for successive (repeated) f or b transitions, leading to fcc and hcp bands that are larger than just one atomic layer (see e.g. figures 3.3, 3.4, or 3.7). The finite state-machine for this Markov process is shown in Figure 3.1.

For the case of a first-order Markov process, or $R = 1$ stacking, the likelihood of an f or b transition is only dependent on the identity of the current state, and there is one linearly independent probability α_f describing the likelihood of an f transition between any two layers. Figure 3.1 shows the finite state-machine for this Markov process. The associated probability matrix can be written as

$$\mathbf{P} = \begin{bmatrix} \alpha_f & \alpha_b = 1 - \alpha_f \\ \alpha_f & \alpha_b = 1 - \alpha_f \end{bmatrix}. \tag{3.2}$$

For the case of a second-order Markov process, or $R = 2$ stacking, the likelihood of an f or b transition is dependent on the current and previous states. This memory effect can be achieved by judicious definition of the probability matrix. It can be seen in equation 3.2 that the only way to reach the Markov state associated with the first row of the probability matrix is through an f transition, while the only way to reach the Markov state associated with the second row of the probability matrix is through a b transition. In equation 3.2 the probably of either transition is however independent of *which* path was taken previously (both states show the same probabilities). By splitting the states and introducing two independent probabilities, the probability of an f transition given a preceding f transition, written α_{ff}, and the probability of an f transition given a preceding b transition, written α_{bf}, a memory effect can be imposed. The finite state-machine for this Markov process is shown in Figure 3.1, and the resulting transition

probability matrix can be written as

$$\mathbf{P} = \begin{bmatrix} \alpha_{ff} & \alpha_{fb} = 1 - \alpha_{ff} \\ \alpha_{bf} & \alpha_{bb} = 1 - \alpha_{bf} \end{bmatrix}. \tag{3.3}$$

Going further, any n^{th}-order Markov process can be represented as a first-order Markov process with an expanded state space and constrained transition probabilities. For example, a third-order Markov process for the nickel system considered here, with the two states associated with the transitions f and b, can be represented by a first-order Markov process with the four states ff, bf, fb and, bb. In this approach, each state in the expanded state space has a forced history: state ff can only be reached as a result of two f transitions, state bb can only be reached as a result of two b transitions, and so on. The probability matrix for such a Markov process is written as

$$\mathbf{P} = \begin{bmatrix} \alpha_{fff} & 0 & \alpha_{ffb} = 1 - \alpha_{fff} & 0 \\ \alpha_{bff} & 0 & \alpha_{bfb} = 1 - \alpha_{bff} & 0 \\ 0 & \alpha_{fbf} & 0 & \alpha_{fbb} = 1 - \alpha_{fbf} \\ 0 & \alpha_{bbf} & 0 & \alpha_{bbb} = 1 - \alpha_{bbf} \end{bmatrix} \tag{3.4}$$

The "memory" associated with the third-order Markov process is contained within the transition probability matrix itself. For example, the states associated with the first row of the probability matrix can only be reached in one transition from states associated with an f transition, that is, either bf (second row) or ff, and the state bb (fourth row) can only be reached in one transition from states associated with a b transition, that is from either fb or bb (third or fourth rows respectively). For this reason some entries of the probability matrix in equation 3.4 are forced to zero.

It is important to point out that a lower order Markov process can be modeled by a higher order Markov process simply by constraining the probabilities in the higher order Markov process. For example, the transition probability matrix for the second order Markov process outlined in equation 3.3 can be used to model the first order Markov process outlined in equation 3.2 by imposing the constraint that $\alpha_{ff} = \alpha_{bf}$, while the first, second, or third order Markov processes outlined in equations 3.2, 3.3, and 3.4, respectively, can each be used to model the zeroth order Markov process outlined in equation 3.1 by imposing

the constraints that $\alpha_f = \alpha_b = 0.5$, $\alpha_{ff} = \alpha_{bf} = 0.5$, or $\alpha_{fff} = \alpha_{bff} = \alpha_{fbf} = \alpha_{bbf} = 0.5$, respectively.

In all these above cases the probability distributions describing the likelihood of repeated sequential transitions are generally geometric in nature, however it is important to remember that the layer sequences are finite in length, as they represent small domains. This can affect the probability distribution shape.

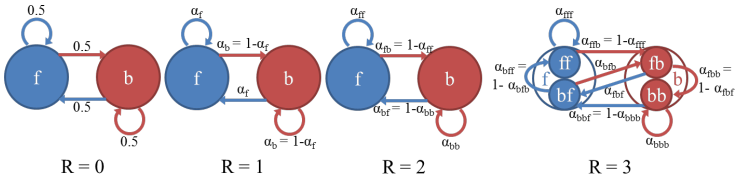

Figure 3.1: Finite state machines representing the Markov process for the case of close packed nickel for different interaction ranges R. Forward transitions are associated with a blue color, while b transitions are associated with a red color.

As a final note the symmetry of these polytypes should be considered: a series of f transitions is equivalent to a series of b transitions in an inverted coordinate system. By Friedel's law, the scattering behavior of the two objects are however equivalent. Thus, in all of the above cases, it is possible to completely swap the probabilities of f and b transitions to obtain an equivalent physical system.

For example, taking equation 3.2 and assigning explicit probabilities gives the matrix

$$\mathbf{P} = \begin{bmatrix} \alpha_f = 0.2 & \alpha_b = 1 - 0.2 = 0.8 \\ \alpha_f = 0.2 & \alpha_b = 1 - 0.2 = 0.8 \end{bmatrix}. \tag{3.5}$$

However, the probability matrix

$$\mathbf{P} = \begin{bmatrix} \alpha_f = 0.8 & \alpha_b = 1 - 0.8 = 0.2 \\ \alpha_f = 0.8 & \alpha_b = 1 - 0.8 = 0.2 \end{bmatrix} \tag{3.6}$$

leads to an ensemble of stacking sequences that are, on average, equivalent. This implies that only a portion of the parameter space associated with the Markov transition probabilities leads to unique systems, at least in the case of nickel.

3.1.2 Automated stochastic domain creation

Once all characteristics of the virtual powder specimen have been chosen, the specimen can be synthesized. The DISCUS software package (v3.6.2), written by Proffen and Neder, is ideal for this purpose [130]. DISCUS is a flexible application for building and manipulating domains. The software contains intrinsic functionality for stochastically sampling various statistical distributions, assembling layers using a Markov process, and cutting crystals based on a shape function. An example DISCUS script that could be used to synthesize a virtual powder sample is provided in Appendix A. The script implements an $R = 3$ stacking scheme, and thus can be used to model all $R \leq 3$ schemes.

In summary, the user provides the script with the intended log-normal mean μ and standard deviation σ for a log-normal distribution describing the domain diameters, along with a unit cell for each layer type (here each layer has an identical unit cell), and transition probabilities. DISCUS randomly samples the log-normal distribution to obtain a domain diameter and creates an atomic layer that is wider than the intended CSD. Following this, DISCUS creates a stacking sequence by randomly sampling the user defined Markov process. The stacking sequence has enough layers to be larger than the domain diameter. DISCUS then populates the stacking sequence with the atomic layers. The entire stack is then shifted by a randomly generated vector, modulo the layer unit cell, to ensure that the lattice and shape function origin are not coincident. Lastly, the spherical shape function is applied, removing all atoms outside its boundaries.

By following this process, DISCUS was used to create seven different virtual powder specimens, with properties outlined in Table 3.1. The libraries all contained at least 2,000 individual domains to ensure adequate sampling of the underlying statistical processes.

Select atomistic domains, chosen from the libraries built with the DISCUS software, can be rendered using OVITO (Open Visualization Tool) [131]. OVITO is a powerful tool, not only for rendering atomistic models, but also for post-processing these atomistic models. Among other things, OVITO can quickly perform common neighbor analysis, identifying the local polytype symmetry of atoms, and color the atoms accordingly. OVITO is capable of differentiating between not only the fcc and hcp polytypes, but also the two common polytypes of

Sample	e^{μ} (nm)	σ	Reichweite R	Probability	
1	5	0	0	-	-
2	5	0.1	0	-	-
3	5	0.1	1	$\alpha_f = 1.0$	-
4	5	0.1	2	$\alpha_{ff} = 0.8$	$\alpha_{bb} = 0.2$
5	15	0.1	0	-	-
6	15	0.1	2	$\alpha_{ff} = 0.8$	$\alpha_{bb} = 0.2$
7	15	0.1	1	$\alpha_f = 1.0$	-

Table 3.1: Characteristics of virtual powders synthesized here. e^{μ} is the median of the log-normal distribution described by log-normal mean and standard deviation μ and σ, respectively.

sp^3-bonded carbon, namely diamond and lonsdaleite. Within all the atomistic models rendered here, this common neighbor analysis has been performed using OVITO, and green or red atoms are coordinated locally as fcc or hcp, respectively. Under-coordinated surface atoms have been removed to improve visibility.

Four randomly selected domains from sample 1 are shown in Figure 3.3, with stacking disorder highlighted by common neighbor analysis. This sample is monodispersed, with domains that are only 5 nm across. It is characterized by an $R = 0$ stacking scheme, and thus it is governed by the transition probability matrix as outlined in equation 3.1. Within sample 1, domains contain both twin boundaries and deformation faults (hcp bands that are 1 or 2 atoms thick, respectively), but also seen are hcp bands significantly thicker than 2 atomic layers.

It is interesting to note that, although each domain in Figure 3.3 was carved with the same 5 nm spherical shape function, the random shift imposes a unique surface termination on each domain. The configuration space associated with this sample is then a result of both the layer configurations and surface termination of the domains.

Sample 2 is identical to sample 1, with the exception that the diameters of the domains in the former are not monodisperse, but rather are described by the log-normal distribution in Figure 3.2, with a median domain diameter of 5 nm, log-normal standard deviation of 0.1, and about 95% of the domains between 4 and 6 nm in diameter. The configuration space in this sample is a result of the same linear disorder

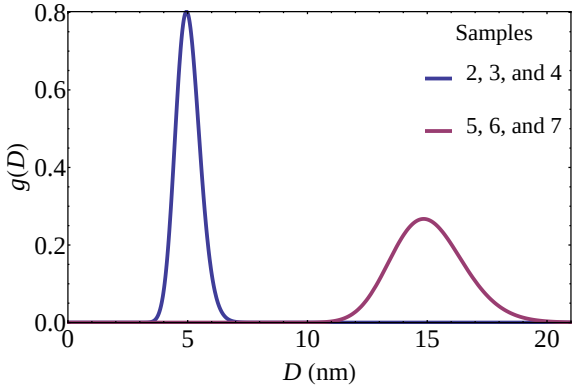

Figure 3.2: Probability density $g(D)$ functions describing the distributions of domain diameters D for the different (labeled) virtual specimens outlined here. Both distributions are log-normal, with a median of either 5 or 15 nm, and a log-normal standard deviation of 0.1.

and surface termination as sample 1, with an added configuration dimension of domain diameter dispersion. All these features can be can be seen in Figure 3.4, which shows four randomly selected domains from this sample.

Sample 3 is an example of an "unfaulted" powder. Within the Markov framework outlined here this deterministic stacking can be described by an $R = 1$ stacking scheme as described by the general probability matrix in equation 3.2, with the probability of an f transition set to 1 leading to an ordered fcc structure. The domains in the sample are characterized by a median diameter of 5 nm, with a diameter dispersion identical to that in sample 2, shown in Figure 3.2. The configuration space in this sample does not include the effect of linear disorder, only that of domain diameter dispersion and surface termination. Four randomly selected domains from sample 3 are shown in Figure 3.5, where it can be seen that the stacking scheme clearly leads to ordered, entirely fcc domains.

Sample 4 is characterized by an $R = 2$ stacking process, with a 80% chance of an f transition given a preceding f transition and a 20% chance of a b transition given a preceding b transition, according to the

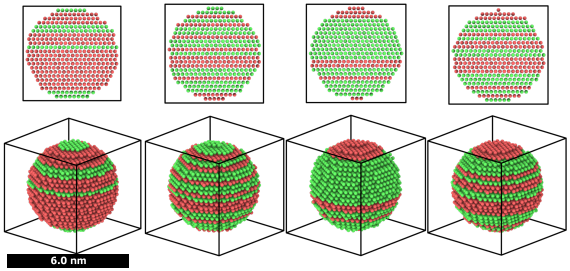

Figure 3.3: Four domains selected randomly from sample 1, shown in both a front view (top) and orthographic projection (bottom). All domains show an identical diameter, but different stacking sequences described by the associated Markov process.

probability matrix shown in equation 3.3. Sample 4 shows the same domain diameter dispersion of samples 2 and 3 (Figure 3.2), with a median diameter of 5 nm. It is clear by viewing a few of the domains, presented in Figure 3.6, that the stacking disorder in this sample is much less "severe" than in the $R = 0$ case of either sample 1 or 2. Significantly fewer and thinner bands showing a local hcp structure are seen. Twin boundaries and deformation faults are however both still present, as are hcp bands greater than two atomic layers.

It is however not immediately obvious how changing from an $R = 0$ to an $R = 2$ stacking disorder alters the configuration space of the sample. Strictly speaking this change affects only the *probability* of each configuration within a domain of a certain diameter: within the $R = 0$ model, all stacking configurations have an equal probability, whereas in an $R = 2$ model, this is not necessarily true. The *total number* of possible configurations is unaltered by changing the stacking model, as this number is only dependent on the diameter of the crystal.

Sample 5 signals a departure from the domain diameter distribution common to samples 2, 3 and 4. The domains diameters in sample 5 are described by the distribution in Figure 3.2, with a median domain diameter of 15 nm, and about 95% of the domains between 12 and 18 nm in diameter. Sample 5 is characterized by the same $R = 0$ stacking

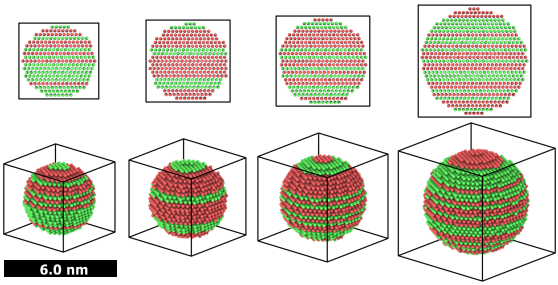

Figure 3.4: Front views (top) and orthographic projections (bottom) of four domains selected randomly from sample 2. Domains show a diameter distribution as presented in Figure 3.2 and different stacking sequences.

process describing sample 2, with a probability matrix as outlined in equation 3.1. Figure 3.7 shows four randomly selected atomistic domains from this sample, showing the diameter dispersion and stacking disorder clearly.

The domains in sample 6, rendered in Figure 3.8, show the same diameter dispersion as sample 5, with a mean diameter of 15 nm. The layer stacking is governed by the same $R = 2$ stacking disorder as sample 4, with an 80% chance of an f transition given a preceding f transition and a 20% chance of a b transition given a preceding b transition (equation 3.3).

Sample 7 (Figure 3.9) is again an example of an "unfaulted" powder, similar to sample 3, with a unity probability of an f transition between any two layers. This sample shows the same larger average domain diameters as samples 5 and 6, with Figure 3.2 showing the diameter dispersion.

3.2 Synthesized (simulated) powder diffraction data

3.2.1 The Debye scattering equation

Once a substantial quantity of domains (typically greater than 2,000) have been created for a given virtual powder, the atomic coordinates can be be used to compute "synthetic" powder diffraction data of the

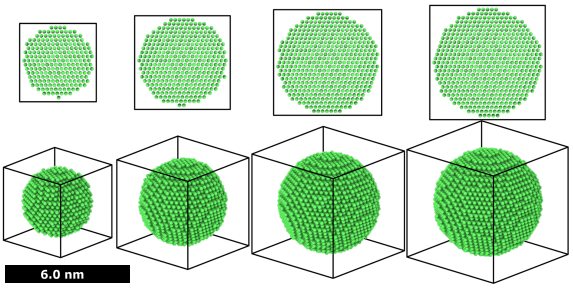

Figure 3.5: Four domains randomly chosen from sample 3, presented in front views (top) and orthographic projections (bottom). Domains show a diameter distribution as depicted in Figure 3.2, with a median diameter of 5 nm. The domains are completely "unfaulted," each showing a deterministic stacking sequence, leading to an fcc structure

object through a DS approach, using the Debye scattering equation (DSE), which is provided here without derivation as

$$I(s) = \sum_{i=1}^{N_{atoms}} \sum_{j=1}^{N_{atoms}} f_i(s) f_j^*(s) \operatorname{sinc}(2\pi s r_{ij}), \tag{3.7}$$

where the double sum is over all atoms in the domain and r_{ij} is the distance between the i and j atomic pair. A deterministic approach, the DSE as presented in equation 3.7 yields the far-field, dynamical, diffracted intensity distribution for an atomistic object averaged over all possible rotations [132]. If the ensemble is a collection of diverse rather than identical objects, the diffracted intensity distribution of the ensemble can be computed as incoherent arithmetic average of the diffracted intensity distribution from each object, provided that each object in the ensemble is sufficiently mis-oriented to scatter independently [52].

The DSE as presented in equation 3.7 is often considered the most precise, accurate, and flexible method for modeling powder diffraction from nanocrystalline systems. Contrary to the RS models outlined in Chapter 2, equation 3.7 forces no assumptions regarding the characteristics of the unit cells, periodicity, crystallinity or morphology of the coherently scattering objects. No approximations, aside from that of

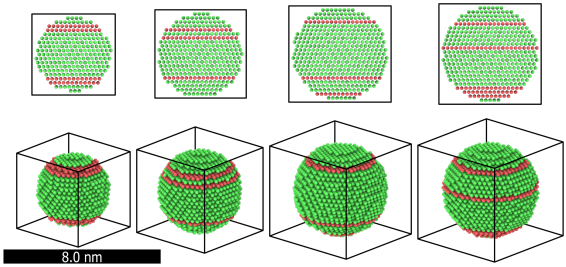

Figure 3.6: Front views (top) and orthographic projections (bottom) of four domains selected randomly from sample 4. Domains show a diameter distribution as depicted in Figure 3.2 and stacking sequences that are the result of an $R = 2$ stacking process with $\alpha_{ff} = 0.8$ and $\alpha_{bb} = 0.2$ (equation 3.3). This particular stacking scheme leads to bands showing a local hcp structure which are much thinner and less numerous than those observed in either sample 1 or 2.

an "ideal powder," are invoked for powder integration, and any type or degree of correlation between structural, nanostructural or microstructural parameters can be treated generally, since each scattering object must be defined explicitly.

Unfortunately, the high level of precision, accuracy, and flexibility is associated with relatively high computational costs. If the ensemble of interest is described by broad statistical distributions governing properties such as size, morphology, or stacking disorder type/extent, then the intersection of all configuration spaces implies that the total number of possible atomic configurations can be extremely large. The explicit nature of the DSE necessitates that a similarly large number of individual objects be considered. Further, the necessary computation time for the DSE scales with the sixth power of the linear dimension of the domain, implying additional computational overheads if the average size of the domains is large, or the size distribution is skewed towards large sizes.

While considerable progress has been made to speed up DSE computations [39, 133, 134] the combined effects of large configuration spaces and non-linear scaling of computation time necessitate that DSE approaches are best suited for systems of relatively small domains with

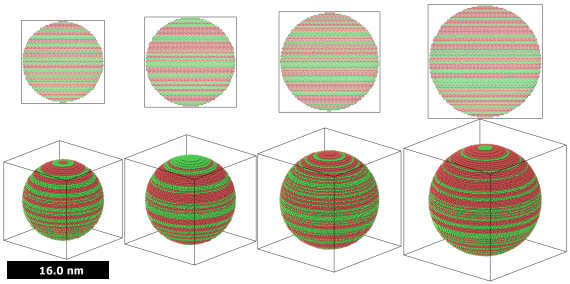

Figure 3.7: Four domains selected randomly from sample 4, characterized by a median diameter of 15 nm and the same $R = 0$ stacking process as in samples 1 and 2, leading to an equal chance of bands showing either an hcp or an fcc structure.

tightly controlled characteristics. For these reasons, studies employing the DSE to deduce real atomic, nano, and microstructural information from experimental data can be found [135–137] but are not yet common.

3.2.2 Convergence

For a polydisperse powder sample showing stacking disorder, it may be likely that no single domain can be considered representative of the whole sample; each is only one of many possible atomic configurations, chosen from the whole configuration space of the sample, and each in turn shows a unique diffracted intensity distribution. As an example, three very diverse intensity distributions are plotted in Figure 3.10. Each is computed by feeding the atomic coordinates of three different domains, shown inset in Figure 3.10, into the DSE (equation 3.7). Each domain was selected randomly from from sample 6, and is thus governed by the statistics of that sample, but none represents the ensemble-average diffracted intensity, shown in Figure 3.17.

In practice, a true nanocrystalline sample is composed of millions or more individual domains, quite an impractical number to consider using the DSE. If an ensemble-averaged powder intensity distribution is sought, it must naturally then be approximated, and it becomes important to check the accuracy of this approximation with respect

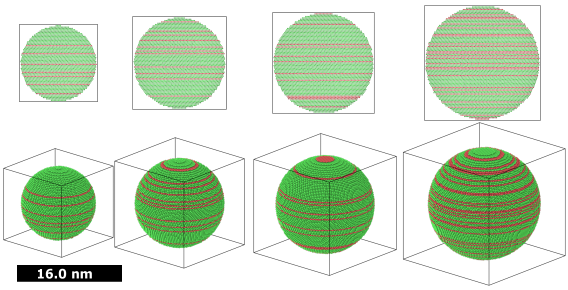

Figure 3.8: Front views (top) and orthographic projections (bottom) of four domains selected randomly from sample 6. Domains show the same diameter distribution as sample 5, shown in Figure 3.2, with various $R = 2$ stacking sequences, where $\alpha_{ff} = 0.8$ and $\alpha_{bb} = 0.2$ (equation 3.3).

to the number of domains considered, in order to ensure convergence of the finite-average approximation to the "true" ensemble-averaged intensity distribution. Beyond this, by determining a minimum number of necessary domains, the "information content" of the diffraction data can be checked as a function of the physical characteristics (atomic, nano, and microstructural) of the sample.

To this end, it is useful to look towards the relatively new approach of "serial femtosecond crystallography," where pulsed X-ray free electron lasers are used to serially collect partial diffraction datasets from a series of individual objects (often individual domains) [138]. These partial datasets are then merged to build the ensemble-averaged diffraction dataset. Naturally, this data merging suffers from a problem similar to the one just mentioned: a sufficient number of partial datasets must be considered to provide an averaged diffracted intensity distribution which is representative of the sample.

Researchers in this field use a measure they call R_{split} to ensure that the dataset is converged [139]. It is the total fractional (or percent) difference between two ensemble-averaged datasets, where the population considered in each ensemble-average is equal in total size, but composed of different randomly selected partial datasets. It can be written as

$$R_{split} = \frac{100}{\sqrt{2}} \frac{\sum I_{\text{group 1}} - I_{\text{group 2}}}{\frac{1}{2}\sum I_{\text{group 1}} + I_{\text{group 2}}}, \tag{3.8}$$

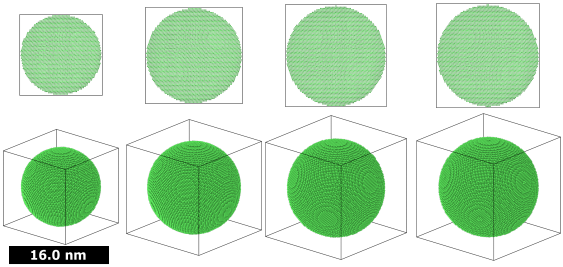

Figure 3.9: Four domains randomly chosen from sample 7, presented in front views (top) and orthographic projections (bottom). Domains show a diameter distribution as depicted in Figure 3.2, with a median size of 15 nm. The domains are completely "unfaulted," each showing a deterministic stacking sequence, leading to an fcc structure

where the summation is over all data points in the data set, and $I_{\text{group 1}}$ and $I_{\text{group 2}}$ represent the averaged intensity by merging over the two different randomly selected datasets.

For each virtual powder sample outlined in Section 3.1.2, R_{split} was computed as a function of the ensemble population size in the scattering vector range from 0.3 Å^{-1} to 1.9 Å^{-1}, representing the wide-angle X-ray scattering (WAXS) of the virtual powder data. Small-angle X-ray scattering (SAXS) was not considered here. To smooth fluctuations associated with the random sampling, an average R_{split} value of 10 different random selections was taken at each populations size. The R_{split} data for each sample was then fit with the function

$$R_{split}(x) = \frac{a}{x^k}, \tag{3.9}$$

where x is the population size, or the number of randomly selected domains included in the ensemble-average, and a and k are fitting parameters. Instrumental weighting was used in the fit, with the standard deviation at each population size being estimated from the averaging over 10 different random selections. The fitted curves for each sample are plotted in Figure 3.11, while Table 3.2 shows the fitted values for a and k, along with the minimum number of randomly selected domains necessary to achieve $R_{split} = 5\%$ and $R_{split} = 1\%$.

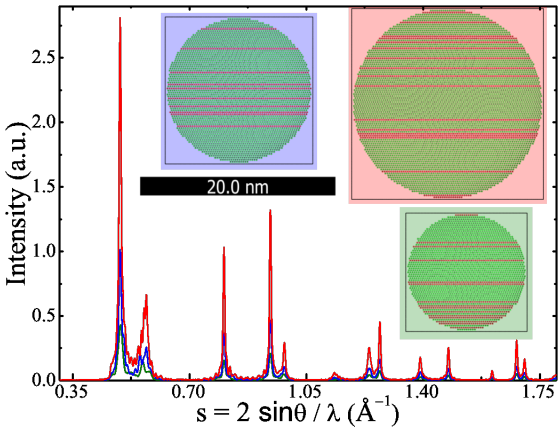

Figure 3.10: The intensity distributions, computed using the DSE (equation 3.7), associated with three different domains, shown inset, randomly selected from sample 6. The colors highlighting each atomistic domain correspond to the associated intensity distribution in the plot.

In general, the convergence behavior is much more rapid than what is seen in serial femtosecond crystallography [139], where thousands or hundreds of thousands of datasets can be necessary to achieve convergence to $R_{split} = 5\%$. This is not at all surprising, as each population member in serial crystallography experiments yields only a small section of RS, whereas in this study each population member provides an entire orientation-averaged picture of RS, leading to much faster convergence.

Of all the samples considered here, sample 1 shows the fastest convergence rate, dropping to $R_{split} = 1\%$ after considering only 177 domains. The ensemble-averaged powder diffraction data for $R_{split} = 5\%$ and $R_{split} = 1\%$ is shown in Figure 3.12, along with the residual between the two convergence levels. The residual is generally spread over the entire dataset, but is largest at Bragg peaks.

This relative result is not surprising; sample 1 is the only monodisperse sample explored here, and the lack of domain size dispersion naturally leads to a narrower configuration space and more rapid convergence. The overall implications are however quite interesting, as a 5

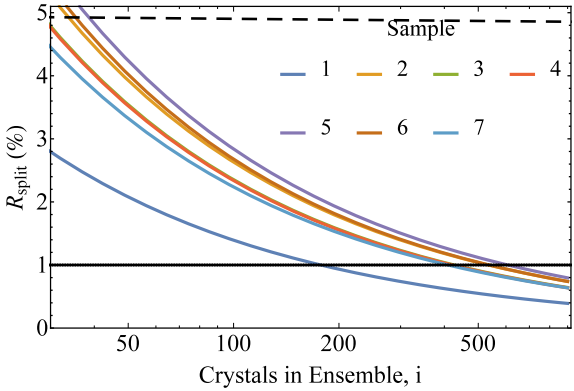

Figure 3.11: Fitted functions (equation 3.9 and Table 3.2) for computed R_{split} (equation 3.8) values considering only WAXS as a function of the number of domains considered in the average, for the 7 different virtual powders considered here. A dashed and solid line is drawn for $R_{split} = 5\%$ and $R_{split} = 1\%$, respectively.

nm domain of this type contains about 25 atomic scale layers, leading to 2^{25} (more than 33 million) possible layer permutations. Granted, at least half of of these permutations are identical by symmetry, but the added possibilities in terms of surface termination further increase the configuration space. Despite what seems like a huge number of possible unique configurations, it is clear that the average diffracted intensity of the sample can be represented to a total error (R_{split}) of less than 1% by considering *as few as 177* configurations or domains. This is a rather striking result, as a typical diffraction dataset from a nanocrsytalline powder sample represents the average of *millions* of domains.

Comparing sample 2 and sample 1 can help isolate the convergence effects of size dispersion, as the two samples show the same type and amount of stacking disorder and the same median domain diameter, but sample 2 includes size dispersion. This feature significantly slows the convergence behavior of the ensemble-average diffraction dataset, shown in Figure 3.13; in this case more than 530 domains must be considered in order to achieve convergence to $R_{split} = 1\%$, more than

Sample	a	k	$R_{split} < 5\%$ (number of domains)	$R_{split} < 1\%$ (number of domains)
1	20(1)	0.580(2)	11	177
2	38(1)	0.577(5)	33	534
3	36(1)	0.590(5)	28	426
4	36(2)	0.591(8)	28	421
5	41(1)	0.578(5)	38	607
6	40(1)	0.586(7)	34	537
7	31(1)	0.571(5)	24	409

Table 3.2: Fitted parameters with estimated standard uncertainties, based on fitting equation 3.9 to data generating by applying equation 3.8. Also listed are the minimum number of domains necessary to achieve different levels of convergence of the ensemble-averaged diffracted intensity, computed using the DSE (equation 3.7)

3 times what was necessary in the case of sample 1. The trend of this result is to be expected; including size dispersion naturally expands the configuration space. It is interesting to note the rather large impact on convergence behavior that occurs by including a rather small amount of dispersion in the domain size distribution, as 95% of the domains are within just ± 1 nm of the median size of 5 nm. In fact, no other single effect investigated here causes such slowing of the convergence behavior, in terms of the relative number of domains necessary.

Comparing the convergence behavior of sample 2 to that of sample 3 can serve to isolate the effect of $R = 0$ type stacking disorder on convergence: the two samples show an identical domain size distribution, but sample 3 shows no stacking disorder, or an *entirely* fcc structure. The powder diffraction dataset from sample 3, shown in Figure 3.14, converges to $R_{split} = 1\%$ after considering 426 domains, 108 fewer domains than were necessary to reach convergence in the case of the $R = 0$ sample, indicating that the convergence effect of $R = 0$ type stacking disorder is small. Much greater is the effect of size dispersion, seen by contrasting convergence behavior of sample 1 with 2.

The residual between the datasets converged to either $R_{split} = 5\%$ or $R_{split} = 1\%$, in the case of sample 3 (Figure 3.14), shows a different behavior than that seen in either samples 1 or 2. Rather than

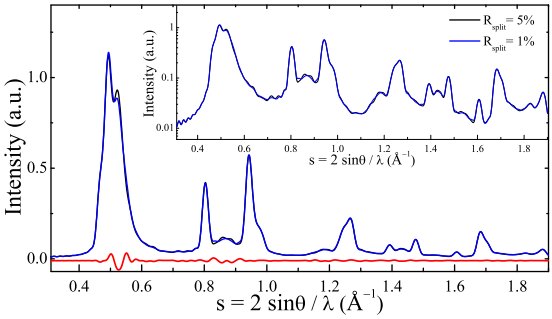

Figure 3.12: The approximated ensemble-averaged powder diffraction data of sample 1, on both a linear and log (inset) scale, computed by averaging the output of the DSE. The two curves represent the approximate averages after considering either 11 or 177 domains, leading to a respective convergence level of $R_{split} = 5\%$ or $R_{split} = 1\%$. The residual between the two levels of convergence is also shown offset.

being spread evenly across the entire scattering vector range, it is concentrated heavily at Bragg peaks. This is reasonable, as the ordered stacking implies no real diffuse intensity between Bragg peaks. Rather, all intensity in the dataset from each domain is concentrated around Bragg peaks.

To investigate the convergence effect of the *type* of stacking disorder, sample 4 can be compared to sample 2. The two are identical except that the former is characterized by an $R = 2$ type stacking process, while the latter is characterized by an $R = 0$ type stacking process. Only about 421 domains are necessary to achieve convergence to $R_{split} = 1\%$ in the case of sample 4, shown in Figure 3.15. This is about 113 fewer than that necessary in the case of sample 2. Thus it would appear that the more complex $R = 2$ type disorder increases the convergence rate and shrinks the configuration space of the ensemble. Conversely, there is not a significant difference between the convergence behavior of sample 4, showing a $R = 2$ type disorder and sample 3, showing no stacking disorder.

Samples 5, 6, and 7 show a median domain size of 15 nm, but show stacking disorder that is identical to samples 2, 4, and 3, respectively.

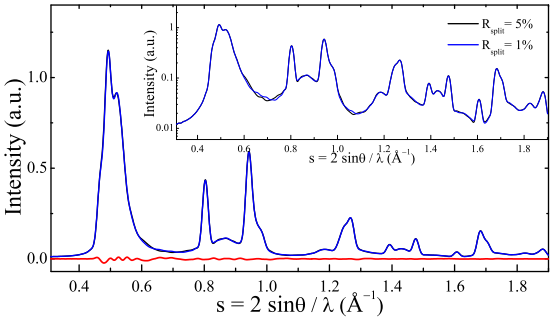

Figure 3.13: Approximate ensemble-averaged powder diffraction data from sample 2, shown on both on a linear and log (inset) scale. The two curves represent either an $R_{split} = 5\%$ or $R_{split} = 1\%$ level of convergence, computed by averaging the output of the DSE from either 33 or 534 domains respectively. A offset residual between the two levels of convergence is also shown.

Comparing the two sets can then give the effect on convergence behavior of increasing the median domain size, holding other factors constant. To achieve convergence to $R_{split} = 1\%$ for the diffraction data from sample 5, shown in Figure 3.16, an average of 607 domains needed to be considered, only 73 more than were necessary for sample 2. A similar trend is found when comparing samples 6 and 4, which both show a more complex, $R = 2$ type, stacking process; moving to the larger median domain size as seen in sample 6 entails considering about 116 more domains to achieve convergence of the ensemble-averaged diffraction dataset, shown in Figure 3.17, to $R_{split} = 1\%$.

This relatively small number of additional domains required to achieve convergence in samples 5 and 6 when compared to samples 2 and 4, is rather unexpected. Tripling the median domain size entails increasing the number of possible layer configurations in a stacked domain by a factor of 9, as N total layers and 2 layer types gives 2^N possible stacking permutations. This significant increase in the configuration space however does not appear to impact convergence behavior of the diffraction data significantly.

It is worth pointing out that, even if an increase in median domain

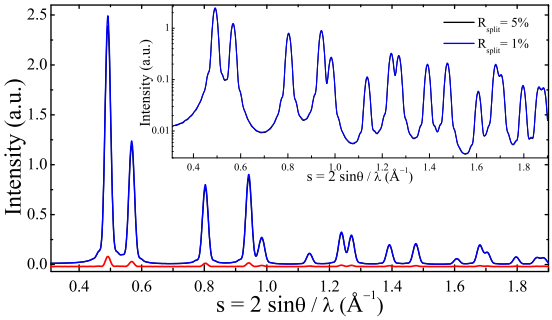

Figure 3.14: Different convergence levels ($R_{split} = 5\%$ or $R_{split} = 1\%$) of the approximate ensemble-averaged powder diffraction data from sample 3, computed using either 28 or 426 domains, respectively. The residual between the two levels of convergence is also shown offset, and a log-scale plot is shown inset to highlight small differences in diffuse features.

linear dimension does not dictate a significant increase in the *total number* of domains necessary to achieve convergence, a threefold increase in the median domain linear dimension dictates a $3^6 = 729$-fold increase in *computation time* when using the DSE (equation 3.7) to compute the ensemble average.

Comparing the convergence behavior of the samples 7 and 3, where no stacking disorder is present, it can be seen that increasing the median domain size leads to a slight *decrease* in the number of domains necessary to achieve convergence to $R_{split} = 1\%$. This represents an inversion of the trend seen when comparing samples 5 and 2 or samples 6 and 4.

Such an inversion may initially seem surprising, but has an intuitive explanation if the ensemble averaged powder intensity distribution of sample 7, shown in Figure 3.18, is considered in the context of the nature of the sample. The increase in median domain size necessitates a *decrease* in the FWHM of the Bragg peaks, and the regular stacking present in the sample dictates that significant diffuse scattering is not present. Thus, the diffracted intensity is concentrated into a smaller scattering vector range, giving a decreased possibility of fluctuations between individual intensity distributions. This is further evidenced in

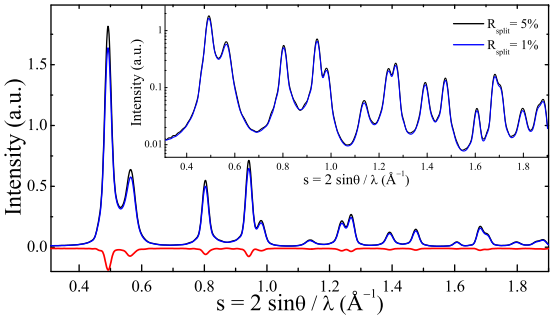

Figure 3.15: The approximate powder ensemble averaged powder diffraction data from sample 4, on both a linear and log (inset) scale. The two curves represent the average powder diffraction data after averaging the output of the DSE considering either 28 or 421 domains, leading to a respective convergence level of $R_{split} = 5\%$ or $R_{split} = 1\%$. The residual between the two levels of convergence is also shown.

the residual resulting from sample 7, shown in Figure 3.18.

Summarizing, this study suggests that domain size dispersion has a much greater impact on the convergence behavior than the type of stacking disorder, or even the median domain size, at least in terms of the *number* of domains necessary to achieve an ensemble-averaged powder diffraction dataset. Increasing the median domain size from 5 to 15 nm has only a marginal impact on the convergence behavior. The slowest convergence behavior was seen in the highly disordered $R = 0$ samples showing domain size dispersion. Importantly, all samples considered here show an average R_{split} value of less than 1% after considering at most 610 domains in the ensemble-average. This suggests that for the material, morphology and stacking disorder types considered here, libraries of just 610 domains can be considered representative when simulating powder diffraction data using the DSE (equation 3.7).

This is however *not equivalent* to declaring these libraries representative in other situations. It is entirely possible that these libraries do not fully embody the statistics of the sample in terms of other physical characteristic, such as layer-configuration, size distribution, or surface

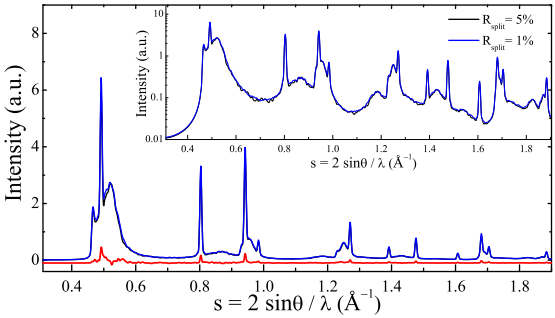

Figure 3.16: Different convergence levels (R_{split} = 5% or R_{split} = 1%) of the approximate ensemble-averaged powder diffraction data from sample 5, computed using either 38 or 607 domains, respectively. The residual between the two levels of convergence is also shown offset, and a log-scale plot is shown inset to highlight small differences in diffuse features.

termination. It is also likely that such small libraries are not representative of macroscopic properties.

As a specific example, sample 1 can be considered. It was mentioned that the total number of possible layer permutations in a 5 nm spherical nickel domain showing stacking disorder is more than 33 million. In the $R = 0$ case of sample 1, each of the layer configurations has an *equal* probability, since the likelihood of an f or b transition is equal. Yet, in the case of sample 1, only 177 randomly selected configurations are necessary to represent the ensemble-averaged powder diffraction dataset to R_{split} = 1%. This essentially means that diffraction techniques cannot unambiguously determine the difference between two samples, one governed by the statistics of sample 1 as outlined in Table 3.1, and one composed of only 177 different configurations selected from sample 1.

This is an important point, and it should be highlighted, as it represents a fundamental limitation of diffraction based characterization. While the powder diffraction data of the two above mentioned samples may be indistinguishable, it is not guaranteed that any other observable macroscopic properties of the two samples are identical.

In the following section, the powder diffraction data from each of the

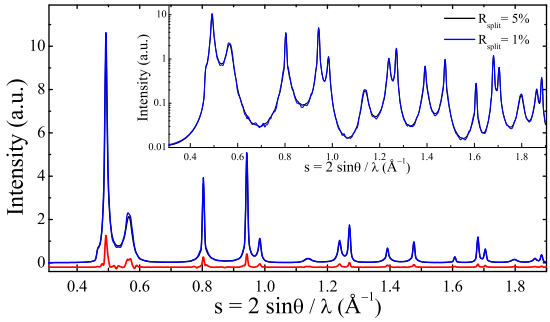

Figure 3.17: The approximate averaged powder diffraction data from sample 6, on both a linear and log (inset) scale. The two curves represent the average after averaging the output of the DSE considering either 34 or 537 domains, leading to a respective convergence level of $R_{split} = 5\%$ or $R_{split} = 1\%$. The residual between the two levels of convergence is also shown.

7 virtual powder samples is discussed and analyzed using different RS based approaches, including traditional line-profile analysis techniques and the new models proposed in Chapter 2. By comparing the fit quality and predicted ensemble parameters of different RS approaches, the overall accuracy of each can be tested.

3.3 Characterization using RS approaches

By establishing a novel convergence criteria, borrowed from the community of serial crystallography, the minimum number of domains necessary to reach reasonable and uniform convergence was established and compared for each virtual powder. Having established uniform convergence, it is possible to use these synthetic datasets to assess the accuracy and validity of different RS modeling approaches as proposed in Chapter 2.

In Section 3.3.1, traditional LPA techniques, based on the equations of Section 2.4.3, are employed to fit the synthetic diffraction data where possible. The results of the analysis are reported, and compared to the known properties of the virtual powder.

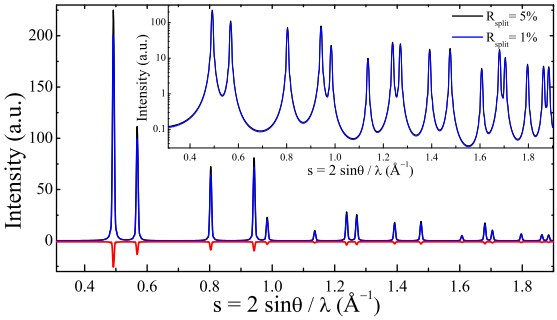

Figure 3.18: The approximated ensemble-averaged powder diffraction data of sample 7, on both a linear and log (inset) scale, computed by averaging the output of the DSE. The two curves represent the approximate averages after considering either 24 or 409 domains, leading to a respective convergence level of $R_{split} = 5\%$ or $R_{split} = 1\%$. The residual between the two levels of convergence is also shown offset.

In Section 3.3.2, more advanced RS modeling techniques, based on the equations of Section 2.6.3, are used to directly fit the synthetic data. These results are reported, and compared to both the known properties of the virtual powder, and the results obtained in Section 3.3.1.

3.3.1 Traditional LPA: fitting with empirical profile functions

As pointed out briefly in Sections 1.2 and 2.4.3, traditional techniques are typically based on the application of equation 2.23 to compute line-profiles positions and relative intensities, followed by an assumption that the line-profiles shape can be modeled by an empirical profile function. This effectively amounts to assuming a powder pattern of the form arising from perfect, spatially infinite crystals that is empirically broadened, as per equation 2.24.

A commonly adopted empirical profile is the pseudo-Voigt, a linear combination of a Cauchy (or Lorentz) and Gauss (or normal) distribution. The pseudo-Voigt profile is a computationally simpler alternative to the true Voigt profile, which represents a convolution of a Cauchy

and Gauss distribution, and can be written as

$$pV\left(x, x_0, I, \eta, \Gamma\right) = I\left[\eta\left(\frac{1}{\pi}\frac{1/2\Gamma}{(x-x_0)^2+(1/2\Gamma)^2}\right) + (1-\eta)\left(\frac{1}{\Gamma}\sqrt{\frac{\ln 16}{\pi}}e^{-\frac{4(x-x_0)^2\ln 2}{\Gamma^2}}\right)\right] \tag{3.10}$$

where the two terms inside the brackets are the Cauchy and Gauss distributions respectively.

The pseudo-Voigt profile is parametrized by the total integrated intensity $I = \int pV\left(x, x_0, I, \eta, \Gamma\right)\,\mathrm{d}x$, the location of the profile x_0, the FWHM Γ, and η, the fraction of Cauchy character of the profile.

There a number of ways to constrain these parameters. If equation 2.24 is used, Bragg's law constrains the position x_o of each line-profile, and the number of free parameters depends on the assumed lattice symmetry, with a maximum of 6 for the lowest symmetry lattices. If information on the atomic coordinates within the unit cell is desired, then the structure factor can be used to compute integrated intensity of each profile, I. The asymmetric unit then determines the number of free parameters, with a maximum 5 times the number of atoms in the asymmetric unit, if occupancy and isotropic thermal displacement are considered. There are a number of methods to constrain the peak shape parameters η and Γ, but in the simplest case they are often left free, leading to an additional number of fitting parameters equal to 2 times the number of non-degenerate line-profiles.

An alternative to this approach is to leave all profile parameters free within the fitting routine, leading to a quantity of fitting parameters equal to 4 times the number of non-degenerate line-profiles. Such model freedom often can lead to a better fit in terms of quality indices when compared to more constrained models. Assigning physical meaning to these unconstrained refined values is not always straightforward, however, and thus it can be difficult to make good use of this information.

The two above modeling approaches represent extremes of diffraction data fitting: highly constrained vs. unconstrained fitting. There exist numerous permutations of the two approaches, with different degrees of constraints. Each permutation has its own advantages and disad-

vantages, and finds use in specific situations depending on the type of information desired.

This discussion neglects the contribution of the diffraction instrument to the line profile shape. The datasets considered here are synthetic, computed using the DSE, and thus are not affected by the instrument. Proper handling of the instrumental effect is however an important part of application of these techniques to real diffraction datasets, and is discussed briefly in Chapter 4.

Within traditional LPA, the results of the data fitting are often interpreted using what is typically called a Williamson-Hall plot [18], where the ratio of the line-profile area to its height, or the integral breadth β, is plotted as a function of the scattering vector s. The trend in $\beta(s)$ gives some indication of the source of the line-profile broadening. Under the common and so-called "size-strain" model, it is assumed that

$$\beta(s) = \frac{1}{\langle L \rangle_V} + 2\langle \varepsilon \rangle s, \tag{3.11}$$

where $\langle L \rangle_V$ is the isotropic volume-weighted mean column length (MCL), and $\langle \varepsilon \rangle$ is the mean isotropic microstrain within the lattice. Thus, by fitting a line to the $\beta(s)$ data as extracted from the fitted empirical profiles, the $\langle L \rangle_V$ and $\langle \varepsilon \rangle$ can be estimated for a sample. Several modified techniques exist for this approach [140, 141], where an attempt is made to handle anisotropic volume-weighted MCLs and strains. For the virtual powders outlined here only the simple isotropic model embodied in equation 3.11 will be employed, as it is known *a priori* that no strain is present, and that the domain morphology is isotropic.

By adopting this traditional LPA approach, some of the powder diffraction datasets presented in Section 3.2 can be fit. It is clear from reading Section 2.4 that Bragg's law and the structure factor of the unit cell, arising from equation 2.24, are intrinsically based on the assumption of perfect, spatially infinite crystals, an assumption that is plainly not true in the case of any of the virtual powder samples (or any real sample, for that matter). That being said, it is useful to attempt such an analysis to understand the exact nature of the shortcomings of these assumptions.

In all the fits presented in this section, the powder diffraction data was fit over the range $0.3 < \mathbf{s} < 1.9\text{Å}^{-1}$ by minimizing the unweighted

sum of the squared differences within the fityk v0.9.8 software package [142]. A pseudo-Voigt line-profile shape as described by equation 3.10 was assumed for each of the 14 distinct line profiles in this scattering vector range. In each virtual powder, an initial fit was attempted where the profile center x_0 and integrated area I were both constrained by equation 2.24 assuming the nickel structure outlined in Section 2.1.

The cubic lattice parameter, a_c, was allowed to vary freely. The position and occupancy of the single nickel atom in the asymmetric unit were held fixed at (0,0,0) and 1.0, respectively, while an isotropic Debye-Waller factor $\langle u^2 \rangle$, representing the mean squared atomic displacement, was allowed to vary freely for this atom. The shape parameters, η and Γ, of each of the 14 profiles were allowed to vary freely. In the case of the former, the value was constrained to be between 0 and 1. An overall scale factor was also refined. For these constrained fits, a total of 31 free parameters were required.

The diffraction data from samples 1, 2 and 5 could not be fit with this approach, with the solution always diverging or parameters fitting to incomprehensible values. The reason for this is apparent, both if a few domains or the diffraction data from the samples are investigated: all of the domains within these samples show a random but coherent interlayering of bands with either a local fcc or hcp structure. This leads to diffraction composed of highly shifted and anisotropically broadened line-profiles from *both* the fcc *and* hcp structures. Equation 2.24 and the associated assumptions are then completely inappropriate.

Samples 4 and 6 show stacking disorder, but are generally much less severely disordered than samples 1, 2 and 5. As a result, the constrained fits of the diffraction data from these samples do not completely fail, but in general were very poor. In these samples, a second fit was performed, again assuming a pseudo-Voigt line-profile shape, but with no constraints on the profile parameters. In these cases, 56 free parameters were required.

In all the fits presented here, the fit quality index used was again R_{split}, as outlined in equation 3.8 within Section 3.2.2. In this case, the two different "groups" were the model fit and the synthetic powder diffraction data. By adopting this approach, the error associated with the modeling can be compared directly to the error associated with approximating the ensemble-average.

3.3.1.1 Sample 3

Sample 3 represents a powder with no stacking disorder, and a median domains size of 5 nm. A few selected domains are rendered in Figure 3.5. The powder diffraction data arising from samples 3 and the associated constrained fit and residual are shown in Figure 3.19. Table 3.3 reports the fitted shape parameters, FWHM and η, for each empirical profile, along with the integral breadth β. A Williamson-Hall analysis was also performed based on the fitted parameters, and is shown in Figure 3.19. The physical sample parameters retrieved from this LPA are presented in Table 3.4, along with corresponding true sample parameters, known *a priori*, and the fit quality index.

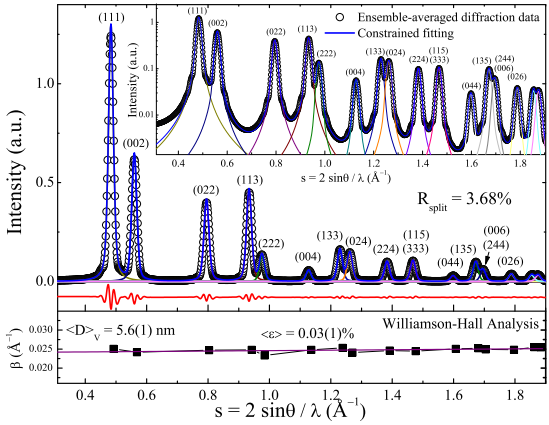

Figure 3.19: The powder diffraction data from virtual powder 3 is shown, fit with a constrained RS model assuming pseudo-Voigt profile shapes. Inset is the same, on a log-scale to highlight differences in the diffuse intensity. Below, the integral breadth β of each line profile has been plotted against the scattering vector s. The trend in β with s has been fit with a line, following typical Williamson-Hall analysis.

The fit quality index obtained for sample 3, $R_{split} = 3.68\%$, indicates that the error associated with approximating the powder diffraction data as a sum of constrained empirical profiles is larger than the error associated with the finite ensemble-average. The overall residual is

not independent, showing some level of positive correlation centered on the location of Bragg peaks. For some individual profiles, most notably the (111), the residual is asymmetric. It is likely that this misfit is associated with the assumption of a relatively simple, symmetric pseudo-Voigt line-profile shape; this empirical profile is not able to capture all fine details that underlie the true sample dataset pointed out in Section 2.5.2, such as profile asymmetries and the apparent violation of Bragg's law that occur even for otherwise perfect, finite domains.

profile	FWHM Γ (Å^{-1})	η	$\beta(\text{Å}^{-1})$
(111)	0.02056(4)	0.310(6)	0.02513
(002)	0.02052(7)	0.29(1)	0.02404
(022)	0.0205(1)	0.31(2)	0.02476
(113)	0.0206(1)	0.26(2)	0.02470
(222)	0.0211(3)	0.24(7)	0.02369
(004)	0.0207(8)	0.4(1)	0.02485
(133)	0.0201(3)	0.26(5)	0.02483
(024)	0.0208(4)	0.36(6)	0.02460
(224)	0.0206(4)	0.30(8)	0.02462
(115) & (333)	0.0205(4)	0.30(7)	0.02456
(044)	0.021(2)	0.4(3)	0.02512
(135)	0.0198(5)	0.29(8)	0.02452
(006) & (244)	0.0225(8)	0.2(1)	0.02568
(026)	0.021(1)	0.3(2)	0.02471

Table 3.3: Reported for each profile are the FWHM Γ and fraction Cauchy character η of the empirical pV profiles used within the constrained fit of the powder diffraction data from virtual powder 3, shown in Figure 3.19. Each profile is represented by its associated Miller indices (hkl). The resulting integral breadth β of each profile is also shown.

In terms of the retrieved physical parameters, the traditional constrained fit and resulting LPA as applied to virtual powder 3 tends to slightly *overestimate* both the volume-weighted mean domain size and the amount of microstrain, although only by a marginal or negligible amount for the latter. The lattice parameter a_c recovered from the fit is overestimated by about 0.04%. The Debye-Waller mean squared

displacement $\langle u^2 \rangle$ is overestimated: virtual powder 3 is technically a static snapshot, with no thermal motion. The picture painted by traditional LPA is then accurate to a degree, but some of the information provided is inaccurate, and *no information* is provided on the shape of the domain size distribution.

Sample 3		$R_{split} = 3.68\%$
Parameter	Constrained fit	True value
a_c (Å)	3.52153(6)	3.52000
$\langle D \rangle_V$ (nm)	5.6(1)	5.0
$\langle \varepsilon \rangle$ (%)	0.03(1)	0.00
$\langle u^2 \rangle$(Å^2)	0.01(1)	0.00

Table 3.4: The physical characteristics of virtual powder 3, obtained by constrained fitting of the powder diffraction data and subsequent Williamson-Hall analysis. Reported is the cubic lattice parameter a_c, the average microstrain $\langle \varepsilon \rangle$, the volume-weighted mean domain size $\langle D \rangle_V$, and an isotropic mean squared thermal displacement $\langle u^2 \rangle$ for the nickel atom. Also reported for comparison are the true characteristics of sample 3, known *a priori*

3.3.1.2 Sample 4

The domains in sample 4, rendered in Figure 3.6, show a degree of $R = 2$ type stacking disorder, and a median domain size of 5 nm. The fitted powder diffraction data and residual is shown in Figure 3.20, along with a Williamson-Hall plot. Table 3.5 displays the fitted line-profile shape parameters, while the physical sample parameters retrieved from the constrained fit and LPA are listed in Table 3.6.

There are several red-flags surrounding the constrained fit presented in Figure 3.20. The fit quality index $R_{split} = 11.0\%$ indicates that the error associated with the constrained model used here is much larger than the error associated with approximating the ensemble-average. The fit residual in Figure 3.20 suggests that the relative integrated intensities of the structure factor constrained model do not not match the data. A large amount of diffuse intensity between profiles is missing from the model, and the positions of several line-profiles, particularly the (002), do not match those in the observed data. Finally, within

profile	FWHM $\Gamma(\text{Å}^{-1})$	η	$\beta(\text{Å}^{-1})$
(111)	0.0267(2)	0.80(1)	0.03822
(002)	0.0416(8)	0.82(3)	0.06021
(022)	0.0247(7)	0.99(4)	0.03845
(113)	0.0235(4)	0.76(3)	0.03308
(222)	0.025(2)	0.8(1)	0.03580
(004)	0.040(8)	0.7(3)	0.05604
(133)	0.030(2)	0.6(1)	0.04025
(024)	0.023(1)	0.5(1)	0.02896
(224)	0.028(3)	0.9(2)	0.04165
(115) & (333)	0.025(2)	0.8(1)	0.03522
(044)	0.024(9)	0.9(6)	0.03478
(135)	0.023(2)	0.3(1)	0.02741
(006) & (244)	0.025(3)	0.3(3)	0.02869
(026)	0.05(1)	0.1(5)	0.04991

Table 3.5: The FWHM and fraction Cauchy character η are reported for the empirical pV profiles used within the constrained fit of the powder diffraction data from virtual powder 4. The resulting integral breadth β of each profile is also shown.

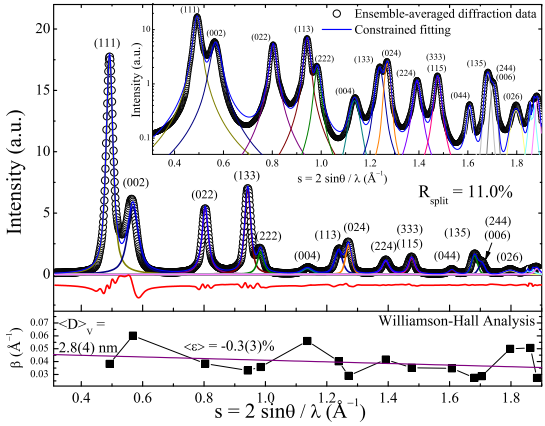

Figure 3.20: The constrained fit of the powder diffraction data arising from virtual powder 4 is shown, with the associated subsequent Willaimson-Hall plot shown below, where β of each line-profile is plotted against its scattering vector s. Also shown is the fit residual. Diffraction data and fit are also shown inset on a log-scale.

the Williamson-Hall plot, the integral breadth trend does not follow a straight line, seemingly violating the model behind equation 3.11, with extensive anisotropic line-profile broadening.

Together, these issues suggest that a model constrained in this way is inappropriate. The reason is apparent if the nature of the sample is considered. The domains composing sample 4 are characterized by a departure from three-dimensional periodicity. The use of Bragg's law and the unit cell structure factor to constrain the model are however based on an explicit assumption of three-dimensional periodicity, leading to equation 2.24. Naturally then, this constrained fitting approach fails.

Surprisingly, this poor quality of the fit is reflected only in some of the retrieved physical characteristics. The volume-weighted mean diameter is underestimated by about 44%, but other characteristics generally do not deviate significantly from their true values. The constrained model however does not consider disorder, and thus no information on the one-dimensional disorder is retrieved.

Sample 4		$R_{split} = 11.0\%$
Parameter	Constrained fit	True value
a_c (Å)	3.5195(5)	3.52000
$\langle D \rangle_V$ (nm)	2.8(4)	5.0
$\langle \varepsilon \rangle$ (%)	-0.3(3)	0.0
Ni $\langle u^2 \rangle$(Å^2)	0.078(3)	0.0

Table 3.6: The characteristics obtained by constrained fitting of the powder diffraction data from virtual powder 4. Reported are the recovered and true physical characteristics, including the cubic lattice parameter a_c, the average microstrain $\langle \varepsilon \rangle$ and the volume-weighted mean domain size $\langle D \rangle_V$, and an isotropic Debye-Waller mean squared atomic displacement $\langle u^2 \rangle$ for the nickel atom.

In light of the poor quality of the constrained fit, the diffraction data from sample 4 was also fit using an unconstrained model, with all profile parameters allowed to vary freely. The result of this fitting approach are shown in Figure 3.21, along with the resulting Williamson-Hall plot. The fitted profile parameters are reported in Table 3.8, along with the integral breadth β and the deviations Δx_0 in the profile positions with respect to what would be expected by applying Bragg's law for an ideal nickel structure.

In general, the fit is highly improved with respect to the constrained model, with a the fit quality index $R_{split} = 3.20\%$ (compared to the 11.0% seen for constrained fitting). The diffuse intensity between profiles is more accurately reproduced, as are the profile positions. While the fit is improved, the error associated with the fit is still greater than that associated with the finite ensemble-average approximation, the residual again shows a degree of correlation, and the fraction Cauchy character η fit to unphysical values greater than unity for several of the line-profiles, indicating a super-Lorentzian character.

Table 3.8 displays the physical sample parameters retrieved from this fit. It is worth noting that by adopting this unconstrained fitting approach, *all information* on atomic structure is lost: no lattice parameter or Debye-Waller mean squared atomic displacement can be retrieved easily, unless fitted peak parameters are analyzed *ex post facto*. The only information that can be estimated is microstructural,

profile	x_0(Å^{-1})	I(Å^{-1})	η	FWHM Γ(Å^{-1})	β(Å^{-1})	Δx_0(Å^{-1})
(111)	0.49265(3)	6.61(3)×10^8	0.716(9)	0.02814(9)	0.03748	-0.00059(3)
(002)	0.5621(1)	3.20(3)×10^8	0.60(2)	0.0449(2)	0.0573	0.0061(1)
(022)	0.80368(8)	1.98(2)×10^8	0.91(2)	0.0237(3)	0.0367	-0.00015(8)
(113)	0.94219(6)	2.37(3)×10^8	0.78(2)	0.0227(3)	0.0335	0.00003(6)
(222)	0.9829(2)	5.1(3) × 10^7	0.4(1)	0.024(1)	0.029	0.0012(2)
(004)	1.139(1)	2.7(3) × 10^7	0.8(3)	0.040(3)	0.054	-0.003(1)
(133)	1.2391(4)	8.4(4) × 10^7	0.90(8)	0.028(1)	0.042	-0.0008(4)
(024)	1.2697(2)	6.6(4) × 10^7	0.4(1)	0.022(1)	0.029	0.0007(2)
(224)	1.3922(6)	5.2(2) × 10^7	1†	0.0282(7)	0.045	-0.0004(6)
(115)& (333)	1.4755(6)	5.1(2) × 10^7	0.83(9)	0.024(6)	0.036	0.0007(6)
(044)	1.606(2)	1.4(2) × 10^7	1.0(3)	0.0236(6)	0.038	0.001(2)
(135)	1.6809(7)	4.2(4) × 10^7	0.4(2)	0.022(4)	0.027	-0.0002(7)
(006)& (244)	1.704(1)	3.2(5) × 10^7	0.8(2)	0.024(7)	0.035	0.000(1)
(026)	1.797(3)	2.3(4) × 10^7	1†	0.038(4)	0.061	0.000(3)

Table 3.7: Shown are the profile parameters resulting from the unconstrained fit of the diffraction data from sample 4. Also shown are the profile shifts Δx_0 from ideal Bragg position, and the integral breadths β of each profile. †Shape parameter persistently fit to unphysical value greater than 1 and thus was subsequently fixed to 1.

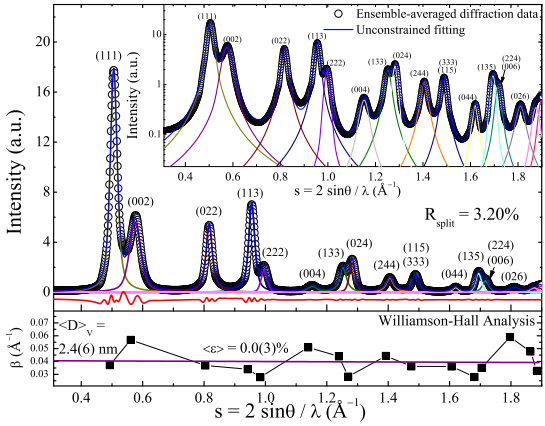

Figure 3.21: The unconstrained fit of the powder diffraction data from sample 4, shown on both a linear and log (inset) scale. A Williamson-Hall plot of the integral breadth β of each line profile against its scattering vector s is also shown. The trend in β with s has been fit with a line to extract the intercept and slope.

and even this information is inaccurate in this case, as it is based on Williamson-Hall analysis as manifested in equation 3.11, which assumes only size and mirostrain but not stacking disorder contribute to line-profile breadths. As a result, the mean domain size is again underestimated by about by about 40%. Thus, the unconstrained fitting approach does provide a higher quality fit, but provides no improvement in terms of understanding the sample, in fact it actually provides *less* information.

3.3.1.3 Sample 6

The domains in sample 6, rendered in Figure 3.8, show the same type and degree of stacking disorder as sample 4, and the same median size, 15 nm, as sample 7. The fitted powder diffraction data from samples 6 and fit residual are shown in Figure 3.22, along with a Williamson-Hall plot. Table 3.9 displays the fitted line-profile parameters, while the physical sample characteristics, retrieved from the fitting and sub-

Sample 4		$R_{split} = 3.20\%$
Parameter	Unconstrained fit	True value
$\langle D \rangle_V$ (nm)	2.4(6)	5.0
$\langle \varepsilon \rangle$ (%)	0.0(3)	0.0

Table 3.8: The physical sample characteristics obtained by unconstrained fitting the powder diffraction data from sample 4, with the unconstrained fit quality index R_{split}. Only the miscrostructural parameters are reported, as atomic information cannot be retrieved with an unconstrained model. Also reported for comparison are the true characteristics of sample 4, known *a priori*

sequent Williamson-Hall analysis, are listed in Table 3.10.

For sample 6, the constrained fit yields a fit quality index of $R_{split} = 11.8\%$, again suggesting that the error associated with fitting is greater than that associated with taking an approximate ensemble average. The constrained fit in this case shows problems similar to the constrained fit of the diffraction data from sample 4. The fit residual, as seen in Figure 3.22, shows positive correlation, several profiles fit to a super-Lorentzian shape, the relative intensities of the fit do not not match the data, a large amount of diffuse intensity is missing from the fit, and the position of several line-profiles do not match those in the observed data. Furthermore, the Williamson-Hall plot does not follow the linear trend predicted by equation 3.11, with all profiles, especially the (002) and (004), showing extensive anisotropic broadening.

The poor level of fit is also reflected clearly in the physical characteristics of the sample, retrieved from the fit and presented in Table 3.10. The volume-weighted mean domain diameter $\langle D \rangle_V$ is underestimated by 300%. An unphysical negative average microstrain is incorrectly found, the lattice parameter is underestimated by about 0.05%, and the mean squared thermal displacement of the nickel atom is overestimated.

The reason for the failure is again clear if the sample is considered. The domains composing sample 6 are characterized by a departure from three-dimensional periodicity. The use of Bragg's law and the unit cell structure factor as in equation 2.24 to constrain the fit explicitly imposes three-dimensional periodicity on the structure. Naturally then,

profile	FWHM $\Gamma(\text{Å}^{-1})$	η	$\beta(\text{Å}^{-1})$
(111)	0.01130(8)	1†	0.017767
(002)	0.0282(8)	0.91(4)	0.043239
(022)	0.0092(1)	1†	0.014656
(113)	0.0078(2)	1†	0.012363
(222)	0.0108(6)	1†	0.016895
(004)	0.026(9)	1†	0.040681
(133)	0.0142(7)	1†	0.021902
(024)	0.0081(5)	0.8(1)	0.011468
(224)	0.013(1)	1†	0.019784
(115) & (333)	0.0090(6)	1†	0.013915
(044)	0.008(2)	1†	0.012825
(135)	0.0077(7)	0.7(2)	0.010320
(006) & (244)	0.008(1)	0.7(3)	0.011900
(026)	0.02(1)	0.9(7)	0.032722

Table 3.9: Reported are the empirical profile parameters resulting from the constrained fit of the powder diffraction data from sample 6, along with the integral breadth β of each profile. †Shape parameter persistently fit to unphysical value greater than 1 and thus was subsequently fixed to 1.

Sample 6		$R_{split} = 11.8\%$
Parameter	Constrained fit	True value
a_c (Å)	3.5195(3)	3.52000
$\langle D \rangle_V$ (nm)	5(1)	15.0
$\langle \varepsilon \rangle$ (%)	-0.3(3)	0.000
$\langle u^2 \rangle (\text{Å}^2)$	0.067(6)	0.000

Table 3.10: The physical characteristics of sample 6, obtained by constrained fitting of the powder diffraction data are reported, along with the true characteristics of sample 6, known *a priori*. Also reported is the fit quality index R_{split}.

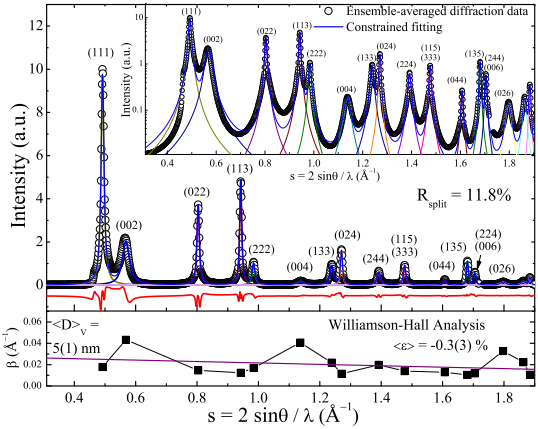

Figure 3.22: The powder diffraction data arising from virtual powder 6, fit with constrained model, and the subsequent Williamson-Hall analysis are shown. Shown also is the offset fit residual.

the constrained fit is of poor quality, and the retrieved parameters are unreliable.

Again, seeing the failure of a constrained model, the powder diffraction data from sample 6 was fit using an unconstrained model. The result is shown in Figure 3.23, along with a Williamson-Hall plot. Table 3.11 gives the fitted profile parameters using this approach, while Table 3.12 displays the physical sample characteristics retrieved from the fit.

The unconstrained fit represents an improvement over the constrained fit in terms of the level of agreement, with the fit quality index decreasing from $R_{split} = 11.8\%$ to 8.72%. This is still however greater than the error obtained by approximating the ensemble-average. The profile positions match the data, but the unconstrained fit is still plagued by problems, with many profiles fitting to a super-Lorentzian shape, missing diffuse intensity, and a fit residual showing clear positive correlation.

The microstructural information, estimated from the unconstrained fit is still inaccurate despite a slightly improved fit agreement. The

profile	x_0(Å^{-1})	I(Å^{-1})	η	FWHM Γ(Å^{-1})	β(Å^{-1})	Δx_0(Å^{-1})
(111)	0.49233(2)	1.71×10^{10}	1†	0.01112(6)	0.01747	-0.00027(2)
(002)	0.5636(2)	$1.00(1) \times 10^{10}$	1†	0.0304(5)	0.04779	0.0046(2)
(022)	0.80354(4)	$4.60(5)\times10^{9}$	1†	0.0077(1)	0.01214	-0.00001(4)
(113)	0.94226(3)	$5.82(6)\times10^{9}$	0.94(3)	0.0077(1)	0.01179	-0.00003(3)
(222)	0.9833(2)	$1.88(7)\times10^{9}$	1†	0.0121(6)	0.01902	0.0009(2)
(004)	1.139(2)	$8(1) \times 10^{8}$	1†	0.028(5)	0.04458	-0.002(2)
(133)	1.2381(3)	$2.11(8)\times10^{9}$	1†	0.0147(8)	0.02311	-0.0007(3)
(024)	1.2702(1)	$2.02(7)\times10^{9}$	0.92(9)	0.0081(4)	0.01231	0.0003(1)
(224)	1.3920(5)	$1.23(7)\times10^{9}$	1†	0.013(1)	0.02053	-0.0002(5)
(115)& (333)	1.4761(3)	$1.26(6)\times10^{9}$	1†	0.0087(5)	0.01369	0.0001(3)
(044)	1.6070(9)	$3.3(5) \times 10^{8}$	1†	0.008(2)	0.01230	0.0001(9)
(135)	1.6808(3)	$1.24(7)\times10^{9}$	0.8(2)	0.0077(5)	0.01100	-0.0001(3)
(006)& (244)	1.7041(5)	$8.2(6) \times 10^{8}$	1†	0.0089(9)	0.01391	0.0004(5)
(026)	1.797(3)	$6(1) \times 10^{8}$	1†	0.028(7)	0.04449	0.000(3)

Table 3.11: Shown are the profile parameters resulting from the unconstrained fit of the diffraction data from sample 6. Also shown are the profile shifts Δx_0 from ideal Bragg position, and the integral breadths β of each profile. †Shape parameter persistently fit to unphysical value greater than 1 and thus was subsequently fixed to 1.

Sample 6		$R_{split} = 8.72\%$
Parameter	Unconstrained fit	True value
$\langle D \rangle_V$ (nm)	5(2)	15.0
$\langle \varepsilon \rangle$ (%)	-0.2(4)	0.0

Table 3.12: The physical sample characteristics obtained by fitting the powder diffraction data from sample 6, with the unconstrained fit quality index R_{split}. Only the miscrostructural parameters are reported, as atomic information could not be retrieved with an unconstrained model. Also reported for comparison are the true characteristics of sample 6, known *a priori*

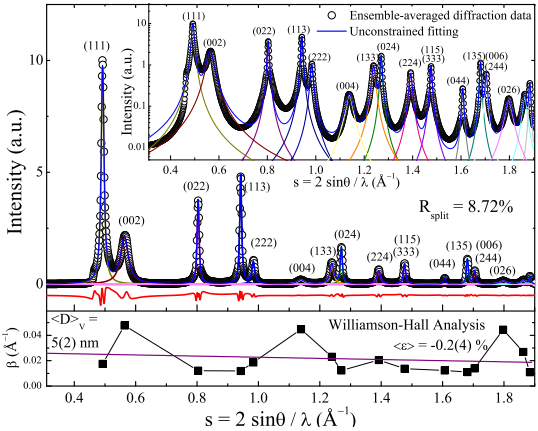

Figure 3.23: The unconstrained fit of the powder diffraction data from sample 6, shown on both a linear and log (inset) scale. A Williamson-Hall plot of the integral breadth β of each line profile against its scattering vector s is also shown. The trend in β with s has been fit with a line to extract the intercept and slope.

volume-weighted mean domain diameter $\langle D \rangle_V$ is still underestimated by 300%, and an unphysical negative average microstrain is again incorrectly found.

3.3.1.4 Sample 7

Sample 7 represents a powder with no stacking disorder, and median domains size of 15 nm. Figure 3.9 shows a few rendered examples of domains from this sample. Figure 3.24 shows the fitted powder intensity distribution and residual from samples 7, along with a Williamson-Hall plot. The fitted line-profile parameters are listed in 3.13, while the physical parameters of the sample, retrieved from the fit, are shown in 3.14, along with corresponding true samples 7 parameters.

While the constrained fit reproduces the diffraction data well, the fit quality index $R_{split} = 3.92\%$ indicates that more error is introduced by fitting than by approximating the ensemble-average. In general, the fit residual again shows positive correlation centered on the locations of

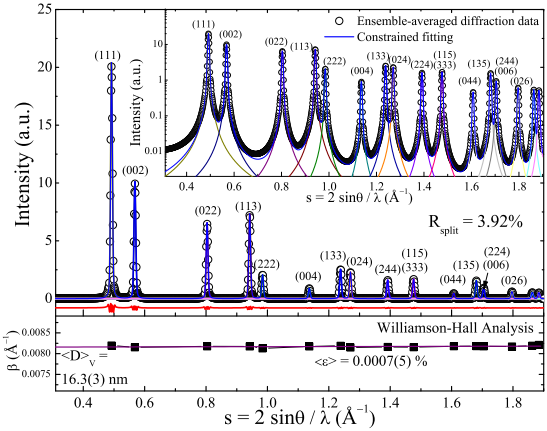

Figure 3.24: The constrained fit of the powder diffraction data from sample 7. Shown immediately below is the residual. Below the residual, the integral breadth β of each line profile has been plotted against the scattering vector s. The trend in β with s has been fit with a line, following typical Williamson-Hall analysis.

Bragg peaks. The Williamson-Hall plot is essentially linear.

As with sample 3, the constrained fitting of the diffraction data from sample 7 generally provides accurate physical sample characteristics, shown in Table 3.14. Both the volume-weighted mean domain size and microstrain are overestimated, but only slightly so. In this case, the latter is essentially estimated at zero, within error. The lattice parameter a_c is recovered more faithfully then was seen in the case of sample 3, but is still slightly overestimated. The Debye-Waller mean squared atomic displacement $\langle u^2 \rangle$ is retrieved faithfully.

In summary, empirical pseudo-Voigt profiles were employed to fit synthetic powder diffraction data from the nickel virtual powders outlined at the beginning of this chapter, following both an unconstrained approach and an approach constrained by the application of equation 2.24. Only 4 of the synthetic diffraction datasets could be fit through such an approach, while the remaining 3 datasets resulted in fits that diverged, or converged to truly nonsensical values, regardless of the starting parameters.

profile	FWHM Γ(Å^{-1})	η	β(Å^{-1})
(111)	0.00684(1)	0.279(5)	0.008247(1)
(002)	0.00684(2)	0.28(1)	0.008249(2)
(022)	0.00684(3)	0.28(2)	0.008245(3)
(113)	0.00684(3)	0.28(1)	0.008243(6)
(222)	0.00683(9)	0.31(6)	0.008341(8)
(004)	0.0068(2)	0.3(1)	0.008295(1)
(133)	0.00684(7)	0.29(4)	0.008291(3)
(024)	0.00684(8)	0.29(4)	0.008283(2)
(224)	0.0068(1)	0.28(6)	0.008252(5)
(115) & (333)	0.0068(1)	0.28(6)	0.008242(4)
(044)	0.0068(4)	0.3(2)	0.008323(3)
(135)	0.0068(1)	0.28(7)	0.008253(4)
(006) & (244)	0.0069(2)	0.3(1)	0.008400(5)
(026)	0.0068(3)	0.3(2)	0.008277(4)

Table 3.13: The FWHM and fraction Cauchy character η of the empirical pV profiles used to fit the powder diffraction data from virtual powder 7 are reported for each profile, represented by the Miller indices (hkl). The resulting integral breadth β of each profile is also shown

Sample 7		$R_{split} = 3.92\%$
Parameter	Constrained fit	True value
a_c (Å)	3.52017(2)	3.52000
$\langle D \rangle_V$ (nm)	16.3(3)	15.0
$\langle \varepsilon \rangle$ (%)	0.0007(5)	0.0
$\langle u^2 \rangle$(Å^2)	0.00(4)	0.0

Table 3.14: The characteristics obtained by fitting the powder diffraction data from virtual powder 7, along with the fit quality index. Also reported for comparison are the true characteristics of sample 7, known *a priori*

The condition for convergence in this case was the type of one-dimensional disorder: samples 1, 2 and 5 are characterized by an $R = 0$ type stacking disorder with an equal (or random) probability of each of the two layer-layer translations. This extreme disorder precludes any attempt to fit the data by employing perturbed models based fundamentally on three-dimensional periodicity, as the powder diffraction data is characterized by anisotropic line-profile broadening, profile position shifts, and the presence of new profiles. These complex features necessitate that all fitting techniques, both constrained and unconstrained, fail. This is a large shortcoming, and leaves an entire group of materials "uncharacterized."

Conversely, when the samples are characterized by an $R = 2$ type stacking process with a larger probability of stacking sequences resulting in a "normal" fcc structure, such as samples 4 and 6, the fitting approach employed in this section is more successful in reproducing the observed data. That being said, the physical characteristics, obtained partially by direct fitting and partially by *ex post facto* interpretation of the empirical profile shapes, are generally unreliable and inaccurate. Average domain sizes are underestimated and the refined lattice parameter deviates significantly more than is acceptable in a typical diffraction study.

The fitting approach employed in this section is most successful in reproducing the observed data for samples such as 3 and 7, characterized by an absence of stacking disorder, or an entirely fcc structure. In general, the physical characteristics of such samples are retrieved accurately and reliably, although only an average domain size is obtained with *no information* regarding the shape of the domain size distribution.

When a small degree of one-dimensional disorder, or stacking disorder, is introduced into the finite domains composing the sample, as in samples 4 and 6, constrained fitting approaches fail, both in reproducing the data, and in retrieving the physical sample characteristics. While a move towards unconstrained fitting can generally improve the quality of the fit, this entails an increase in the number of fitted parameters. Clear methods for translating these fitted parameters unambiguously to meaningful physical information *ex post facto* do not exist in a general sense. In any case, while the fit may improve, atomic-scale

information is completely lost by employing an unconstrained fitting technique, and the accuracy of the retrieved microstructural information is not significantly improved over constrained approaches.

Finally, it should be highlighted that the successful retrieval of sample characteristics in the ordered samples can be misleading. For all the datasets considered, the resulting fit error, measured by the factor R_{split}, was greater than the error introduced by approximating the ensemble-average. This indicates that there are some details of the line profiles that cannot be captured by fits based on empirical profiles.

3.3.2 Computing the FT directly using new models

The models employed in the previous section are based the assumption of empirical profiles (here equation 3.10 was used) and the application of Bragg's law with the traditional description of the structure factor of the unit cell, as embodied in equation 2.24. Subsequently, a Williamson-Hall analysis based on equation 3.11 was applied to obtain physical information on the sample microstructure.

This approach was reasonably successful for samples 3 and 7, showing no linear disorder. It was significantly less suscessful when linear-disorder was present, failing to retrieve accurate physical characteristics in the case of moderately disordered samples 4 and 6, and resulting in divergent fits in in the case of heavily disordered samples 1, 2, and 5.

An alternative approach is to make use of the models outlined in Section 2.6 to compute the model diffracted intensity, and to refine those model parameters directly, without resorting to empirical profiles. The equations outlined in this section take as input *only* the details of the stacking disorder and the domain morphology and size distribution, and provide directly the diffracted intensity distribution. Such an exercise, as applied to the 7 virtual powders outlined in this chapter, is the focus of this section.

The first step, as with any fitting approach, is to assume reasonable starting models. In this case, significant information on the samples is known *a priori*. In a real experimental case, such as that presented in Chapter 4, it is mandatory to first have a good understanding of the chemistry and the likely crystal structure of the sample, the type and extent of linear disorder, and the morphology and approximate size of

the domains. This is possible with careful synthetic control and an exploratory electron microscopy study.

The samples here are all composed of close packed polytypes of nickel, and thus the layer unit cell as outlined in Section 2.1 is assumed. The equivalent cubic lattice parameter a_c was refined and used to constrain the layer thickness c_l and lattice parameters $\mathbf{a}_l$ and $\mathbf{b}_l$ through equation 4.2. The one nickel atom in the layer unit cell is on a special site, and as a result its position was not refined here. An isotropic Debye-Waller factor $\langle u^2 \rangle$, representing the mean squared atomic displacement of the nickel atom, was also refined. This gave a total of 2 refined parameters associated with the atomic structure of the samples.

In this case, the stacking model outlined in Section 2.1 is assumed, allowing equation 2.87 to be used to describe the diffracted powder intensity distribution. As mentioned in Section 3.1.1, any $R = n$ stacking process can be successfully modeled by an $R \geq n$ stacking process. For the samples considered here, the largest Reichweite number is 2, and thus an $R = 2$ stacking process will be assumed for all samples, as governed by the probability matrix outlined in equation 3.3. With this model, two parameters, the transition probabilities α_{ff} and α_{bf}, were refined to describe the disorder. It should be pointed out that using the probability matrix shown in equation 3.3 within equation 2.87 is valid even when the structure is ordered, implying that $\alpha_{ff} = 1$ and $\alpha_{bf} = 0$.

It is known *a priori* that the domains composing the samples considered here show an isotropic morphology, with size governed by a log-normal distribution. With this in mind, the CVF arising from a log-normal distribution of spherical domains as written in equation 2.47 can be used to describe the broadening associated with finite crystal size. This entails the use of two refinable parameters governing the log-normal distribution, respectively the log-normal mean and standard deviation, μ and σ.

Including an overall scale parameter to account for proportionality, only 7 total parameters are required to fit the powder diffraction data in these samples. This represents an improvement over the fitting approach outlined in Section 3.3.1, where as few as 31 and as many as 56 free parameters were needed to fit the data. Moreover, each parameter used for fitting in this section is directly connected to a

physical characteristic of the actual sample, rather than being related to such a characteristic *ex post facto*.

The synthetic powder diffraction datasets from all virtual powders considered here were fit by using the above approach to compute the model data. The indicated 7 model parameters were varied to minimize the total sum of the squared difference between the model and the data through a gradient based algorithm. This all was as implemented in the Mathematica software package. The fits were performed five times for each sample, with starting parameters chosen randomly from a range of ±10% of the true parameter value. The best best fit of the five was taken.

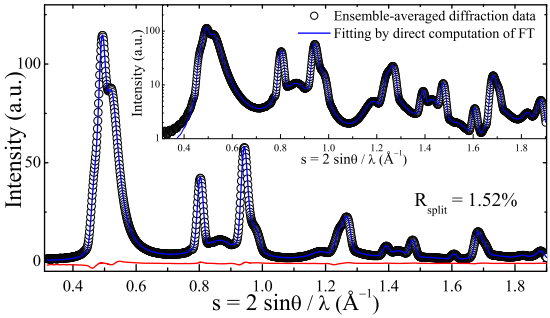

Figure 3.25: Shown is the synthetic powder diffraction data from sample 1, along with a fit using an approach where the FT is computed directly from physical characteristics of the sample. Both are shown on a linear and log (inset) scale. The fit residual is also shown.

The synthetic powder diffraction data from sample 1 is shown in Figure 3.25 on both a linear and log-scale, along with the fit as described above and the fit residual. In general, the fit agreement is exceptional, with $R_{split} = 1.52\%$ indicating a fitting error nearly equivalent to that associated with the ensemble-averaging process used to build the dataset. The fit residual is generally small across the scattering vector range considered, with the largest residuals concentrated about the location of Bragg peaks in an ideal nickel structure. It is not possible to compare this fit with one using empirical profile functions, as fitting with this approach completely failed.

Sample 1		$R_{split} = 1.52\%$
Parameter	Direct fitting	True value
a_c (Å)	3.520(4)	3.52000
$\langle u^2 \rangle (\text{Å}^2)$	0.0(1)	0.0
α_{ff}	0.50(5)	0.50
α_{bf}	0.49(4)	0.50
e^{μ} (nm)	4.97(8)	5.0
σ	0.02(2)	0.0

Table 3.15: Physical characteristics of sample 1 retrieved by directly fitting the powder diffraction data using expressions for the FT, along with the true sample characteristics for comparison. Reported is the

The size dispersion of the domains in sample 1 is best described by a Dirac distribution, while the stacking disorder is described by the $R = 0$ process leading to a transition probability matrix as in equation 3.1. Together these two phenomena require only 1 free parameter: the median of the Dirac distribution. By modeling these two features as as a log-normal distribution and an $R = 2$ process, respectively, an additional 3 parameters are introduced.

Considering the over-defined model, the physical characteristics of sample 1, obtained through direct fitting and reported in Table 3.15, are generally recovered well. The atomic structure is recovered exactly, while the details of the stacking process match almost exactly within error. The fitted fitted parameters μ and σ reproduce the true Dirac domain size distribution very well.

In Figure 3.26 the powder diffraction data from sample 2 is shown, along with the fit as described above, on both a linear and log-scale. The fit agreement is very good, with $R_{split} = 1.52\%$ again indicating a fitting error that is about equivalent to that associated with the ensemble-averaging process used to build the dataset. Across the scattering vector range considered the fit residual is generally small, with the largest residuals concentrated about the location of Bragg peaks in an ideal nickel structure. Again, the powder diffraction data from sample 2 could not be fit with empirical profiles following the approach outlined in Section 3.3.1.

The physical characteristics of sample 2 obtained through this fit are

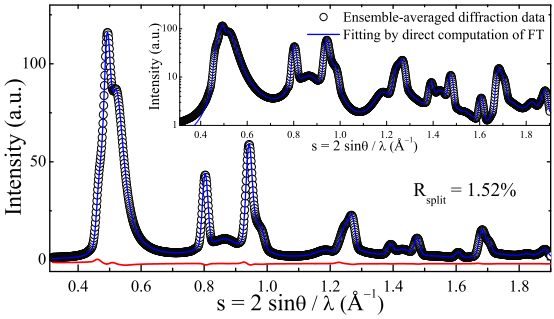

Figure 3.26: Powder diffraction data from sample 2 is shown with a fit done by directly computing the FT and refining the physical characteristics of the sample, on both a log (inset) and linear scale. The fit residual is also shown in red.

reported in Table 3.16. All characteristics are recovered with high accuracy. The best agreement is found in the case of the atomic structure, which is recovered exactly. The details of the stacking process match almost exactly within error but the estimated standard uncertainties on the refined transition probabilities are again large. The parameters of domain size distribution are also recovered accurately.

For sample 3, showing no linear disorder, the fit gives very high agreement with the synthetic powder diffraction data, and is presented in

Sample 2		$R_{split} = 1.52\%$
Parameter	Direct fitting	True value
a_c (Å)	3.520(3)	3.52000
$\langle u^2 \rangle$(Å^2)	0.0(2)	0.0
α_{ff}	0.49(2)	0.50
α_{bf}	0.50(5)	0.50
e^{μ} (nm)	5.01(7)	5.0
σ	0.11(6)	0.10

Table 3.16: Retrieved physical characteristics of sample 2, obtained by directly fitting the powder diffraction data using expressions for the FT

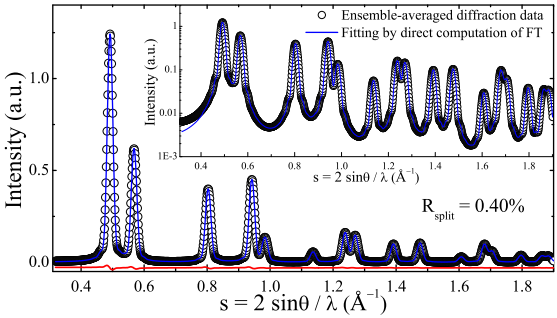

Figure 3.27: Shown is the powder diffraction data from sample 3 and the fit done by directly computing the FT. Both are shown on a linear and log (inset) scale. Shown below in red is the fit residual.

Figure 3.27. The fit error of $R_{split} = 0.40\%$ is very low, much lower than that associated with the finite ensemble average. The fit residual is nearly flat across the entire scattering vector range, with slight fluctuations at the location of Bragg peak maxima.

The fitted physical sample characteristics are shown in Table 3.17. In this case all characteristics are retrieved with near exact accuracy. The estimated standard uncertainties are also much lower, especially on the transition probabilities. This is likely because any small change from the three-dimensional periodicity entailed by $\alpha_{ff} = 1.0$ and $\alpha_{bf} = 0.0$

Sample 3		$R_{split} = 0.40\%$
Parameter	Direct fitting	True value
a_c (Å)	3.5200(1)	3.52000
$\langle u^2 \rangle$(Å^2)	0.00(1)	0.0
α_{ff}	0.999(1)	1.00
α_{bf}	0.000(2)	0.00
e^{μ} (nm)	5.02(5)	5.0
σ	0.100(9)	0.10

Table 3.17: Physical characteristics of sample 3 retrieved by directly fitting the synthetic powder diffraction data using expressions for the FT

represents a very large change in the diffracted intensity distribution, leading to a very steep objective function gradient.

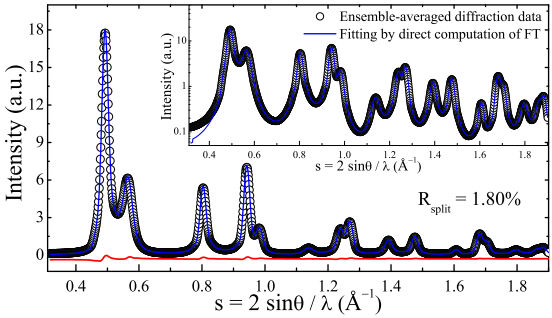

Figure 3.28: Shown is the synthetic powder diffraction data from sample 4 as well as the fit by directly computing the FT. Shown below in red is the fit residual.

Sample 4		$R_{split} = 1.80\%$
Parameter	Direct fitting	True value
a_c (Å)	3.5200(4)	3.52000
$\langle u^2 \rangle (\text{Å}^2)$	0.00(5)	0.0
α_{ff}	0.802(4)	0.80
α_{bf}	0.21(3)	0.20
e^{μ} (nm)	5.1(1)	5.0
σ	0.11(2)	0.10

Table 3.18: Physical characteristics of sample 4 retrieved by directly fitting powder diffraction data using expressions for the FT

The fit of the powder diffraction data from sample 4, showing an $R = 2$ linear disorder, is presented in Figure 3.28. It yields good agreement with the synthetic powder diffraction data, with a fit error of $R_{split} = 1.80\%$, equivalent to that associated with the finite ensemble average. The fit residual is again concentrated at the location of Bragg peak maxima.

Presented in Table 3.18 are the fitted physical sample characteristics.

All characteristics are recovered with high accuracy, but the best agreement is again found with atomic structure characteristics, which are recovered exactly within estimated uncertainty. The parameters of domain size distribution are also recovered accurately with low estimated uncertainties.

The α_{ff} transition probability matches almost exactly within error, with a low estimated standard uncertainty. Conversely, α_{bf} is retrieved with less accuracy and a higher estimated standard uncertainty. The relative large probability (0.80) of consecutive f transitions creates large blocks of consecutive f transitions which dominate the diffracted intensity distribution, and thus dominate the gradient of the fit objective function and the standard uncertainty estimates. The portions of defective structure created when the large blocks of consecutive f transitions are by chance interrupted tend to be more rare and smaller,and thus contribute relatively less to the diffracted intensity distribution. For this reason, the gradient of the fit objective function with respect to parameters governing these structural features (α_{bf}) is less steep, leading to a larger estimated error.

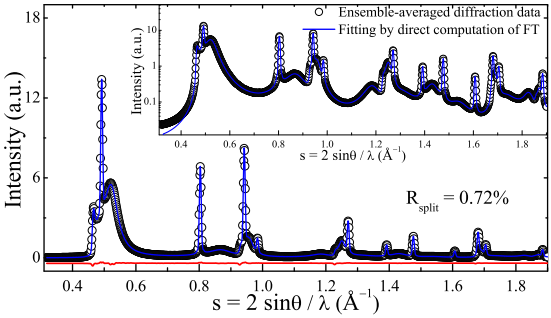

Figure 3.29: Powder diffraction data of sample 5 shown on a linear and log scale (inset). Also shown is the fit performed by directly computing the FT, along with the fit residual.

Like samples 1 and 2, sample 5 shows $R = 0$ linear disorder. Again, the model adopted here is over-defined, being intended for an $R = 2$ stacking process. That being said, the fit of the powder diffraction data from sample 5, presented in Figure 3.29, shows good agreement,

Sample 5		$R_{split} = 0.72\%$
Parameter	Direct fitting	True value
a_c (Å)	3.5201(2)	3.52000
$\langle u^2 \rangle (\text{Å}^2)$	0.0(1)	0.0
α_{ff}	0.49(3)	0.50
α_{bf}	0.50(4)	0.50
e^{μ} (nm)	15.2(3)	15.0
σ	0.10(1)	0.10

Table 3.19: Physical characteristics of sample 5 retrieved by directly fitting powder diffraction data using expressions for the FT

with a sufficiently low value of error, $R_{split} = 0.72\%$. The fit residual is nearly featureless, with small fluctuations at the the location of sharp Bragg-like features.

The physical characteristics retrieved by direct fitting are shown in Table 3.19, and generally agree well with the true sample characteristics. The estimated uncertainties on the transition probabilities are again large, as was seen in the other samples showing $R = 0$ linear disorder (samples 1 and 2). That being said, all characteristics are retrieved nearly exactly within estimated uncertainties. This represents a large improvement, as fits of this dataset employing empirical profiles complete diverged.

Sample 6		$R_{split} = 0.64\%$
Parameter	Direct fitting	True value
a_c (Å)	5.5200(3)	3.52000
$\langle u^2 \rangle (\text{Å}^2)$	0.00(4)	0.0
α_{ff}	0.799(1)	0.80
α_{bf}	0.21(3)	0.20
e^{μ} (nm)	14.9(2)	15.0
σ	0.098(1)	0.10

Table 3.20: Sample 6 characteristics, retrieved by direct fitting of the powder diffraction data using expressions for the FT

Like sample 4, sample 6 shows $R = 2$ linear disorder. The fit of the

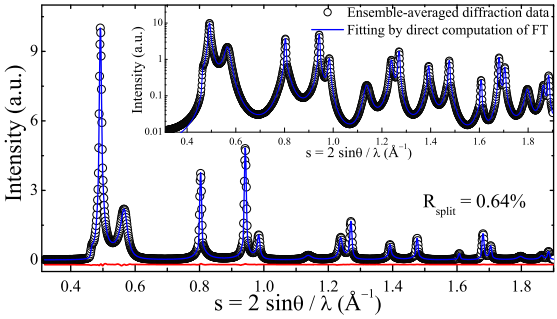

Figure 3.30: Shown on a log (inset) and linear scale is the powder diffraction data from sample 6 fit by directly computing the FT. The fit residual is also shown in red.

powder diffraction data from sample 6, presented in Figure 3.30, shows a high level of agreement, with an error of $R_{split} = 0.64\%$, lower than that associated with the finite ensemble average. The fit residual is nearly featureless, with very slight fluctuations at the the location of sharp Bragg-like features.

The fitted physical sample characteristics are shown in Table 3.20. In this case all characteristics are retrieved with exact accuracy, within the bounds of the low estimated uncertainties.

Sample 7		$R_{split} = 1.08\%$
Parameter	Direct fitting	True value
a_c (Å)	3.52000(6)	3.52000
$\langle u^2 \rangle$(Å^2)	0.000(1)	0.0
α_{ff}	1.000(1)	1.00
α_{bf}	0.000(2)	0.00
e^{μ} (nm)	15.00(6)	15.0
σ	0.100(2)	0.10

Table 3.21: Sample 7 characteristics, retrieved by direct fitting of the powder diffraction data using expressions for the FT

Sample 7 represents an ideal fcc nickel powder with no stacking dis-

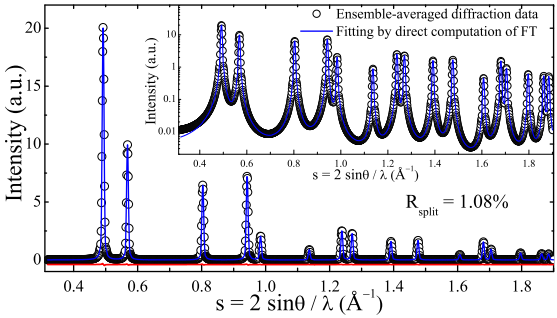

Figure 3.31: Shown on a log (inset) and linear scale is the powder diffraction data from sample 7 fit by directly computing the FT. The fit residual is also shown in red.

order. The powder diffraction data and fit are shown in Figure 3.31. Again, the fit reproduces the data very well, with a low error of $R_{split} = 1.08\%$. The fitted physical sample characteristics are shown in Table 3.21. In the case of this idealized powder, all characteristics are retrieved with exact accuracy, within the estimated uncertainties, which themselves are very low compared to those of the other samples.

In summary, for each of the 7 synthetic diffraction datasets analyzed in this section, a direct fitting approach was applied. Equations 2.47 and 3.3 were used to describe, respectively, the diffraction broadening effect of a polydisperse finite domain size and transition matrix governing the one-dimensional disorder. These two equations were substituted into equation 2.87 to compute the diffracted intensity directly. By optimizing the physical characteristics, a best-fit was found between the modeled and synthetic diffraction data, without invoking empirical profile functions. For all the datasets considered, the resulting fit error, measured by the factor R_{split}, was less than the error introduced by approximating the ensemble-average. In all cases, the direct fitting procedure retrieved exact or nearly exact sample characteristics with relatively low estimated uncertainties. The lowest uncertainties were achieved in samples with less linear disorder, on characteristics pertaining to atomic structure.

3.4 Concluding remarks

This chapter outlined the procedure for creating a virtual atomistic powder sample. First, models were outlined for governing the general powder ensemble characteristics, such as domain size and atomistic layer arrangements. A spherical morphology was adopted with domain diameters distributed log-normally. A layer description of the nickel structure was adopted from the work of Warren [21], and a simple Markov model was employed to describe stacking sequences assuming only either f or b relative layer translations were possible.

Markov chains and log-normal distributions, as applied here, are however abstractions derived to reduce the amount of information necessary to describe a large ensemble. The distribution of domain sizes in a real sample may or may not be accurately described as "log-normal," and the layer stacking sequences may or may not be accurately described by a Markov chain. These assumption are employed here because they provide relatively simple and appropriate examples that can be used to test the accuracy and reliability of the different RS models outlined in Chapter 2.

Through use of the DISCUS software package [130], atomistic powders with known characteristics were constructed. The DSE (equation 3.7) was used to compute the powder averaged diffracted intensity distribution from each domain and these intensity distributions were averaged for each sample. A novel approach was outlined for determining the degree of convergence of the ensemble-averaged diffracted intensity distributions, borrowed from serial femtosecond crystallography[139]. Using this approach, the minimum library size necessary for reproducing an approximate ensemble-average faithfully was established and investigated as a function of sample characteristics.

The use of the DSE closely resembles a true diffraction experiment, at least more so than the use of the RS models outlined in Chapter 2. When applying the DSE, only configurations which are explicitly present are considered, just as with a true diffraction experiment. With this in mind, it is interesting to note that for all of the samples considered here, libraries of less than 650 configurations were required to reach a reasonable level of convergence. In some cases, as few as 177 domains were necessary. This introduces some ambiguity into the diffraction measurement: it is not possible to distinguish between a

true powder ensemble dictated by the general characteristics, containing millions of domains, and one composed of just the finite library necessary to produce a reasonably converged ensemble average.

Having established the approximate convergence of the diffraction data from the virtual powders, two different data fitting approaches were applied, based on two different RS models from Chapter 2. The first model was based on empirically broadening a powder pattern derived from the assumption of three-dimensional periodicity and large crystals, as per equation 2.24. In general, this method completely failed in both fitting the data and retrieving sample characteristics when significant stacking disorder was present. When only a limited amount of stacking disorder was present, the model was successful in reproducing the experimental data (to an extent) but the characteristics of the sample were not retrieved reliably or accurately. When no stacking disorder was present, the model was successful both in reproducing the experimental data and accurately retrieving the characteristics of the sample.

These results are important, because they demonstrate the perils associated with applying models in situations where their base assumptions are not satisfied. In some cases, the samples considered here deviated enough from the assumptions of the model to clearly guarantee the failure of data fitting. However in other cases the deviations from the model assumptions are not significant enough to guarantee failure of the fitting. In these cases, fitting of the data is *successful*, but the retrieved sample characteristics are completely *nonsensical*. Such perils can only be avoided in the case of real samples if complementary characterization approaches are applied. Diffraction is not by any means a characterization approach that can provide complete understanding of the sample, but rather it must exist as part of a vast tool-set.

With the shortcomings of these models established, a more physically reasonable model was used to fit the synthetic powder diffraction data from these samples. With this approach, the parameters of the domain size distribution, the layer transition probabilities, and the atomic unit cell of the layers were used directly in equation 2.87 to fit the powder diffraction data.

By adopting this approach, each powder diffraction dataset from the 7 virtual powders considered here was successfully fit, with fit quality

indices indicating that the fit error was lower than or about equivalent to that introduced by approximating the finite ensemble average. Beyond the high level of agreement between the fit and the diffraction data, the physical characteristics of each of the 7 virtual powders were retrieved accurately, even in cases where a somewhat inappropriate stacking model was assumed (for example, when an $R = 2$ stacking model was used to fit diffraction data from samples 1, 2, 3, 5 and 7, which were characterized by an $R < 2$ stacking processes).

In such direct fitting situations, the first and most important step is always an assumption of the proper models. In the cases presented in this chapter, the fitting procedure benefited enormously from prior knowledge of the true sample characteristics. With this information, it was trivial to assume the correct models and proceed with the analysis. it should be stressed again that, when considering a real powder sample, acquisition of such information requires the application of many different and overlapping characterization techniques.

A final word should be devoted to the atomistic virtual powders themselves. Each domain within these samples represents an idealized and static snapshot, and does not necessarily represent a physically feasible atomic configuration. The primary aim of this study was testing data fitting approaches based on various different models. Thus, the physical accuracy of the domains themselves is irrelevant, and the only important point is that the synthetic powder diffraction data, approximated by a finite ensemble average, accurately represents the true ensemble average for a given set of chosen sample characteristics.

That being said it is likely that the defects introduced by perturbing the spatially infinite, three-dimensionally periodic crystal, (i.e. stacking disorder and domain boundaries) in some cases lead to physically unreasonable configurations that should either be eliminated from the virtual powder or altered somehow. Alteration could be achieved through a suitable molecular dynamics simulation, with an appropriate energy minimization and/or thermalization. Such a procedure could be useful for investigating the physical accuracy of both the virtual powders themselves and the assumptions necessary to model their synthetic powder diffraction data.

The next chapter follows a path similar to this chapter, but rather than considering synthetic powder diffraction data from atomistic vir-

tual powders, real powder diffraction data is considered from nanostructured boron nitride samples.

Chapter 4

Practical application: boron nitride

Recently several authors have reported different polycrystalline boron nitride (BN) samples with improved hardness, thermal stability, and fracture toughness [125, 143, 144]. All authors report structural fluctuations at the nanoscale, with electron micrographs suggesting extensive "banding" within individual domains, which themselves show an isotropic morphology and are generally less than 50 nm in size [125, 126]. The powder diffraction patterns vary from sample to sample and from study to study, but generally show some common characteristics including anisotropic line-profile broadening and shifting, as well the presence of incomplete sets of diffraction peaks from two different polytypes of BN with unexpected relative peak intensities [125, 126].

Lacking definitive quantitative diffraction analysis, authors have put forward many conflicting hypotheses regarding the identity of improved BN samples. Some authors have suggested samples are "aggregated nanocomposites," essentially proposing sintered mixtures of the two polytypes [143]. Others have proposed that samples are either "nanostructured" [144, 145] or "nanotwinned" [125] single-phase BN. Unfortunately this confusion in sample identity has prevented a comprehensive understanding the physical processes behind the improvement in properties. To date, no definitive conclusion has been reached regarding the nanostructuring in such BN samples.

The cubic polytype of BN, or c-BN, crystallizes in the $F\bar{4}3m$ space group, with a lattice parameter of $a_c = 3.615$ Å [146], and is completely isostrucutural with cubic diamond. A schematic of the c-BN unit cell

is shown in Figure 4.1a. This polytype is common in numerous industrial applications, typically as an abrasive in cases requiring thermal or chemical stability beyond that of harder, diamond-based abrasives.

Much like diamond, a second sp^3-bonded polytype of BN has been reported. Crystallizing in the $P6_3/mmc$ space group with lattice parameters $a_w = 2.55$ Å and $c_w = 4.17$ Å, it is often called wurtzite-type BN, or just w-BN, and is isostrucutral with the lonsdaleite phase of diamond [147, 148]. A schematic of the w-BN unit cell is shown in Figure 4.1b.

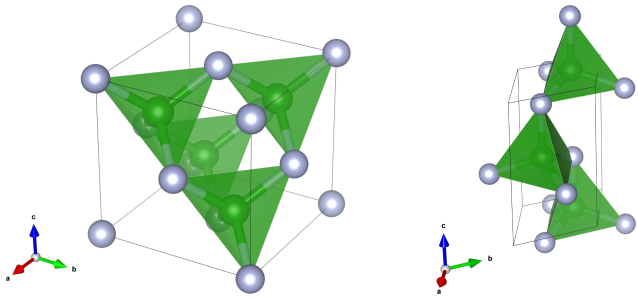

(a) c-BN (b) w-BN

Figure 4.1: Perspective views of the unit cells of two different sp^3-bonded polytypes of boron nitride

This chapter is focused on testing two different approaches for quantitative analysis of the powder diffraction data from several nanostructured BN samples, with the ultimate aim of understanding atomic, nano, and microstructure of these samples. The first approach is based on an assumption of two-phase samples, while the second is based on the assumption of single-phase samples showing stacking disorder.

4.1 Experimental

The syntheses of all nanostructured BN samples showing improved properties follow similar routes: a nanocrystalline form of the sp^2-bonded (graphite-like) BN polytype, crystallizing in the space group $P6_3/mmc$, is subjected to high-pressure high-temperature (HPHT)

treatments, and undergoes a phase transformation to an sp^3-bonded polytype [125, 126, 146, 147]. At sufficiently high temperatures and pressures, complete transformation to c-BN is observed [147]. The identity of the products at intermediate temperatures and pressures is still unclear and the subject of contention in the literature [125, 126, 145, 149].

The 6 samples investigated here were first reported by Tian *et al.* [125]. In their work, nanostructured turbostratic sp^2-bonded BN "nano-onions" were subjected to HPHT treatments at various pressure-temperature combinations. The subset of samples considered here were all treated at 15 GPa. Electron micrographs, available in the original work, show approximately equiaxed individual domains, less than 50 nm in diameter, containing nanostructural "bands" that the original authors call "nanotwins" [125].

The powder X-ray diffraction pattern for each sample was collected on a laboratory diffractometer (D8 Discover) in Bragg-Brentano geometry using copper radiation without a monochromator. The instrumental contribution to line profile-broadening was obtained by fitting pseduo-Voigt profiles to the powder diffraction data of a microcrystalline silicon sample, collected in the same instrumental geometry. By parameterizing the squared FWHM of the resulting line-profiles using a Caglioti-type second degree polynomial in $\cos\theta$ with coefficients $U = 0.0028, V = 0.013, W = -0.0029$ [150], and and a Cauchy mixing parameter η using a second degree polynomial in θ ($\eta(\theta) = a\theta^2 + b\theta$ with $a = 0.14, b = 0.011, c = 0$), the θ dependence of the instrumental contribution to line-profile shape was estimated and included by numerical convolution.

4.2 Diffraction fitting

4.2.1 Two-phase models

Just as in Section 3.1.1, the first step to quantitative diffraction analysis is choosing appropriate models. As mentioned, some authors have hypothesized that nanostructured BN samples are sintered two-phase mixtures of c-BN and w-BN. Employing such a model and assuming three-dimensionally periodic phases implies the existence of Bragg peaks within the powder diffraction patterns. From $25° < 2\theta < 100°$,

there are 15 distinct Bragg peaks, 10 arising from w-BN and 5 from c-BN. Fitting each peak with a pseudo-Voigt function with unconstrained shape parameters requires the use of 30 free parameters. If the position of each profile is constrained by Bragg's law, three further parameters are required, two due to w-BN, and one from c-BN.

The profile area can be constrained by the structure factor, but choices must be made regarding which atomic structure parameters to refine. Boron and nitrogen are similar in atomic number, so only one shared isotropic Debye-Waller factor $\langle u^2 \rangle$ is refined per phase. Within both the c-BN and w-BN unit cells, all atoms sit on special sites, and the symmetry of the unit cells is such that only the z-coordinate of nitrogen in the w-BN structure could be refined; it is however here held constant. The atomic structure constraints thus entail only 2 additional free parameters.

Additionally, a linear sample displacement correction s was refined, allowing for a point-wise shift in θ, based on the equation $\Delta 2\theta = -\frac{180s}{\pi} \cos\theta$ (in degrees), where s represents twice the ratio of the linear sample displacement to the diffractometer goniometer radius. Furthermore, the coefficients of a third degree polynomial in θ were refined to fit the background. Adding a scale term for each phase entails 2 additional parameters, bringing the total number of parameters for this two-phase fit to 41. The number of parameters could be reduced if the shape of each profile was constrained through some equation, for example equation 3.11, but this approach is not adopted here.

The adoption of models in this way allows for the use of the equations outlined in Chapter 2 for approximating the powder diffraction data as a sum of empirical profiles. For each of the 6 samples investigated here, equation 2.24 was used, as implemented within the fityk v0.9.8 software package [142], to model the powder diffraction data from each sample. The atomic parameters of the sample and the empirical profile shapes were refined by minimizing the weighted sum of the squared differences between the observed and and modeled data, using a local gradient approach.

4.2.2 Single-phase models

As already mentioned, electron microscopy studies suggest that the samples are nanocrystalline, with extensive "banding" [125]. This

nanoscale banding, together with the strange anisotropic powder diffraction features, suggest the presence of stacking disorder, a hypothesis also proposed in the literature [125, 126, 145, 149]. Stacking disorder in BN samples is best understood within the context of the two main sp^3-bonded polytypes. By viewing projections of the c-BN and w-BN polytypes, as shown in Figures 4.2a and 4.2c, respectively, it is clear that both can be described as *different* relative arrangements of the *same* atomic scale layer, just as in the case of the fcc and hcp polytypes outlined in Section 2.1.

In fact, the only differences between the nickel and BN cases are the contents and absolute dimensions of the layer unit cell. With the $p6mm$ layer group, the layer unit cell common to both BN polytypes is shown in 4.2b, and contains one boron at (0,0,0) and one nitrogen at (0,0,0.75), both on $1a$ Wyckoff sites. Only one shared isotropic Debye-Waller factor $\langle u^2 \rangle$ is refined for the layer unit cell, with the positions of the atoms held constant.

The layer unit cell vectors $\mathbf{a}_l$ and $\mathbf{b}_l$ and layer thickness c_l can be described through a transformation of either the c-BN or w-BN unit cells, written as either

$$\mathbf{a}_l = -\frac{\mathbf{a}_c}{2} + \frac{\mathbf{b}_c}{2}, \tag{4.1a}$$

$$\mathbf{b}_l = -\frac{\mathbf{b}_c}{2} + \frac{\mathbf{c}_c}{2} \tag{4.1b}$$

$$c_l = \frac{1}{3} \left\| \mathbf{a_c} + \mathbf{b_c} + \mathbf{c_c} \right\|, \tag{4.1c}$$

or

$$\mathbf{a}_l = \mathbf{a}_w \tag{4.2a}$$

$$\mathbf{b}_l = \mathbf{b}_w, \tag{4.2b}$$

$$c_l = \frac{1}{2} \left\| \mathbf{c_w} \right\|, \tag{4.2c}$$

where $\mathbf{a}_c$, $\mathbf{b}_c$, and $\mathbf{c}_c$ are the c-BN unit cell vectors, and $\mathbf{a}_w$, and $\mathbf{b}_w$ are the w-BN unit cell vectors.

The shape of layer unit cell is slightly different depending on whether the c-BN or w-BN unit cell vectors are transformed. Specifically, the symmetry of the c-BN unit cell dictates that only the cubic lattice parameter $a_c = \|\mathbf{a_c}\| = \|\mathbf{b_c}\| = \|\mathbf{c_c}\|$ is used to constrain the layer unit cell shape, whereas the symmetry of the w-BN unit cell dictates the hexagonal lattice parameters a_w and c_w are both used to constrain the layer unit cell shape, as the ratio c_w/a_a is not ideal in the w-BN unit cell. In practice, this amounts to either allowing both the layer thickness c_l and lattice parameter a_l to vary freely, or allowing just the layer lattice parameter to vary freely and constraining the layer thickness through $c_l = \sqrt{2/3}a_l$. Throughout this chapter, the latter approach is adopted in all fits, necessitating two fit parameters for the atomic structure ($\langle u^2 \rangle$ and a_l).

The c-BN and w-BN polytypes can be constructed by considering *relative* horizontal positions of two adjacent atomic layers. A "forward" shift, represented by the relative position vector $\mathbf{R}_f = \frac{\mathbf{a}_l}{3} - \frac{\mathbf{b}_l}{3} + c_l\hat{\mathbf{z}}$, or a "backward" shift, represented by the relative position vector $\mathbf{R}_b = -\frac{\mathbf{a}_l}{3} + \frac{\mathbf{b}_l}{3} + c_l\hat{\mathbf{z}}$ are the only two possibilities. The c-BN polytype is constructed by repeating the same translation, while the w-BN polytype is constructed by alternating translation types. Within this section, $\mathbf{R}_f$ and $\mathbf{R}_b$ were not varied as part of the fitting process.

As a note, a alternative stacking model could be envisioned, where two distinct atomic scale layers were used to construct the two polytypes. In this case, both layers would be primitive hexagonal lattices containing either a boron or a nitrogen atom. By constraining the transition probabilities to force an alternation of these two different layer types with the correct stacking vectors, both the c-BN and w-BN polytypes could in theory be constructed. This however introduces an unnecessary complexity into the Markov process and the above specified simpler stacking model is preferred.

The arrangement of the atomic scale layers is modeled by a Markov process, as outlined in Section 2.7. The similarity to the case of the fcc and hcp polytypes is again exploited when discussing the interaction range or Reichweite number R of this system. The description outlined in Section 3.1.1 can in fact be completely lifted and brought here, allowing for the use of either equation 3.1, 3.2, 3.3, or 3.4 to describe the probability matrix $\mathbf{T}$ of the Markov process describing the layer

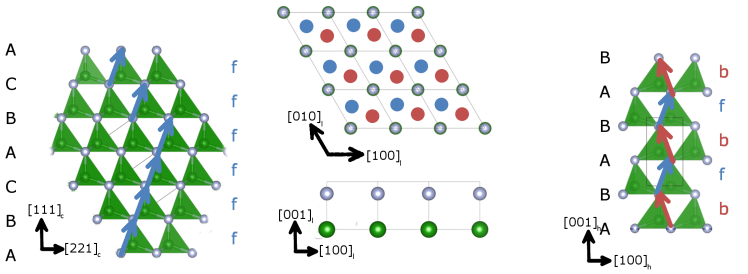

(a) c-BN unit cells (b) common layer unit cell (c) w-BN unit cells

Figure 4.2: In (a), a projected view of several c-BN unit cells is shown, with the Warren layer type identified at left, and relative translation identified at right. The same is shown in (c) for several idealized w-BN unit cells. In (b), the layer unit cell common to both polytypes is shown, both in a top and front view. The indicated directions are with respect to the lattice of the closest pictured structure. Forward or backward relative translations are indicated by the color blue or red, respectively

arrangements. The finite states machines of Markov processes with varying interaction ranges are shown in Figure 4.3.

In this chapter, the $R = 0$ stacking process was not adopted, as it offers no degrees of freedom in terms of the layer arrangements. The $R = 1$ stacking process offers only one degree of freedom in terms of the layer arrangements, and leads to cubic and relatively twinned cubic regions of the same average size. This is contradicted by experimental observation, as Tian *et al.* reported smaller relatively twinned cubic bands, based on electron microscopy studies [125]. For these reasons, throughout this section a $R = 2$ stacking process as described by equation 3.3 is assumed for describing the layer arrangements. This entails two fit parameters associated with layer correlations, namely α_{ff} and α_{bf}.

Electron micrographs rule out the presence of strongly anisotropic morphologies, instead indicating that the domains composing the sample adopt what is essentially an equiaxial or spherical morphology [125]. For this reason, a spherical crystal shape function was adopted in this

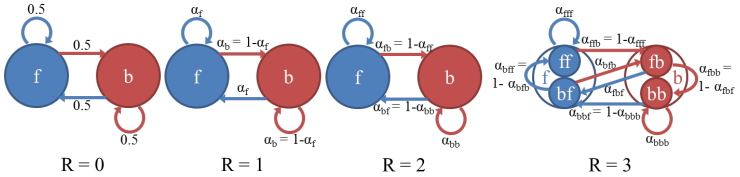

Figure 4.3: Finite state machines for modeling stacking disorder in BN

section. A log-normal distribution was assumed to describe the dispersion of the domain diameters, yielding two fit parameters associated with crystal morphology, namely μ and σ, the log-normal mean and standard deviation, respectively.

Again, a linear sample displacement correction s and the coefficients of third degree polynomial in θ were refined, to account for a linear sample displacement and background, respectively. All total and including a scale factor, 11 parameters were necessary to directly fit the powder diffraction datasets using this approach. The parameters refined for each sample, their physical meanings, and their boundaries, when imposed, are presented in Table 4.1.

Parameter	Physical meaning	Boundaries
h	overall scale	$h > 0.0$
$a_c = 2\sqrt{2}a_l$	layer lattice	3.59 Å $< a_c <$ 3.63 Å
$\langle u^2 \rangle$	isotropic Debye-Waller mean squared thermal displacement (both B and N)	0.0 Å^2 $< \langle u^2 \rangle <$ 4.00 Å^2
s	sample displacement	-
α_{ff}	probability of f transition given a previous f transition	$0.0 < \alpha_{ff} < 0.50$
α_{bf}	probability of f transition given a previous b transition	$0.0 < \alpha_{bf} < 1.00$
μ	log-normal mean and standard deviation of domain diameter distribution	0.0 Å $< 4/3e^{\mu+7/2\sigma^2} <$ 10^3 Å
σ		
a_1	Background polynomial coefficients	
a_2		
a_3		

Table 4.1: A complete list with physical meanings and imposed boundaries of all fitted parameters used in the single-phase fits

Adopting such models for the samples allows for the use of equation 2.87 to compute the diffracted intensity distribution. For each of the 6 samples investigated here, a manual optimization of fit parameters was first made to provide reasonable starting values. The parameters were then refined by minimizing the weighted sum of the squared dif-

ferences between the observed and modeled data using a local gradient approach.

4.3 Fitting results

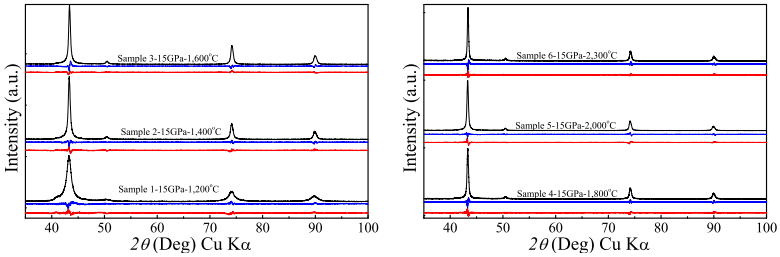

(a) Samples 1-3

(b) Samples 4-6

Figure 4.4: Shown is the X-ray powder diffraction data of each BN sample considered here (with processing temperature/pressure listed). Below each powder diffraction pattern is a fit residual associated with the two-phase Rietveld fit (red lines) or the single-phase fit incorporating one-dimensional disorder (blue lines)

The experimental powder diffraction data from each sample is shown in Figure 4.4, with fit residuals from the two different models shown offest below the diffraction data.

The two different fitting approaches each provide a different set of information. By applying a two-phase approach with empirical profiles, the integral breadth of each profile can be extracted *ex post facto* and used in a Williamson-Hall analysis for each phase, based on equation 3.11. This provides a volume-averaged strain and domain diameter, if equiaxed domains are assumed. Additionally, the lattice parameters and the shared isotropic Debye-Waller factor for each phase are directly retrieved from the fit. All physical characteristics retrieved from the two-phase fits are reported in Table 4.2, along with the goodness-of-fit indices [151].

Adopting a direct modeling approach assuming one-dimensional disorder yields a different set of information from each sample. Again, the

Parameter	Sample 1	2	3	4	5	6
GoF	1.15	1.10	0.87	1.08	0.78	1.05
s	0.10(1)	0.064(5)	-0.04(4)	0.087(4)	0.106(4)	0.029(3)
c-BN						
a_C (Å)	3.6203(4)	3.6182(1)	3.6176(1)	3.6163(1)	3.6170(1)	3.6156(1)
$\langle u^2 \rangle$(Å^2)	0.0128(5)	0.0080(4)	0.00(5)	0.0120(4)	0.0202(5)	0.0176(5)
$\langle D \rangle_V$ (nm)	18(2)	28(2)	29.7(8)	49(2)	51(2)	100(6)
$\langle \varepsilon \rangle$ (%)	0.2(1)	0(3)	0.0(2)	0.02(1)	0.02(2)	0.3(1)
w-BN						
a_W (Å)	2.460(4)	2.408(8)	2.427(6)	2.41(1)	2.319(5)	2.45(4)
c_W (Å)	3.99(2)	4.24(2)	4.23(2)	4.20(3)	4.39(1)	3.978(8)
$\langle u^2 \rangle$(Å^2)	0.58(6)	0.39(4)	4.0(2)	0.0(2)	0.0(2)	0.0(2)
$\langle D \rangle_V$ (nm)	4(3)	3.4(5)	3.2(7)	10(12)	10(14)	13(40)
$\langle \varepsilon \rangle$ (%)	2(5)	2(1)	1(2)	1(7)	1(4)	1(5)

Table 4.2: Physical characteristics for BN samples, retrieved by fitting powder diffraction data using a two-phase model with empirical profiles

lattice parameters and the shared isotropic Debye-Waller factor are directly retrieved from the fit. However, $R = 2$ layer-layer correlation probabilities are also retrieved, as well as the log-normal mean and standard deviation of a log-normal distribution describing the domain diameters. These physical characteristics are listed for each sample in Table 4.3, with the fit quality indices, for each of the 6 samples considered here.

Parameter	Sample 1	2	3	4	5	6
GoF	1.21	1.06	0.99	1.13	0.86	1.15
$a_C = 2\sqrt{2}a_l$ (Å)	3.6169(3)	3.6144(1)	3.6137(1)	3.6131(1)	3.61324(7)	3.6130(1)
$\langle u^2 \rangle$(Å^2)	0.011(2)	0.0095(6)	0.0076(5)	0.0068(4)	0.0057(1)	0.0038(2)
s	0.8(5)	0.6(2)	-5.7(2)	-0.3(2)	0.6(2)	-3.6
α_{ff}	0.924(1)	0.9510(7)	0.9624(6)	0.9759(5)	0.9760(8)	0.9855(5)
α_{bf}	0.44(3)	0.28(2)	0.27(3)	0.25(3)	0.27(5)	0.27(4)
μ	3.2(5)	5.47(4)	5.55(4)	5.75(3)	5.80(5)	5.94(3)
σ	0.65(1)	0.22(3)	0.23(3)	0.19(3)	0.17(4)	0.16(3)

Table 4.3: Fitted parameters for BN samples using a single-phase RS approach incorporating stacking disorder]

4.4 Nanostructure: virtual specimens

The information in Table 4.3 gives only a partial picture of each sample. The layer lattice parameter a_l gives a picture of atomic scale structure, while μ and σ completely define the domain size distribution, or the

microstructure of each sample. The layer correlation probabilities α_{ff} and α_{bf} help to describe the nanoscale structure.

More interesting however is the full picture of how these different structure scales interact. To investigate this, a virtual specimen can be created, following a process similar to that in Section 3.1.2, or proposed but not studied already in the literature [152]. This is done simply by stochastically sampling the characteristics of each sample to build individual domains, and then analyzing the structure of these domains.

For example, to create one domain of a given sample, first the log-normal distribution refined from the powder diffraction data of the sample is sampled to establish the domain size. Following this, a Markov chain is generated by sampling the finite state machine created from the refined transition probabilities of the sample. The length of this Markov chain is determined by the refined layer unit cell thickness and the sampled domain size. The Markov state sequence represents the sequence of layers in the domain. For example, a domain can be represented by a Markov state sequence such as

$$fffffffbfffffffffffffffffbbbbbfffff, \tag{4.3}$$

representing a series of forward f and backward b transitions.

When a domain is constructed in such a way, bands can be observed within the domain showing *local* symmetry of either of the two sp^3-bonded polytypes mentioned earlier (Figures 4.1a and 4.1b). Three types of bands can be uniquely identified in such a domain, based on these two polytypes: c-BN, w-BN, and tc-BN (twinned cubic-BN). The local structure of any given layer is determined by the relative position of the pre- and proceeding layers, and correspond to the layer sequences as follows

$$\begin{aligned} \ldots ff \ldots &\rightarrow \text{c-BN} \\ \ldots fb \ldots &\rightarrow \text{w-BN} \\ \ldots bf \ldots &\rightarrow \text{w-BN} \\ \ldots bb \ldots &\rightarrow \text{tc-BN} \end{aligned} \tag{4.4}$$

It is important to note that the distinction between c-BN and tc-BN is only meaningful when both structures exist coherently within a single domain, as the two are related by reflection on the cubic (111)

plane. This distinction can be useful to identify preferential growth of relatively twinned bands with respect to non-twinned bands within individual domains.

With this, the individual layers in Markov state sequence in equation 4.3 can be assigned local symmetries

$$fffffffbffffffffffffffffbbbbffff \tag{4.5}$$

All nanostructural information can be retrieved from a domain represented by a Markov sequence such as that in equations 4.3 and 4.5: this specific sequence can be described as 7.1 nm domain, containing 34 atomic layers and 7 total polytype bands: a c-BN band of 8 layers (1.7 nm), a w-BN of 2 layers (0.4 nm), a c-BN of 15 layers (3.1 nm), a w-BN of 1 layer (0.2 nm), a tc-BN of 4 layers (0.8 nm), a w-BN of 1 layer (0.2 nm), and a c-BN of 3 layers (0.6 nm). It is not necessary to explicitly

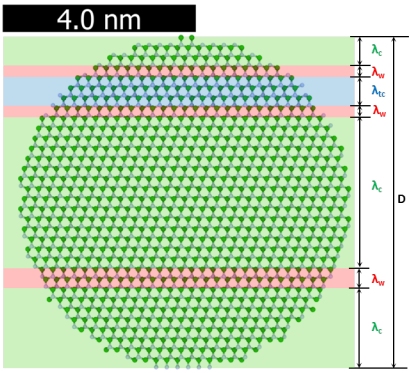

Figure 4.5: An atomistic BN domain corresponding to the Markov sequence in equation 4.3. Locally c-BN, tc-BN, or w-BN are colored green, blue, or red, respectively.

define atomic positions to retrieve this nanostructural information, as all atomic positions are implicit based on the Markov sequence, the relative positions of the atomic layers as defined by the Markov process, and the assumed domain morphology. By avoiding the specification of atomic positions, considerable computational resources can be spared, both in processing and storage. That being said, it can at times be

helpful to view an atomistic representation a Markov sequence. Figure 4.5 shows such an atomistic representation of the Markov sequence presented in equation 4.3, with band structures colored according to local symmetry, and band sizes denoted by λ_x, where $x =$ c, tc, or w.

Such a domain however represents only one configuration within a powder or polycrystalline sample that is composed of a huge number of domains. By repeating this stochastic domain creation process many times, statistical distributions can be built that completely describe the nanostructure of the sample. Examples of such distributions for sample 1 are shown in Figure 4.6.

The first row of Figure 4.6 gives information on the domains in the sample. Figure 4.6a shows the probability of choosing a domain from the sample with only one local symmetry (with no stacking disorder). In this case, there is no distinction between the tc-BN and c-BN structures. Figure 4.6b is similar, but gives the joint probability of choosing a domain from the sample with only one local symmetry and a specific size.

The second row of Figure 4.6 gives information on the bands in the sample. Figure 4.6c presents the probability of choosing a single band from any domain in the sample and finding it with a specific local symmetry. Figure 4.6d gives the joint probability of choosing a single band and finding it with both a given local symmetry and thickness. Figure 4.6e gives similar information, showing the joint probability of choosing a single band and finding it both with a given local symmetry and inside a domain of a given size.

The final row of Figure 4.6 provides information on the individual atomic layers in the sample. Figure 4.6f gives the overall probability of choosing a single layer with a given local symmetry. Figure 4.6g gives the joint probability of choosing a single layer in the sample and finding it within a band both of a given local symmetry and thickness. Figure 4.6e gives similar information, showing the joint probability of choosing a single atomic layer and finding it with a given local symmetry inside a domain of a given size.

Together these distributions give a complete set of information regarding the nanostructure of the virtual sample, as derived from the fit assuming a single phase with stacking disorder.

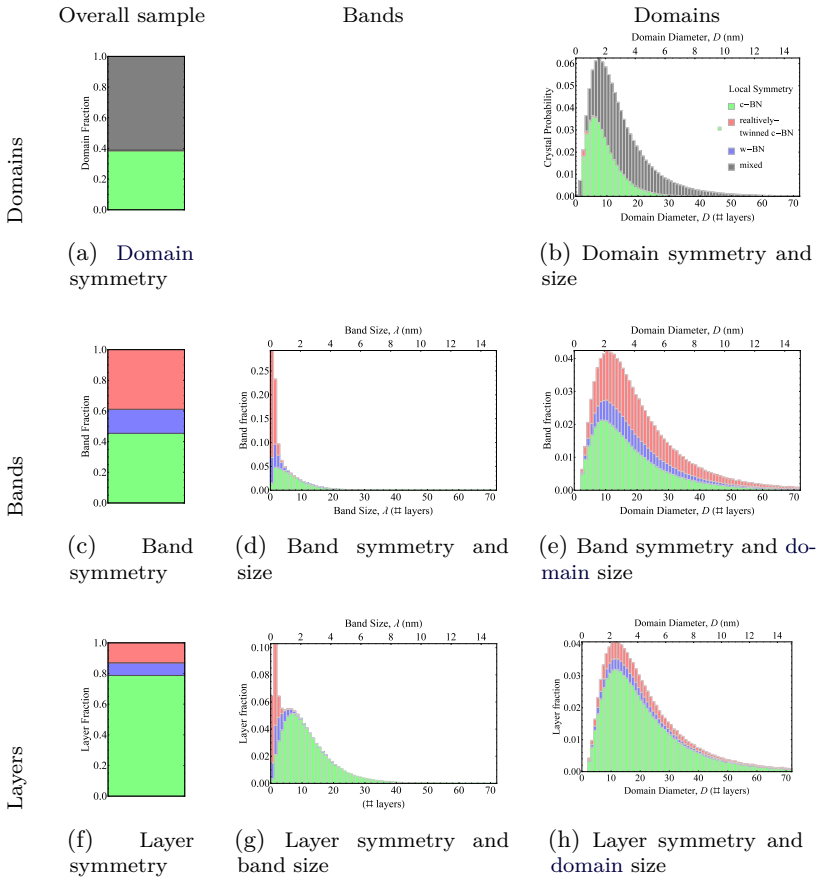

(a) Domain symmetry

(b) Domain symmetry and size

(c) Band symmetry

(d) Band symmetry and size

(e) Band symmetry and domain size

(f) Layer symmetry

(g) Layer symmetry and band size

(h) Layer symmetry and domain size

Figure 4.6: Probability distributions describing the nanostructure of sample 1, derived from random sampling of refined stochastic process

4.5 Discussion

4.5.1 Model accuracy

The two different models provide two very distinct pictures of the samples. By employing a two-phase RS model, assuming empirical profile shapes constrained by Bragg's law and a traditional structure factor, the hypothesis is that each sample is a sintered mixture of purely c-BN and w-BN domains, where each shows near perfect three-dimensional periodicity. By applying the new RS model proposed in Section 2.6.3, the hypothesis is that each sample is a sintered body of BN domains, where each domain is characterized by one-dimensional disorder and built of coherently stacked bands that show a local symmetry of either the c-BN or w-BN polytype.

Comparing the results obtained in terms of both the agreement with experimental data and the reliability of the extracted sample characteristics can help establish exactly which picture of the samples is more likely. If just the goodness-of-fit index is used to compare the models, one might be inclined to declare the two-phase hypothesis as more likely: with the exception of sample 1, all two-phase fits show a lower goodness-of-fit, indicating a higher level of fit agreement.

This however is a good example of where a bit of common sense can go a long way. For each sample, the w-BN phase parameters fit to unphysical values with large estimated uncertainties. The w-BN lattice parameter c_w shows a relative standard uncertainty of about 0.5%, much higher than what is typically expected for a lattice parameter. Further, c_w deviates from the experimentally reported value of 4.17 Å[147, 148] by as much as 4% in some samples. A similar problem is found for the a_w w-BN lattice parameter. Worse still are the implausibly large average microstrain and small average domain size of the w-BN phase, retrieved for each sample. The relative standard uncertainties obtained on both these characteristics are in some cases greater than 100%.

In general these issues are a clear indication that a two-phase model is not appropriate, suggesting that the samples are not sintered mixtures of nanocrystalline c-BN and w-BN. The alternative hypothesis is that the samples are sintered bodies of nanocrystalline BN domains, where each domain is characterized by one-dimensional disorder and

built of coherently stacked bands that show a local symmetry of either the c-BN or w-BN polytype. As mentioned earlier, generally the goodness-of-fit numbers indicate that the fits associated with such a model are lower quality. However, the difference in the goodness-of-fit between the two models is not particularly large, and the single-phase model is significantly simpler, requiring only 11 parameters compared to the 41 parameters employed in the two-phase model. Further, the fitted parameters within the single-phase model correspond directly to physical characteristics of the sample, are more physically reasonable, and are generally retrieved with lower standard uncertainties. Finally, the hypotheses of one-dimensional disorder is supported directly by electron microscopy observations. All of these pieces together strongly suggest that the single-phase hypothesis is morel likely.

It is worth pointing out that the one-dimensionally disordered single-phase hypothesis was already proposed in an incomplete form by Tian *et al.* These researchers neglected to suppose the existence of bands showing a w-BN local symmetry within the domains, instead supposing only the existence of nanotwins [125]. Nanotwinned bands however necessitate the presence of w-BN bands, as a $(111)_c$ twin-boundary in BN *always* shows the local symmetry of the w-BN polytype (see e.g. Figure 4.5). The existence of larger w-BN bands in the samples of Tian *et al.* was pointed out by Dubrovinskaia and Dubrovinsky [126], who had previously synthesized apparently similar samples [143]. However, in their original work, Dubrovinskaia *et al.* explicitly *ruled out* the possibility of stacking disorder, instead proposing that the samples were sintered nanocomposites [143].

4.5.2 Effect of processing temperature

Having established a likely nanostructural model, as well as a method for extracting a full nanostructural picture, it is possible to explore the effect of HPHT synthesis temperature on sample atomic, nano, and microstructure. Repeating the stochastic sample creation process outlined in Section 4.4 for each sample gives distributions like those presented in Figure 4.6 for each sample. Analysis of these distributions gives all information on the virtual sample nanostructure, linked to the real sample through the powder diffraction data fitting.

The lattice parameter, directly refined as part of the fit for each

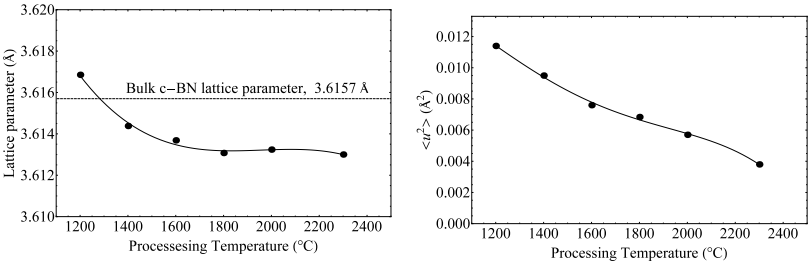

(a) Equivalent c-BN lattice parameter

(b) Debeye-Waller mean squared displacement

Figure 4.7: Atomic scale structure of the BN samples as extracted from powder diffraction data fitting, plotted vs. synthesis temperature

dataset, is plotted in Figure 4.7a against synthesis temperature. As synthesis temperature increases, the lattice parameter tends to decrease, with the largest drop seen between the samples prepared at 1200°C and 1400°C. Above a synthesis temperature of 1800°C, the lattice parameter is stable at round 3.6131 Å. The significant deviation in lattice parameter at low synthesis temperature is likely due to the very small average domain size of about 10 nm. Smaller domains show a larger volume fraction of under-coordinated surface species, which can relax and show a lattice parameter significantly different from that of the bulk material [97–100]. The tendency to converge to a lattice parameter slightly smaller than the measured bulk value of c-BN ($a_c = 3.615$ Å) can be explained by the presence of w-BN bands within the domains. The B-N bond length in the ideal w-BN polytype is 1.56179 Å, smaller than that in ideal c-BN (1.56534 Å), thus it is possible that the w-BN bands are slightly more dense than their c-BN counterparts, and that their presence leads to a small decrease in the lattice parameter.

Figure 4.7b shows a plot of the directly refined isotropic mean squared thermal displacement, $\langle u^2 \rangle$. With increasing synthesis temperature, $\langle u^2 \rangle$ decreases nearly linearly, suggesting that thermal vibrations decrease in magnitude with increasing synthesis temperature. An apparent decrease in vibrational magnitude is consistent with a more ordered

structure [105, 153].

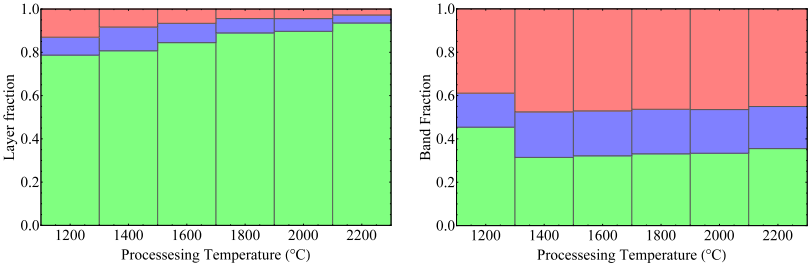

(a) layers (b) bands

Figure 4.8: Probability of finding a layer or band of a certain polytype symmetry within each BN sample

The probability of choosing a layer of a given local symmetry is shown in Figure 4.8a. As each layer effectively represents a uniform slice of the domain, the layer probability effectively represents a volume fraction or percent. Figure 4.8a then suggests that the c-BN volume percent increases from 79% at a synthesis temperature of 1200°C to 94% at a synthesis temperature of 2300°C. This increase in c-BN comes at the expense of both w-BN and tc-BN type layers: the volume percent of both decreases with increasing synthesis temperature.

The probability of a band showing a specific polytype vs synthesis temperature is shown in Figure 4.8b. There is an an initial increase in the pervasiveness of w-BN and tc-BN type bands from a synthesis temperature of 1200°C to 1400°C, coming at the expense of c-BN type bands. This trend is reversed above synthesis temperatures of 1200°C, where a very slight increase is seen in the fraction c-BN type bands at the expense of w-BN type bands, with little to no change seen in the frequency of tc-BN type bands. Generally, Figure 4.8 would suggest that while the overall volume fractions associated with each layer local symmetry change significantly with synthesis temperature, the frequency of each type of band remains relatively static.

Figure 4.8 gives information only about the *relative frequency* of bands or layers showing a specific local symmetry. Another important aspect is the average thickness $\langle\lambda\rangle$ of these bands (see Figure 4.5 for

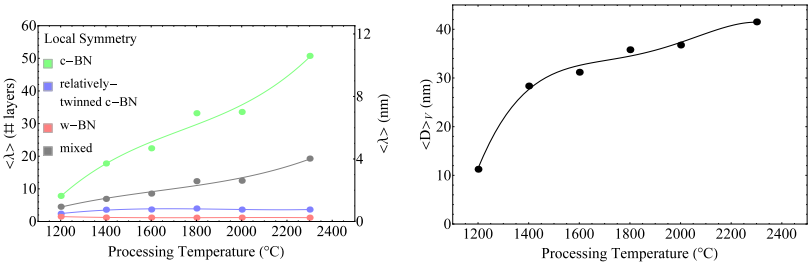

(a) Average band size

(b) Volume-average domain size

Figure 4.9: Nano and microstructure of the BN samples as extracted from powder diffraction data fitting, plotted as a function of synthesis temperature

a schematic depiction). By taking a numerical average of distributions like the one shown in Figure 4.6d for each sample, the average band thickness can be determined, both with and without regard to local symmetry. A plot of this information vs synthesis temperature is shown in Figure 4.9a. Initially, from a synthesis temperature of 1200°C to 1400°C there is a very small change in the average thickness of bands showing either a w-BN or tc-BN local symmetry. Again above a synthesis temperature of 1400°C locally w-BN or tc-BN bands remain relatively static at average thicknesses of about 1.2 or 3.6 atomic layers (0.77 nm or 1.2 nm), respectively.

Conversely, Figure 4.9a clearly shows that average thickness of bands with a c-BN local symmetry increases nearly linearly with increasing synthesis temperature, from 7.8 atomic layers (1.6 nm) at 1200°C to 51 layers (11 nm) at 2300°C. The same is true if the local symmetry of the band is neglected: in general as synthesis temperature increases each domain is on average composed of thicker bands showing one consistent polytype symmetry throughout. This indicates that the nanostructure becomes more ordered with increasing synthesis temperature, consistent with the results obtained regarding thermal vibrations.

Shown in Figure 4.9b is the volume-weighted mean domain size $\langle D \rangle_V$ plotted against synthesis temperature. There is a large increase in $\langle D \rangle_V$ from 11.3 nm at 1200°C to 28.4 nm at 1400°C. Above 1400°C the increase in $\langle D \rangle_V$ is essentially linear with synthesis temperature, with a final volume-weighted mean domain size of 41.5 nm at 2300°C.

With this complete set of information it is possible to hypothesize how the BN phase transformation proceeds with increasing temperature at 15 GPa. Initially at 1200°C, very disordered, small domains exist, containing up to 15% w-BN type layers by volume, dispersed into w-BN type bands that are on average just one layer thick. These w-BN type bands act as twin boundaries between c-BN and relatively twinned c-BN type bands, where one of the two is on average much smaller. With a small increase in synthesis temperature to 1400°C, the average domain size more than doubles, with a marked decrease in the volume fraction of w-BN type layers, in favor of c-BN type layers. The growth of c-BN type bands is favored, while relatively twinned c-BN and w-BN type bands remain on average about the same size. These trends (consumption of w-BN type layers, growth of c-BN type bands, domain growth) continues with further increases in synthesis temperature above 1400°C. Even at synthesis temperatures as high as 2300°C however, stacking disorder still exists, although it is much less frequent.

Some authors have suggested that the samples investigated contain large regions of w-BN type structure [126], similar to previously reported aggregated BN nanocomposites [143]. In general however, none of the virtual samples show a significant quantity of w-BN type bands that are greater in thickness than 1 atomic scale layer. In fact, it is clear from Figure 4.9a that in all samples, regardless of synthesis temperature, the average w-BN band thickness is less than 1.2 atomic layers. With this information it is possible to state that the primary manifestation of disorder is the presence of twin boundaries, at least in the case of these specific BN samples [125]. This goes beyond the simple model that these BN samples are characterized by stacking disorder, proposed by Koch and Leoni [145].

4.6 Concluding remarks

Disagreement exists in the literature regarding the crystalline identity of nanostructured BN samples, with some proposing they are sintered mixtures of the two sp^3-bonded polytypes ("aggregated nanocomposites") [126, 143], and others suggesting that samples are "nanostructured" [144], "disordered" [145], or "nanotwinned" [125, 149] single-

phase BN. By applying two different models for powder diffraction data fitting, it was possible to test each of these nanostructural models. This study suggests that HPHT treatment of turbostratic sp^2-bonded BN at 15 GPa, between 1200°C and 2300°C, does not result in two-phase samples but rather a single BN phase with stacking disorder, and that the primary manifestation of this stacking disorder is the presence of nanotwins, as originally proposed [125].

Using a Markov chain model, it is possible to imagine the existence of similar BN samples characterized by different nanostructures. In fact, the possible permutations of domain size, Reichweite number, and layer-layer correlation probabilities implies that a vast array of nanostructured BN samples could exist. This potential for diversity is a possible explanation for the significant disagreement in the literature: small variations in initial precursors or synthesis parameters (temperature, pressure, dwell time, ramp rate, etc.) could cause significant fluctuations in the sample in terms of one-dimensional disorder, domain morphology and even atomic structure. These changes manifest as inexplicable features in the powder diffraction pattern, and often prevent any sort of quantitative analysis.

As a practical example, the work of Dubrovinskaia *et al.* can be considered. Unlike Tian *et al.*, who employed BN "nano-onions" precursors (nested fullerene-like structure) [125], Dubrovinskaia *et al.* subjected simple pyrolytic graphite-like BN to HPHT treatments. They concluded that reflection broadening within the powder diffraction data was entirely due to crystallite size, and thus ruled out the presence of structural defects (stacking disorder) [143]. However, the powder diffraction data of some samples (e.g. their Figure 2c, synthesized at 1600°C and 18 GPa) clearly show features from both c-BN and w-BN phases. With this qualitative evidence, Dubrovinskaia *et al.* concluded that their samples were aggregated nanocomposites [143].

However, by applying the Markov chain models adopted here, powder diffraction data which looks remarkably similar to that reported in Figure 2c of [143] can be simulated. Such a simulation, done by assuming instrumental conditions identical to those used by Dubrovinskaia *et al.*, is reported in Figure 4.10a. Shown in Figures 4.10b, 4.10c, and 4.10d are respectively the domain size distribution, the fraction of different layer types, and the fraction of different band types asso-

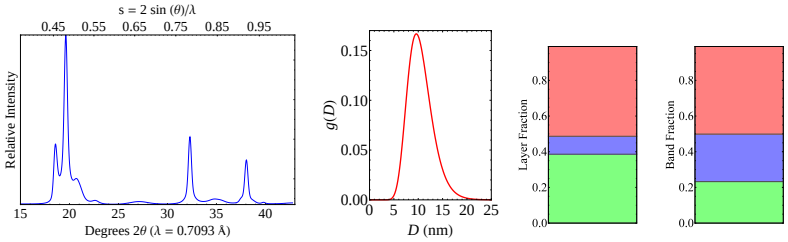

(a) diffraction data (b) domain size (c) layers (d) bands

Figure 4.10: Powder diffraction data with nano and microstructure information for a hypothetical sample, possibly similar to that prepared at 1600°C and 18 GPa by Dubrovinskaia *et al.* [143].

ciated with the powder diffraction data in Figure 4.10a. Compared to the samples investigated here, the hypothetical sample of focus in Figure 4.10 is characterized by a much large fraction of w-BN type layers (51%) and bands (50%). Further, the w-BN type bands are on average much larger ($\langle \lambda_w \rangle$ = 3.9 atomic layers = 1.4 nm), indicating the stacking disorder in such a sample cannot be said to manifest as "nanotwins". Granted, without analysis of the actual powder diffraction data following a process similar to the one outlined here, it cannot be concluded definitively that the sample reported by Dubrovinskaia *et al.* is in fact characterized by stacking disorder. However the visual similarity between the simulated and measured powder patterns, and the presence of "banding" within individual domains of their samples, evidenced by electron microscopy [143], suggest that stacking disorder is highly likely.

Describing a sample characterized by stacking disorder as an aggregated nanocomposite is partially appropriate, as disordered samples do show local regions with structure similar to c-BN and w-BN (see e.g. Figure 4.5). Strictly speaking, a two-phase composite specimen should show disordered boundaries between domains of different polytypes, while specimens characterized by stacking disorder show very specific *coherent* boundaries. One would expect that from a mechanical point of view the properties would be distinct.

Thus, not only was a probable nanostructural model suggested and

supported, this nanostructural model can facilitate speculation on the identity of apparently diverse samples prepared under similar synthesis conditions. Beyond this, by applying the approach outlined here, it should be possible to correlate nanostructural information with both properties and synthesis conditions in order to better understand the physical mechanisms underlying the improved performance of nanostructured BN and ultimately engineer further improvements.

Chapter 5

Conclusions

5.1 Summary

The primary aim of this work was reviewing, expanding upon, testing, and utilizing RS models of diffraction. In Chapter 2, RS models were reviewed, moving from strict assumptions of spatial unboundedness and three-dimensional periodicity to more relaxed assumptions of partial periodicity and finite crystals. Throughout the chapter, concepts were illustrated practically through examples of metallic nickel. New expressions were presented and a new approach was shown for approximating the diffraction effect of finite crystal size for a powder ensemble of one-dimensionally disordered crystals. A generalized shape function approach was demonstrated for the first time for the case of a spatially finite one-dimensionally disordered average crystal, without introducing any new definition to the layer electron density. It was explicitly pointed out that care must be taken in choosing models: there is a trade off between computational expense, accuracy, and physicality. It is essential that the limitations (assumptions) of the models are kept in mind when adopting any specific approach.

In Chapter 3, RS models were tested on synthetic powder diffraction data computed by applying the DSE to several atomistic powder specimens. A process for creating atomistic powder ensembles was outlined, and a novel method was proposed for accurately approximating the ensemble-averaged powder diffraction pattern. The minimum library size was determined and compared for each ensemble

considered, and it was found that libraries of less than 620 domains were generally sufficient to approximate the ensemble average. The ensemble-averaged powder diffraction data was fit where possible using several different models, and it was found that only the new model for finite, linearly disordered-crystals was successful both at reproducing the powder diffraction data and accurately retrieving the physical characteristics of the samples. It was seen that while a failure to satisfy model assumptions does not necessarily imply that the data fitting fails, it can necessitate that the fitted parameters do not reflect the true characteristics of the sample.

In Chapter 4, different RS models were utilizing to fit powder diffraction data from nanostructured BN samples to establish the most likely nanostructure. It was found that models incorporating the powder diffraction effects of stacking disorder and finite crystal size, while not significantly improving the agreement with the observed diffraction data, yielded more accurate and precise refined parameters, and were in better agreement with electron microscopy studies when compared to models assuming a sintered mixture of two nanocrystalline phases. With this result, it was possible to conclude that the most likely nanostructural model is that of sintered bodies composed of a single one-dimensionally disordered nanocrsytalline phase, rather than a two-phase or nanocomposite sintered body. Beyond this, by constructing simulated nanostructures through stochastically sampling refined sample characteristics, it was possible to further conclude that in the samples investigated, the primary manifestation of one-dimensional disorder was the presence of twin boundaries, leading to nanometer scale twin bands or "nanotwins" as proposed by those who synthesized the samples, and ruling out the presence of significantly large bands showing a w-BN-like structure.

5.2 Future perspectives

Nanomaterials showing one dimensional disorder are pervasive. Considering only materials isostructural with the simple close packed polytypes discussed in this thesis already provides a huge list of possibilities. Many metals show a significantly decreased stacking fault energy when alloyed [154], or even meta-stable polytypes when samples

are nanocrsytalline [155–157]. This stacking disorder or polytype interlayering has been linked to material performance in a number of nanocrystalline metal systems [155–159].

Most II-IV semicondoctors such as ZnO, ZnS, ZnSe, ZnTe, CdS, CdSe, and CdTe, adopt structures similar to the cubic zincblende and hexagonal wurtzite structures (isostructural with c- and w-BN), and tend to show polytype interlayering and/or the presence of stacking faults [105, 160–169]. In a number of cases, this nanostructuring has been shown to influence electronic properties [161, 167].

Going beyond the polytypes considered in this work, mixed layer minerals with both cationic [14, 170–172] and anionic [173–175] rigid layers also show stacking disorder, although the nature of the bonding often dictates that layer-layer translations are significantly less well-defined than the examples considered here. These materials show promise as specialized drug carriers [176–178], for environmental remediation [179], and catalysis [180, 181].

It should be clear then that the modeling approaches outlined in this thesis have a role to play within materials science, as effective characterization acts to connect structure, properties, processing, and performance. In the face of the the "nanostructure problem" [15] associated with stacking disorder, outlined briefly in Chapter 1 and highlighted further throughout this work, *traditional* diffraction techniques can be ineffective. The new models outlined here offer an improvement, and could in some cases represent a bridge to the atomic scale detail offered by the more computational expensive DS approach embodied by the DSE.

Specifically, the RS modeling approaches reviewed and expanded upon in Chapter 2 can be useful for providing a coarse understanding of the average atomic, nano, and micro structure of a powder sample. These approaches are however intrinsically limited by their intrinsic assumptions, especially that sample related parameters are uncorrelated. In reality, lattice parameters and faulting rate are influenced by crystal size, and may not be uniform within a crystal. The values retrieved by RS modeling approaches likely then represent mean or effective values.

Correlation of atomic, nano, and micro structure can be modeled easily using the DSE, but good starting models are necessary to make the analysis computationally tractable. Thus RS and DS models can be

seen as complementary; the former can provide a reasonable starting point for the latter, saving computational resources, while the latter is more flexible, but computationally expensive. Molecular dynamics could also be used as an intermediate treatment, transforming initial idealized atomistic powder ensembles into more physically reasonable ensembles. Ultimately, the goal would be to apply as many characterization techniques as possible simultaneously to refine a globally consistent model for the sample across vast length scales, from atomic to macroscopic.

Acknowledgments

My sincerest gratitude goes to my family, for always encouraging and supporting me through what I'm sure has seemed like an unending formal education. Special thanks go to my parents for tolerating my tendency to question every word out of their mouths, to my Aunt Lori for more than I could list here, and my Uncle Bob for taking interest in the obscurities I have chosen to specialize in.

I am extremely grateful to Dr. Scott Misture at Alfred University, who gave me my first position as an undergraduate researcher, and sparked my interest in scientific pursuits. I would like to thank Dr. Kirill Yusenko for always keeping me grounded in reality with a steady stream of interesting diffraction data from real (not virtual) specimens. Similar thanks also go to Dr. Lars Lundegaard and Dr. Christoffer Tyrsted, also for insightful and critical feedback.

I cannot omit the contribution of my friends and colleagues both at the University of Trento and abroad, who have provided me an overabundance of support (of all kinds), especially in the latter half of my degree. To Pete, Luca, Cristy, Dmitry, Alberto, Bochra, and Camilo, I can honestly say that my time here in Trento would not have been the same without you all.

Finally, it is important to acknowledge the role my academic tutor, Prof. Matteo Leoni, who has taught me many things, including the importance of hard work, academic and professional integrity, honesty in all things, and most importantly, teamwork. It is fair to say that without him, I would not be in the position I am now.

Some of the research presented here was partially funded as part of the Futuro in Ricerca RBFR10CWDA project from the Italian Ministry of Education.

Appendix A

DISCUS Synthesis Script

Below is an example script provided to the DISCUS software package (v3.6.2) [130] for creating a virtual powder specimen. It is intended to be used with a layer input file, included in the same directory, and named "l1.cll." The contents of "l1.cll" are included after the script.

```
1  set prompt, off, file
2
3  #
4  #declare variables
5  #
6  variable integer, start
7  variable integer, stop
8  variable integer, current
9  variable real, diameter
10 variable real, shift1
11 variable real, shift2
12 variable real, shift3
13 variable real, mu
14 variable real, median
15 variable real, prob
16 variable real, prob2
17 variable real, prob3
18 variable real, prob4
19 variable real, sigma
20 variable integer, width
21 variable integer, height
22
23 #naming conventions, number of domains to be created (here 10)
24 start = 1
25 stop = 10
26
```

```
27  #parameters for generating an ensemble, should be chosen by
        user
28  #log-normal mean of log-normal distribution describing domain
        diameters (in Angstroms)
29  mu = 4.5
30
31  #log-normal standard deviation of log-normal distribution
        describing domain diameters (in Angstroms)
32  sigma = 0.18
33
34  #median of log-normal distribution describing domain diameters
        (in Angstroms)
35  median = exp(mu)
36
37  #probability of a forward transition given two previous forward
         transitions (alphafff)
38  prob = 0.91
39
40  #probability of a forward transition given a previous forward
        transition and a previous previous backward transition (
        alphabff)
41  prob2 = 0.80
42
43  #probability of a forward transition given a previous backward
        transition and a previous previous forward transition (
        alphafbf)
44  prob3 = 0.25
45
46  #probability of a forward transition given two previous
        backward transitions (alphabbf)
47  prob4 = 0.12
48
49
50  #loop to create multiple domains
51  do i[1] = start,stop
52
53    #sample distribution to get diameter
54    diameter = logn(median, sigma)
55
56    #if the diameter is less than 3.2 Angstroms we throw it away
          (this is not an objective cut-off...)
57    if(diameter .lt. 0.32) then
58      i[1] = i[1] - 1
59    else
60      #store the variables
61      current = i[1]
62      #define  the layer cell
```

```
63          read
64                  cell l1.cll
65      #calculate the minimum number of unit cells based on the
            unit cell dimension and the target diameter
66      width = 1.6 *(int(diameter/lat[1])) + 4
67      height = (int(diameter/lat[3])) + 5
68
69      #compute a random shift (this is to be completely correct
            when using the shape function apporach)
70      shift1 = (lat[1] * ran(0.))
71      shift2 = (lat[2] * ran(0.) )
72      shift3 = (height/2.0 +(lat[3]/2 * ran(0.) ))
73
74      #load the cell with the correct dimensions and dump it to a
             temp file
75      read
76        cell l1.cll,width,width,1
77      save dummy.1.struc
78
79      #enter the stack subroutine area
80      stack
81        #
82        # Now we specify the structure files to be used for the
83        # four layers. each layer is identical except for it's
              stacking
84        #
85        layer dummy.1.struc
86        layer dummy.1.struc
87        layer dummy.1.struc
88        layer dummy.1.struc
89        #
90        # number of layers in the stack
91        #
92        number height
93        #
94        # transition vectors.  This is for R=3 so we have some
              forbidden transitions
95        #
96            #Forward
97        trans 1,1, 1.0/3.0,-1.0/3.0,1.0
98
99            #Forbidden
100       trans 1,2, 0,0,1.0
101
102           #Backward
103       trans 1,3, -1.0/3.0,1.0/3.0,1.0
104
```

```
105             #Forbidden
106         trans 1,4, 0,0,1.0
107
108             #Forward
109         trans 2,1, 1.0/3.0,-1.0/3.0,1.0
110
111             #Forbidden
112         trans 2,2, 0,0,1.0
113
114             #Backward
115         trans 2,3, -1.0/3.0,1.0/3.0,1.0
116
117             #Forbidden
118         trans 2,4, 0,0,1.0
119
120             #Forbidden
121         trans 3,1, 0,0,1.0
122
123             #Forward
124         trans 3,2, 1.0/3.0,-1.0/3.0,1.0
125
126             #Forbidden
127         trans 3,3, 0,0,1.0
128
129             #Backward
130         trans 3,4, -1.0/3.0,1.0/3.0,1.0
131
132             #Forbidden
133         trans 4,1, 0,0,1.0
134
135             #Forward
136         trans 4,2, 1.0/3.0,-1.0/3.0,1.0
137
138             #Forbidden
139         trans 4,3, 0,0,1.0
140
141             #Backward
142         trans 4,4, -1.0/3.0,1.0/3.0,1.0
143
144         #
145         #probabilities.  This is for R=2 so we have some
                forbidden transitions
146         #
147         crow 1,prob,0,1.0-prob,0
148         crow 2,prob2,0,1.0-prob2,0
149         crow 3,0,prob3,0,1.0-prob3
150         crow 4,0,prob4,0,1.0-prob4
```

```
151         #
152         # no idea what this does but I guess it has to do with
                how Discus builds the stacks in x and y...
153         #
154         aver  0.0, 0.0, 1.0
155         modul 1.00, 0.00, 0.00, 0.00, 1.00, 0.00
156         set modulus,on
157         set trans, fixed
158
159         create
160         run
161       exit
162       #
163       # do the shifting
164       #
165       symm
166         uvw   0,0,1
167         orig  0.0, 0.0, 0.0,crystal
168         trans shift1,shift2,(-1.0*(shift3))
169         angle 0.0
170         type  proper
171         mode  repl
172         power 1
173         sel   all
174         incl  all
175         show
176         run
177       exit
178       #
179       # cut our sphere
180       #
181       boundary sphere, diameter/2
182       purge
183       #
184       # output the crystal in an xyz format
185       #
186       plot
187         prog diamond
188         outfile "./domain.diameter.%f.iter.%d.xyz",diameter,
                current
189         type crystal
190         ext all
191         sel all
192         dese void
193         col xyz
194         show
195         run
```

```
196       exit
197     endif
198   enddo
199
200
201   exit
```

layer input file contents, “l1.cll”:

```
1   title 1 layer, Ni
2   #layer group symmetry
3   spcgr P6
4   #layer unit cell the cubic lattice parameter (a_c) is
        transformed  here to a hexagonal equivalent
5   # a_h = b_h = sqrt(2)*a_c/2 , c_h  = sqrt(3) * a_c/3
6   #ac= 3.52
7   cell  2.4890   2.4890  2.0323   90.00   90.00   120.00
8   atoms
9   Ni    0.000   0.000   0.000   0.100
```

Abbreviations

Acronyms

FP	fundamental parameters
FWHM	full width at half maximum
CSD	coherently scattering domain
FT	Fourier transform
WPPM	whole powder pattern modelling
DSE	Debye scattering equation
BN	boron nitride
DS	direct-space
RS	reciprocal-space
LPA	line-profile analysis
fcc	face-centered cubic
hcp	hexagonal close packed
CVF	common volume function
MCL	mean column length
SEM	scanning electron microscopy
TEM	transmission electron microscopy
WAXS	wide-angle X-ray scattering
SAXS	small-angle X-ray scattering
HPHT	high-pressure high-temperature

Symbols

β	Integral breadth of a line profile. The integrated area of the profile divided by the profile maximum
$\mathbf{a}$	DS lattice vector, $\parallel$ to $\hat{\mathbf{x}}$
$\mathbf{b}$	DS lattice vector, in the plane spanned by $\hat{\mathbf{x}}$ and $\hat{\mathbf{y}}$
$\mathbf{c}$	DS lattice vector
$\mathbf{R}_{ij}$	Stacking vector spatially relating layer types i and j when adjacent in a crystal with stacking disorder
$\hat{\mathbf{v}}$	unit vector, $\mathbf{v}/\left\|\mathbf{v}\right\|$
λ	wavelength
$\mathbf{r}$	position vector
θ	half of the scattering angle
$\mathbf{s}$	scattering vector
s	scattering vector magnitude
e	elementary charge, $1.602176565\,(35) \times 10^{-19}$C
m_e	rest mass of an electron, $9.10938215\,(45) \times 10^{-18}$g
c	speed of light in a vacuum, 2.99792458×10^{8} m/s
$U\left(\mathbf{r}\right)$	electron density from an isolated atom
$\mathbf{V}$	volume

$\cdot$	scalar product
$\imath$	imaginary unit, $\sqrt{-1}$
$\varphi(\mathbf{s})$	Scattered wave amplitude
$\mathcal{F}$	Fourier transform operator
$f(\mathbf{s}, \hbar\omega)$	atomic form factor
$\hbar$	reduced Planck constant[†], $6.58211928\,(15) \times 10^{-16}$eV·s
$\delta(\mathbf{r})$	Dirac delta distribution
$*$	convolution operation
$z(\mathbf{r})$	DS lattice function
$\rho(\mathbf{r})$	electron density from a collection of atoms
$F(s)$	structure factor
$I(\mathbf{s})$	intensity distribution
$Z(\mathbf{s})$	RS lattice function
h	Miller index associated with $\mathbf{a}^*$ direction in RS
k	Miller index associated with $\mathbf{b}^*$ direction in RS
l	Miller index associated with $\mathbf{c}^*$ direction in RS
$\mathbf{a}^*$	RS lattice vector, $\parallel$ to $\mathbf{b} \times \mathbf{c}$
$\mathbf{b}^*$	RS lattice vector, $\parallel$ to $\mathbf{c} \times \mathbf{a}$
$\mathbf{c}^*$	RS lattice vector, $\parallel$ to $\mathbf{a} \times \mathbf{b}$
$\times$	cross product
$\sigma(\mathbf{r})$	Shape function describing a crystal volume
$S(\mathbf{s})$	FT of the crystal shape function, $\mathcal{F}[\sigma(\mathbf{r})]$

[†]Datum taken from [184]

$A(\mathbf{L})$ Autocorrelation function of the shape function

M Number of layer types in the Markov process describing a crystal with stacking disorder

N Total number of layers in a crystal

α_{ij} Transition probability from Markov state (layer type) i to j in the Markov process describing a crystal with stacking disorder

R Reichweite number of the stacking process

Bibliography

[1] J.T. Bagnara, P.J. Fernandez, and R. Fujii. "On the blue coloration of vertebrates". *Pigment Cell Res.* **20** (2007), pp. 14–26. DOI: 10.1111/j.1600-0749.2006.00360.x.

[2] W.C. Röntgen. "On a new kind of rays". *Science* **3** (1896), pp. 227–231. DOI: 10.1126/science.3.59.227.

[3] W. Friedrich, P. Knipping, and M. Laue. "Interferenzerscheinungen bei Röntgenstrahlen". *Ann. Phys.* **346** (1913), pp. 971–988. DOI: 10.1002/andp.19133461004.

[4] M. von Laue. "Eine quantitative Prüfung der Theorie für die Interferenzerscheinungen bei Röntgenstrahlen". *Ann. Phys.* **346** (1913), pp. 989–1002. DOI: 10.1002/andp.19133461005.

[5] W.H. Bragg and W.L. Bragg. "The Reflection of X-rays by Crystals". *Proc. R. Soc. A Math. Phys. Eng. Sci.* **88** (1913), pp. 428–438. DOI: 10.1098/rspa.1913.0040.

[6] G.S. Pawley. "Unit-cell refinement from powder diffraction scans". *J Appl Cryst* **14** (1981), pp. 357–361. DOI: 10.1107/s0021889881009618.

[7] A. Le Bail, H. Duroy, and J. Fourquet. "Ab-initio structure determination of $LiSbWO_6$ by X-ray powder diffraction". *Mater. Res. Bull.* **23** (1988), pp. 447–452. DOI: 10.1016/0025-5408(88)90019-0.

[8] A.A. Coelho. *TOPAS-Academic*. Brisbane, 2007.

[9] R.W. Cheary and A.A. Coelho. "A fundamental parameters approach to X-ray line-profile fitting". *J. Appl. Crystallogr.* **25** (1992), pp. 109–121. DOI: 10.1107/S0021889891010804.

[10] R.W. Cheary and A.A. Coelho. "Axial Divergence in a Conventional X-ray Powder Diffractometer. I. Theoretical Foundations". *J. Appl. Crystallogr.* **31** (1998), pp. 851–861. DOI: 10.1107/S0021889898006876.

[11] R.A. Young. *The Rietveld Method*. Ed. by R.A. Young. Oxford University Press, 1995. DOI: 10.1002/crat.2170300412.

[12] H.P. Klug and L.E. Alexander. *X-Ray Diffraction Procedures: For Polycrystalline and Amorphous Materials, 2nd Edition*. Wiley-Interscience, 1974.

[13] T. Ino and N. Minami. "X-ray diffraction by small crystals". *Acta Crystallogr. Sect. A* **35** (1979), pp. 163–170. DOI: 10.1107/S0567739479000280.

[14] V.A. Drits and C. Tchoubar. *X-Ray Diffraction by Disordered Lamellar Structures. Theory and applications to microdivided silicates and carbons*. Berlin, Heidelberg, New York: Springer-Verlag, 1990.

[15] S.J.L. Billinge. "The nanostructure problem". *Physics* **3** (2010). DOI: 10.1103/physics.3.25.

[16] S.J.L. Billinge and I. Levin. "The Problem with Determining Atomic Structure at the Nanoscale". *Science* **316** (2007), pp. 561–565. DOI: 10.1126/science.1135080.

[17] P. Scherrer. "Bestimmung der Größe und der inneren Struktur von Kolloidteilchen mittels Röntgenstrahlen". *Nachrichten von der Gesellschaft der Wissenschaften zu Göttingen, Mathematisch-Physikalische Klasse* **1918** (1918), pp. 98–100.

[18] G. Williamson and W. Hall. "X-ray line broadening from filed aluminium and wolfram". *Acta Metallurgica* **1** (1953), pp. 22–31. DOI: 10.1016/0001-6160(53)90006-6.

[19] P. Scardi, M. Leoni, and R. Delhez. "Line broadening analysis using integral breadth methods: a critical review". *J Appl Cryst* **37** (2004), pp. 381–390. DOI: 10.1107/s0021889804004583.

[20] P. Scardi and M. Leoni. "Whole powder pattern modelling". *Acta Crystallogr. Sect. A Found. Crystallogr.* **58** (2002), pp. 190–200. DOI: 10.1107/S0108767301021298.

[21] B.E. Warren. *X-ray Diffraction*. 2nd ed. New York: Dover publications, 1990.

[22] P.P. Ewald. “X-ray diffraction by finite and imperfect crystal lattices”. *Proc. Phys. Soc.* **52** (1940), pp. 167–174. DOI: 10.1088/0959-5309/52/1/323.

[23] A.R. Stokes and A.J.C. Wilson. “A method of calculating the integral breadths of Debye-Scherrer lines”. *Mathematical Proceedings of the Cambridge Philosophical Society* **38** (1942), pp. 313–322. DOI: 10.1017/S0305004100021988.

[24] M. Wilkens. “The determination of density and distribution of dislocations in deformed single crystals from broadened X-ray diffraction profiles”. *Physica Status Solidi (a)* **2** (1970), pp. 359–370. DOI: 10.1002/pssa.19700020224.

[25] S. Hendricks and E. Teller. “X-Ray Interference in Partially Ordered Layer Lattices”. *J. Chem. Phys.* **10** (1942), p. 147. DOI: 10.1063/1.1723678.

[26] P. Scardi and M. Leoni. “Diffraction line profiles from polydisperse crystalline systems”. *Acta Crystallogr. Sect. A Found. Crystallogr.* **57** (2001), pp. 604–613. DOI: 10.1107/S0108767301008881.

[27] P. Scardi, M. Leoni, and Y. Dong. “Whole diffraction pattern-fitting of polycrystalline fcc materials based on microstructure”. *Eur. Phys. J. B* **18** (2000), pp. 23–30. DOI: 10.1007/s100510070073.

[28] G. Ribárik, T. Ungár, and J. Gubicza. “MWP-fit: a program for multiple whole-profile fitting of diffraction peak profiles by ab initio theoretical functions”. *J. Appl. Crystallogr.* **34** (2001), pp. 669–676. DOI: 10.1107/S0021889801011451.

[29] M. Leoni, T. Confente, and P. Scardi. “PM2K: a flexible program implementing Whole Powder Pattern Modelling”. *Zeitschrift für Krist. Suppl.* **23** (2006), pp. 249–254. DOI: 10.1524/zksu.2006.suppl_23.249.

[30] J. Ahmed, C.K. Blakely, S.R. Bruno, and V.V. Poltavets. “Synthesis of $MSnO_3$ (M=Ba, Sr) nanoparticles by reverse micelle method and particle size distribution analysis by whole powder pattern modeling”. *Mater. Res. Bull.* **47** (2012), pp. 2282–2287.

[31] C.K. Blakely, S.R. Bruno, Z.J. Baum, and V.V. Poltavets. “Effects of ball milling and thermal annealing on size and strain of $ASnO_3$ (A = Ba, Sr) ceramics”. *Solid State Sci.* **15** (2013), pp. 110–114.

[32] J. Ahmed, C.K. Blakely, J. Prakash, S.R. Bruno, M. Yu, Y. Wu, and V.V. Poltavets. "Scalable synthesis of delafossite $CuAlO_2$ nanoparticles for p-type dye-sensitized solar cells applications". *J. Alloys Compd.* **591** (2014), pp. 275–279. DOI: 10.1016/j.jallcom.2013.12.199.

[33] M. Abdellatief, A. Lausi, J.R. Plaisier, and P. Scardi. "Influence of Lattice Defects on the Grain Growth Kinetics of Nanocrystalline Fluorite". *Metall. Mater. Trans. A* **45** (2013), pp. 123–128. DOI: 10.1007/s11661-013-1786-8.

[34] S.V. Komogortsev, R.S. Iskhakov, A.A. Zimin, E.Y. Filatov, S.V. Korenev, Y.V. Shubin, N.A. Chizhik, G.Y. Yurkin, and E.V. Eremin. "Magnetic anisotropy and order parameter in nanostructured CoPt particles". *Appl. Phys. Lett.* **103** (2013), p. 152404. DOI: 10.1063/1.4824973.

[35] H. Jensen, J.H. Pedersen, J.E. Jørgensen, J.S. Pedersen, K.D. Joensen, S.B. Iversen, and E.G. Søgaard. "Determination of size distributions in nanosized powders by TEM, XRD, and SAXS". *Journal of Experimental Nanoscience* **1** (2006), pp. 355–373. DOI: 10.1080/17458080600752482.

[36] J. May, M. Dinkel, D. Amberger, H. Höppel, and M. Göken. "Mechanical Properties, Dislocation Density and Grain Structure of Ultrafine-Grained Aluminum and Aluminum-Magnesium Alloys". *Metall and Mat Trans A* **38** (2007), pp. 1941–1945. DOI: 10.1007/s11661-007-9110-0.

[37] M. Dinkel, F. Pyczak, J. May, H.W. Höppel, and M. Göken. "XRD profile analysis characterization of ultrafine grained Al–Mg alloys". *J. Mater. Sci.* **43** (2008), pp. 7481–7487. DOI: 10.1007/s10853-008-2859-8.

[38] I. Dragomir, D. Li, G. Castello-Branco, H. Garmestani, R. Snyder, G. Ribarik, and T. Ungar. "Evolution of dislocation density and character in hot rolled titanium determined by X-ray diffraction". *Mater. Charact.* **55** (2005), pp. 66–74. DOI: 10.1016/j.matchar.2005.03.002.

[39] L. Gelisio, C.L. Azanza Ricardo, M. Leoni, and P. Scardi. "Real-space calculation of powder diffraction patterns on graphics processing units". *J. Appl. Crystallogr.* **43** (2010), pp. 647–653.

[40] Y. Mishin, D. Farkas, M.J. Mehl, and D.A. Papaconstantopoulos. "Interatomic potentials for monoatomic metals from experimental data and ab initio calculations". *Phys. Rev. B* **59** (1999), pp. 3393–3407. DOI: 10.1103/physrevb.59.3393.

[41] C. Kittel. *Introduction to Solid State Physics*. Wiley, 2004.

[42] S. Chen, X. Gong, and S.-H. Wei. "Superhard Pseudocubic BC_2N Superlattices". *Phys. Rev. Lett.* **98** (2007), p. 015502. DOI: 10.1103/PhysRevLett.98.015502.

[43] "The 80 layer groups". In: *International Tables Online*. International Union of Crystallography (IUCr), 2006, pp. 219–389. DOI: 10.1107/97809553602060000650.

[44] G. Hägg. *Arkiv för kemi, mineralogi och geologi* **16B** (1943), pp. 1–6.

[45] Various. *International Tables for Crystallography Volume C: mathematical, physical and chemical tables*. 2004. DOI: 10.1107/97809553602060000103.

[46] E.A. Merritt. *Anomalous Scattering Coefficients*. URL: http://skuld.bmsc.washington.edu/scatter/AS_form.html.

[47] D.T. Cromer and J.B. Mann. "X-ray scattering factors computed from numerical Hartree–Fock wave functions". *Acta Cryst Sect A* **24** (1968), pp. 321–324. DOI: 10.1107/s0567739468000550.

[48] P.A. Doyle and P.S. Turner. "Relativistic Hartree–Fock X-ray and electron scattering factors". *Acta Cryst Sect A* **24** (1968), pp. 390–397. DOI: 10.1107/s0567739468000756.

[49] A.G. Fox, M.A. O'Keefe, and M.A. Tabbernor. "Relativistic Hartree–Fock X-ray and electron atomic scattering factors at high angles". *Acta Cryst Sect A* **45** (1989), pp. 786–793. DOI: 10.1107/s0108767389007567.

[50] Waber and Cromer. "International Tables for X-ray Crystallography". 1974.

[51] A. Guinier. *X-ray Diffraction in Crystals, Imperfect Crystals, and Amorphous Bodies*. Dover Books on Physics Series. Dover, 1994.

[52] L. Gelisio and P. Scardi. "X-Ray Interference by Nanocrystalline Domains". *J. Nanosci. Nanotechnol.* **12** (2012), pp. 8811–8817. DOI: 10.1166/jnn.2012.6479.

[53] A.L. Patterson. "The Diffraction of X-Rays by Small Crystalline Particles". *Phys. Rev.* **56** (1939), pp. 972–977. DOI: 10.1103/PhysRev.56.972.

[54] P. Scardi, M. Leoni, and K.R. Beyerlein. "On the modelling of the powder pattern from a nanocrystalline material". *Zeitschrift für Krist.* **226** (2011), pp. 924–933. DOI: 10.1524/zkri.2011.1448.

[55] R. Hosemann and S. Bagchi. *Direct Analysis of Diffraction by Matter*. North-Holland Pub. Co., 1962, p. 734.

[56] J.I. Langford and D. Louër. "Diffraction line profiles and Scherrer constants for materials with cylindrical crystallites". *J. Appl. Crystallogr.* **15** (1982), pp. 20–26. DOI: 10.1107/S0021889882011297.

[57] R. Vargas, D. Louër, and J.I. Langford. "Diffraction line profiles and Scherrer constants for materials with hexagonal crystallites". *J Appl Cryst* **16** (1983), pp. 512–518. DOI: 10.1107/s0021889883010924.

[58] A. Leonardi, M. Leoni, S. Siboni, and P. Scardi. "Common volume functions and diffraction line profiles of polyhedral domains". *J. Appl. Crystallogr.* **45** (2012), pp. 1162–1172. DOI: 10.1107/S0021889812039283.

[59] J.I. Langford, D. Louër, and P. Scardi. "Effect of a crystallite size distribution on X-ray diffraction line profiles and whole-powder-pattern fitting". *J Appl Cryst* **33** (2000), pp. 964–974. DOI: 10.1107/s002188980000460x.

[60] C.E. Kril and R. Birringer. "Estimating grain-size distributions in nanocrystalline materials from X-ray diffraction profile analysis". *Philosophical Magazine A* **77** (1998), pp. 621–640. DOI: 10.1080/01418619808224072.

[61] T. Ino and N. Minami. "Intensity profile of Debye–Scherrer line from small crystallites". *Acta Cryst Sect A* **40** (1984), pp. 538–544. DOI: 10.1107/s0108767384001136.

[62] K.R. Beyerlein, R.L. Snyder, and P. Scardi. "Faulting in finite face-centered-cubic crystallites". *Acta Crystallogr. Sect. A* **67** (2011), pp. 252–63. DOI: 10.1107/S0108767311009482.

[63] L. Landau. "The scattering of X-rays by crystals with variable lamellar structure". *Physika. Z. Sowjetunion* **12** (1937), 579Lif–585.

[64] M. Lifschitz. "On the theory of scattering of X-rays by crystals of variable structure". *Physika. Z. Sowjetunion* **12** (1937), pp. 623–643.

[65] A.J.C. Wilson. "Imperfections in the Structure of Cobalt. II. Mathematical Treatment of Proposed Structure". *Proceedings of the Royal Society A: Mathematical, Physical and Engineering Sciences* **180** (1942), pp. 277–285. DOI: 10.1098/rspa.1942.0040.

[66] M.S. Paterson. “X-Ray Diffraction by Face-Centered Cubic Crystals with Deformation Faults”. *J. Appl. Phys.* **23** (1952), p. 805. DOI: 10.1063/1.1702312.

[67] A.J.C. Wilson. “The Reflexion of X-Rays from the ‘Anti-Phase Nuclei’of $AuCu_3$ I. Formula”. *Proceedings of the Royal Society A: Mathematical, Physical and Engineering Sciences* **181** (1943), pp. 360–368. DOI: 10.1098/rspa.1943.0013.

[68] B. Warren. “X-ray studies of deformed metals”. *Progress in Metal Physics* **8** (1959), pp. 147–202. DOI: 10.1016/0502-8205(59)90015-2.

[69] T.R. Welberry. “Diffuse x-ray scattering and models of disorder”. *Reports on Progress in Physics* **48** (1985), p. 1543.

[70] R. Berliner and S. Werner. “Effect of stacking faults on diffraction: The structure of lithium metal”. *Phys. Rev. B* **34** (1986), pp. 3586–3603. DOI: 10.1103/PhysRevB.34.3586.

[71] E. Michalski. “The diffraction of X-rays by close-packed polytypic crystals containing single stacking faults. I. General theory”. *Acta Crystallogr. Sect. A Found. Crystallogr.* **44** (1988), pp. 640–649. DOI: 10.1107/S010876738800323X.

[72] V.B. Cajipe, P.A. Heiney, and J.E. Fischer. “In situ study of staging disorder in cesium-intercalated graphite”. *Phys. Rev. B* **39** (1989), pp. 4374–4385. DOI: 10.1103/physrevb.39.4374.

[73] J. Kakinoki and Y. Komura. “Diffraction by a one-dimensionally disordered crystal. I. The intensity equation”. *Acta Crystallogr.* **19** (1965), pp. 137–147. DOI: 10.1107/S0365110X65002888.

[74] J. Kakinoki and Y. Komura. “Comments on Allegra’s paper ‘A simplified formula for the calculation of the X-ray intensity diffracted by a monodimensionally disordered structure’”. *Acta Crystallogr.* **15** (1962), pp. 292–292. DOI: 10.1107/S0365110X62000717.

[75] J. Kakinoki and Y. Komura. “Intensity of X-ray Diffraction by an One-Dimensionally Disordered Crystal (1) General derivation in cases of the ”Reichweite” s=0 and 1”. *J. Phys. Soc. Japan* **7** (1952), pp. 30–35. DOI: 10.1143/JPSJ.7.30.

[76] J. Kakinoki and Y. Komura. “Intensity of X-ray Diffraction by a One-dimensionally Disordered Crystal (II) General Derivation in the Case of the Correlation Range s=2”. *J. Phys. Soc. Japan* **9** (1954), pp. 169–176.

[77] J. Kakinoki. “Diffraction by a one-dimensionally disordered crystal. II. Close-packed structures”. *Acta Crystallogr.* **23** (1967), pp. 875–885. DOI: 10.1107/S0365110X67003974.

[78] G. Allegra. “Il calcolo dell’intensità di diffrazione dei raggi X da parte di strutture denotanti disordine monodimensionale. Nota I. - criteri matematici”. *Nuovo Cim.* **21** (1961), pp. 786–801. DOI: 10.1007/BF02785605.

[79] G. Allegra. “A simplified formula for the calculation of the X-ray intensity diffracted by a monodimensionally disordered structure”. *Acta Crystallogr.* **14** (1961), pp. 535–535. DOI: 10.1107/S0365110X61001650.

[80] G. Allegra. “Il calcolo dell’intensità di diffrazione dei raggi X da parte di strutture denotanti disordine monodimensionale. II. - Applicazioni della teoria ad alcuni modelli strutturali con disordine monodimensionale”. *Nuovo Cim.* **22** (1961), pp. 661–672. DOI: 10.1007/BF02783099.

[81] G. Allegra. “Il calcolo dell’intensità di diffrazione dei raggi X da parte di strutture denotanti disordine monodimensionale. III. - Studio strutturale di due diverse modificazioni cristalline del $TiCl_3$ che presentano disordine monodimensionale”. *Nuovo Cim.* **23** (1962), pp. 502–515. DOI: 10.1007/BF02733203.

[82] J. Kakinoki and Y. Komura. “Intensity of X-ray Diffraction by a One-dimensionally Disordered Crystal (III) The Close-packed Structure”. *J. Phys. Soc. Japan* **9** (1954), pp. 177–183. DOI: 10.1143/JPSJ.9.177.

[83] J. Kakinoki, E. Kodera, and T. Aikami. “An application of the Patterson method to the determination of layer sequences in polytypes with close-packed structures”. *Acta Crystallogr. Sect. A* **25** (1969), pp. 385–386. DOI: 10.1107/S0567739469000659.

[84] H. Jagodzinski. “Eindimensionale Fehlordnung in Kristallen und ihr Einfluss auf die Röntgeninterferenzen. II. Berechnung der fehlgeordneten dichtesten Kugelpackungen mit Wechselwirkungen der Reichweite 3”. *Acta Crystallogr.* **2** (1949), pp. 208–214. DOI: 10.1107/S0365110X49000564.

[85] H. Jagodzinski. “Eindimensionale Fehlordnung in Kristallen und ihr Einfluss auf die Röntgeninterferenzen. I. Berechnung des Fehlordnungsgrades aus den Röntgenintensitäten”. *Acta Crystallogr.* **2** (1949), pp. 201–207. DOI: 10.1107/s0365110x49000552.

[86] H. Jagodzinski. “Eindimensionale Fehlordnung in Kristallen und ihr Einfluss auf die Röntgeninterferenzen. III. Vergleich der Berechnungen mit experimentellen Ergebnissen”. *Acta Crystallogr.* **2** (1949), pp. 298–304. DOI: 10.1107/s0365110x49000771.

[87] H. Jagodzinski. “Der Symmetrieeinfluss auf den allgemeinen Lösungsansatz eindimensionaler Fehlordnungs-probleme”. *Acta Crystallogr.* **7** (1954), pp. 17–25. DOI: 10.1107/s0365110x54000035.

[88] M.M. Treacy, J. Newsam, and M. Deem. “A general recursion method for calculating diffracted intensities from crystals containing planar faults”. *Proc. R. Soc. A Math. Phys. Eng. Sci.* **433** (1991), p. 499. DOI: 10.1098/rspa.1991.0062.

[89] H. Burzlaff and H. Zimmermann. “Bases, lattices, Bravais lattices and other classifications”. In: *Space-group symmetry*. International Union of Crystallography (IUCr), 2006, pp. 742–749. DOI: 10.1107/97809553602060000517.

[90] C. Marti, P. Thorel, B. Croset, and A. Bourdon. “Diffraction pattern of crystals with numerous stacking faults”. *Acta Crystallogr. Sect. A* **37** (1981), pp. 609–616. DOI: 10.1107/S0567739481001411.

[91] A. Plançon. “Consistent Modeling of the Xrd Patterns of Mixed-layer Phyllosilicates”. *Clays Clay Miner.* **52** (2004), pp. 47–54. DOI: 10.1346/CCMN.2004.0520106.

[92] A. Plançon, V.A. Drits, B.A. Sakharov, Z.I. Gilan, and J. Ben Brahim. “Powder diffraction by layered minerals containing different layers and/or stacking defects. Comparison between Markovian and non-Markovian models”. *J. Appl. Crystallogr.* **16** (1983), pp. 62–69. DOI: 10.1107/S0021889883009954.

[93] M. Leoni, A.F. Gualtieri, and N. Roveri. “Simultaneous refinement of structure and microstructure of layered materials”. *J. Appl. Crystallogr.* **37** (2004), pp. 166–173. DOI: 10.1107/S0021889803022787.

[94] G.W. Brindley and J. Méring. “Diffractions des rayons X par les structures en couches désordonnées. I”. *Acta Crystallogr.* **4** (1951), pp. 441–447. DOI: 10.1107/S0365110X51001409.

[96] B.E. Warren. “X-Ray Diffraction in Random Layer Lattices”. *Phys. Rev.* **59** (1941), pp. 693–698. DOI: 10.1103/physrev.59.693.

[97] R. Lamber, S. Wetjen, and N.I. Jaeger. “Size dependence of the lattice parameter of small palladium particles”. *Phys. Rev. B* **51** (1995), pp. 10968–10971. DOI: 10.1103/physrevb.51.10968.

[98] F. Zhang, S.-W. Chan, J.E. Spanier, E. Apak, Q. Jin, R.D. Robinson, and I.P. Herman. "Cerium oxide nanoparticles: Size-selective formation and structure analysis". *Appl. Phys. Lett.* **80** (2002), p. 127. DOI: 10.1063/1.1430502.

[99] L. Wu, H.J. Wiesmann, A.R. Moodenbaugh, R.F. Klie, Y. Zhu, D.O. Welch, and M. Suenaga. "Oxidation state and lattice expansion of CeO_{2-x} nanoparticles as a function of particle size". *Phys. Rev. B* **69** (2004). DOI: 10.1103/physrevb.69.125415.

[100] W.H. Qi, M.P. Wang, and Y.C. Su. "Size effect on the lattice parameters of nanoparticles". *Journal of Materials Science Letters* **21** (2002), pp. 877–878. DOI: 10.1023/a:1015778729898.

[101] R.W. Cheary and A.A. Coelho. "Synthesizing and fitting linear position-sensitive detector step-scanned line profiles". *J. Appl. Crystallogr.* **27** (1994), pp. 673–681. DOI: 10.1107/S0021889893014165.

[102] E.N. Maslen. "X-ray absorption". In: *International Tables for Crystallography*. Vol. C. The International Union of Crystallography, 2004. Chap. 6.3, pp. 599–608. DOI: 10.1107/97809553602060000103.

[103] K.R. Beyerlein, R.L. Snyder, M. Li, and P. Scardi. "Application of the Debye function to systems of crystallites". *Philos. Mag.* **90** (2010), pp. 3891–3905. DOI: 10.1080/14786435.2010.501769.

[104] S.J. Billinge. "Nanoscale structural order from the atomic pair distribution function (PDF): There's plenty of room in the middle". *Journal of Solid State Chemistry* **181** (2008), pp. 1695–1700. DOI: 10.1016/j.jssc.2008.06.046.

[105] A.S. Masadeh, E.S. Božin, C.L. Farrow, G. Paglia, P. Juhas, S.J.L. Billinge, A. Karkamkar, and M.G. Kanatzidis. "Quantitative size-dependent structure and strain determination of CdSe nanoparticles using atomic pair distribution function analysis". *Phys. Rev. B* **76** (2007). DOI: 10.1103/physrevb.76.115413.

[106] F.M. Michel, L. Ehm, S.M. Antao, P.L. Lee, P.J. Chupas, G. Liu, D.R. Strongin, M.A.A. Schoonen, B.L. Phillips, and J.B. Parise. "The Structure of Ferrihydrite, a Nanocrystalline Material". *Science* **316** (2007), pp. 1726–1729. DOI: 10.1126/science.1142525.

[108] B. Gilbert. "Nanoparticles: Strained and Stiff". *Science* **305** (2004), pp. 651–654. DOI: 10.1126/science.1098454.

[109] R.B. Neder and V.I. Korsunskiy. "Structure of nanoparticles from powder diffraction data using the pair distribution function". *J. Phys.: Condens. Matter* **17** (2005), S125–S134. DOI: 10.1088/0953-8984/17/5/013.

[110] D. Grandjean, R.E. Benfield, C. Nayral, A. Maisonnat, and B. Chaudret. "EXAFS and XANES Study of a Pure and Pd Doped Novel Sn/SnO_x Nanomaterial". *The Journal of Physical Chemistry B* **108** (2004), pp. 8876–8887. DOI: 10.1021/jp0370627.

[111] V.L. Aksenov, M.V. Koval'chuk, A.Y. Kuz'min, Y. Purans, and S.I. Tyutyunnikov. "Development of methods of EXAFS spectroscopy on synchrotron radiation beams: Review". *Crystallogr. Rep.* **51** (2006), pp. 908–935. DOI: 10.1134/s1063774506060022.

[112] S. Mondini, A.M. Ferretti, A. Puglisi, and A. Ponti. "Pebbles and PebbleJuggler: software for accurate, unbiased, and fast measurement and analysis of nanoparticle morphology from transmission electron microscopy (TEM) micrographs". *Nanoscale* **4** (2012), p. 5356. DOI: 10.1039/c2nr31276j.

[113] W. Rasband. *ImageJ*. U. S. National Institutes of Health. 1997-2014. URL: http://imagej.nih.gov/ij/.

[114] I. Sondi and B. Salopek-Sondi. "Silver nanoparticles as antimicrobial agent: a case study on E. coli as a model for Gram-negative bacteria". *J. Colloid Interface Sci.* **275** (2004), pp. 177–182. DOI: 10.1016/j.jcis.2004.02.012.

[115] L.C. Gontard, D. Ozkaya, and R.E. Dunin-Borkowski. "A simple algorithm for measuring particle size distributions on an uneven background from TEM images". *Ultramicroscopy* **111** (2011), pp. 101–106. DOI: 10.1016/j.ultramic.2010.10.011.

[116] Y. Tian, B. Xu, D. Yu, Y. Ma, Y. Wang, Y. Jiang, W. Hu, C. Tang, Y. Gao, K. Luo, Z. Zhao, L.-M. Wang, B. Wen, J. He, and Z. Liu. "Ultrahard nanotwinned cubic boron nitride". *Nature* **493** (2013), pp. 385–8. DOI: 10.1038/nature11728.

[117] Q. Huang, D. Yu, B. Xu, W. Hu, Y. Ma, Y. Wang, Z. Zhao, B. Wen, J. He, Z. Liu, and Y. Tian. "Nanotwinned diamond with unprecedented hardness and stability." *Nature* **510** (2014), pp. 250–3. DOI: 10.1038/nature13381.

[118] J.E. Bonevich and W.K. Haller. *Measuring the Size of Nanoparticles Using Transmission Electron Microscopy (TEM)*. The National Institute of Standards and Technology (NIST), 2010.

[119] ASTM. *ASTM E122-07, Standard Practice for Calculating Sample Size to Estimate, With Specified Precision, the Average for a Characteristic of a Lot or Process*. American Society for Testing and Materials.

[120] M. Chen. "Deformation Twinning in Nanocrystalline Aluminum". *Science* **300** (2003), pp. 1275–1277. DOI: 10.1126/science.1083727.

[121] V. Germain, J. Li, D. Ingert, Z.L. Wang, and M.P. Pileni. "Stacking Faults in Formation of Silver Nanodisks". *The Journal of Physical Chemistry B* **107** (2003), pp. 8717–8720. DOI: 10.1021/jp0303826.

[122] M. Yamasaki, M. Sasaki, M. Nishijima, K. Hiraga, and Y. Kawamura. "Formation of 14H long period stacking ordered structure and profuse stacking faults in Mg–Zn–Gd alloys during isothermal aging at high temperature". *Acta Mater.* **55** (2007), pp. 6798–6805. DOI: 10.1016/j.actamat.2007.08.033.

[123] H. Fujiwara, T. Kimoto, T. Tojo, and H. Matsunami. "Characterization of in-grown stacking faults in 4H–SiC (0001) epitaxial layers and its impacts on high-voltage Schottky barrier diodes". *Appl. Phys. Lett.* **87** (2005), p. 051912. DOI: 10.1063/1.1997277.

[124] K. Koumoto, S. Takeda, C.H. Pai, T. Sato, and H. Yanagida. "High-Resolution Electron Microscopy Observations of Stacking Faults in beta-SiC". *J. Am. Ceram. Soc.* **72** (1989), pp. 1985–1987. DOI: 10.1111/j.1151-2916.1989.tb06014.x.

[125] Y. Tian, B. Xu, D. Yu, Y. Ma, Y. Wang, Y. Jiang, W. Hu, C. Tang, Y. Gao, K. Luo, Z. Zhao, L.-M. Wang, B. Wen, J. He, and Z. Liu. "Ultrahard nanotwinned cubic boron nitride. Supplementary information". *Nature* **493** (2013), pp. 385–8. DOI: 10.1038/nature11728.

[126] N. Dubrovinskaia and L. Dubrovinsky. "Controversy about ultrahard nanotwinned cBN." *Nature* **502** (2013), E1–2.

[127] Z. Libor and Q. Zhang. "The synthesis of nickel nanoparticles with controlled morphology and SiO_2/Ni core-shell structures". *Mater. Chem. Phys.* **114** (2009), pp. 902–907. DOI: 10.1016/j.matchemphys.2008.10.068.

[128] D.-H. Chen and S.-H. Wu. "Synthesis of Nickel Nanoparticles in Water-in-Oil Microemulsions". *Chem. Mater.* **12** (2000), pp. 1354–1360. DOI: 10.1021/cm991167y.

[129] Y. Chen, D.-L. Peng, D. Lin, and X. Luo. "Preparation and magnetic properties of nickel nanoparticles via the thermal decomposition of nickel organometallic precursor in alkylamines". *Nanotechnology* **18** (2007), p. 505703. DOI: 10.1088/0957-4484/18/50/505703.

[130] T. Proffen and R.B. Neder. "DISCUS : a program for diffuse scattering and defect-structure simulation". *J. Appl. Crystallogr.* **30** (1997), pp. 171–175. DOI: 10.1107/S002188989600934X.

[131] A. Stukowski. "Visualization and analysis of atomistic simulation data with OVITO–the Open Visualization Tool". *Model. Simul. Mater. Sci. Eng.* **18** (2010), p. 015012.

[132] P. Debye. "Zerstreuung von Röntgenstrahlen". *Nachrichten von der Koeniglichen Gesellschaft der Wissenschaften zu Goettingen, Math. Klasse* **1915** (1915), pp. 70–76.

[133] B.D. Hall and R. Monot. "Calculating the Debye–Scherrer diffraction pattern for large clusters". *Comput. Phys.* **5** (1991), p. 414. DOI: 10.1063/1.168397.

[134] A. Cervellino, C. Giannini, and A. Guagliardi. "On the efficient evaluation of Fourier patterns for nanoparticles and clusters." *J. Comput. Chem.* **27** (2006), pp. 995–1008. DOI: 10.1002/jcc.20407.

[135] A. Cervellino, C. Giannini, A. Guagliardi, and D. Zanchet. "Quantitative analysis of gold nanoparticles from synchrotron data by means of least-squares techniques". *Eur. Phys. J. B* **41** (2004), pp. 485–493. DOI: 10.1140/epjb/e2004-00342-3.

[136] G. Cernuto, N. Masciocchi, A. Cervellino, G.M. Colonna, and A. Guagliardi. "Size and shape dependence of the photocatalytic activity of TiO_2 nanocrystals: a total scattering Debye function study." *J. Am. Chem. Soc.* **133** (2011), pp. 3114–9. DOI: 10.1021/ja110225n.

[137] A. Manceau, M.A. Marcus, S. Grangeon, M. Lanson, B. Lanson, A.-C. Gaillot, S. Skanthakumar, and L. Soderholm. "Short-range and long-range order of phyllomanganate nanoparticles determined using high-energy X-ray scattering". *J. Appl. Crystallogr.* **46** (2013), pp. 193–209. DOI: 10.1107/S0021889812047917.

[138] R.A. Kirian, X. Wang, U. Weierstall, K.E. Schmidt, J.C.H. Spence, M. Hunter, P. Fromme, T. White, H.N. Chapman, and J. Holton. "Femtosecond protein nanocrystallography—data analysis methods". *Opt. Express* **18** (2010), p. 5713. DOI: 10.1364/oe.18.005713.

[139] T.A. White, A. Barty, F. Stellato, J.M. Holton, R.A. Kirian, N.A. Zatsepin, and H.N. Chapman. "Crystallographic data processing for free-electron laser sources". *Acta Crystallogr D Biol Cryst* **69** (2013), pp. 1231–1240. DOI: 10.1107/s0907444913013620.

[140] T. Ungár, I. Dragomir, Á. Révész, and A. Borbély. "The contrast factors of dislocations in cubic crystals: the dislocation model of strain anisotropy in practice". *J Appl Cryst* **32** (1999), pp. 992–1002. DOI: 10.1107/s0021889899009334.

[141] T. Ungár, J. Gubicza, G. Ribárik, and A. Borbély. "Crystallite size distribution and dislocation structure determined by diffraction profile analysis: principles and practical application to cubic and hexagonal crystals". *J Appl Cryst* **34** (2001), pp. 298–310. DOI: 10.1107/s0021889801003715.

[142] M. Wojdyr. "Fityk : a general-purpose peak fitting program". *J Appl Cryst* **43** (2010), pp. 1126–1128. DOI: 10.1107/s0021889810030499.

[143] N. Dubrovinskaia, V.L. Solozhenko, N. Miyajima, V. Dmitriev, O.O. Kurakevych, and L. Dubrovinsky. "Superhard nanocomposite of dense polymorphs of boron nitride: Noncarbon material has reached diamond hardness". *Appl. Phys. Lett.* **90** (2007), p. 101912. DOI: 10.1063/1.2711277.

[144] V.L. Solozhenko, O.O. Kurakevych, and Y. Le Godec. "Creation of nanostuctures by extreme conditions: high-pressure synthesis of ultrahard nanocrystalline cubic boron nitride." *Adv. Mater.* **24** (2012), pp. 1540–4. DOI: 10.1002/adma.201104361.

[146] R.H. Wentorf. "Cubic Form of Boron Nitride". *J. Chem. Phys.* **26** (1957), p. 956.

[147] F.R. Corrigan and F.P. Bundy. "Direct transitions among the allotropic forms of boron nitride at high pressures and temperatures". *J. Chem. Phys.* **63** (1975), p. 3812. DOI: 10.1063/1.431874.

[148] F.P. Bundy and R.H. Wentorf. "Direct Transformation of Hexagonal Boron Nitride to Denser Forms". *The Journal of Chemical Physics* **38** (1963), p. 1144. DOI: 10.1063/1.1733815.

[149] Y. Tian, B. Xu, D. Yu, Y. Ma, Y. Wang, Y. Jiang, W. Hu, C. Tang, Y. Gao, K. Luo, Z. Zhao, L.-M. Wang, B. Wen, J. He, and Z. Liu. "Tian et al. reply." *Nature* **502** (2013), E2–3.

[150] G. Caglioti, A. Paoletti, and F. Ricci. "Choice of collimators for a crystal spectrometer for neutron diffraction". *Nucl. Instruments* **3** (1958), pp. 223–228. DOI: 10.1016/0369-643X(58)90029-X.

[151] B.H. Toby. "R factors in Rietveld analysis: How good is good enough?" *Powder Diffr.* **21** (2006), pp. 67–70. DOI: 10.1154/1.2179804.

[152] A. Leineweber and M. Leoni. "Simulation of layer-faulting in Nb_2Co_7 intermetallic compound using DIFFaX+". *Zeitschrift für Kristallographie Supplements* **2009** (2009), pp. 423–428. DOI: 10.1524/zksu.2009.0062.

[153] V. Petkov, R.G. Difrancesco, S.J.L. Billinge, M. Acharya, and H.C. Foley. "Local structure of nanoporous carbons". *Philosophical Magazine Part B* **79** (1999), pp. 1519–1530. DOI: 10.1080/13642819908218319.

[154] H. Van Swygenhoven, P.M. Derlet, and A.G. Frøseth. "Stacking fault energies and slip in nanocrystalline metals." *Nat. Mater.* **3** (2004), pp. 399–403.

[155] C.N. Chinnasamy, B. Jeyadevan, K. Shinoda, K. Tohji, A. Narayanasamy, K. Sato, and S. Hisano. "Synthesis and magnetic properties of face-centered-cubic and hexagonal-close-packed Ni nanoparticles through polyol process". *J. Appl. Phys.* **97** (2005), 10J309. DOI: 10.1063/1.1851951.

[156] M. Han, Q. Liu, J. He, Y. Song, Z. Xu, and J.M. Zhu. "Controllable Synthesis and Magnetic Properties of Cubic and Hexagonal Phase Nickel Nanocrystals". *Adv. Mater.* **19** (2007), pp. 1096–1100. DOI: 10.1002/adma.200601460.

[157] Y.T. Jeon, J.Y. Moon, G.H. Lee, J. Park, and Y. Chang. "Comparison of the magnetic properties of metastable hexagonal close-packed Ni nanoparticles with those of the stable face-centered cubic Ni nanoparticles." *J. Phys. Chem. B* **110** (2006), pp. 1187–91. DOI: 10.1021/jp054608b.

[158] M. Behrens, F. Studt, I. Kasatkin, S. Kühl, M. Hävecker, F. Abild-Pedersen, S. Zander, F. Girgsdies, P. Kurr, B.-L. Kniep, M. Tovar, R.W. Fischer, J.K. Nørskov, and R. Schlögl. "The active site of methanol synthesis over $Cu/ZnO/Al_2O_3$ industrial catalysts." *Science* **336** (2012), pp. 893–7.

[159] I. Kasatkin, P. Kurr, B. Kniep, A. Trunschke, and R. Schlögl. "Role of lattice strain and defects in copper particles on the activity of $Cu/ZnO/Al_2O_3$ catalysts for methanol synthesis." *Angew. Chem. Int. Ed. Engl.* **46** (2007), pp. 7324–7.

[160] Y. Yan, G.M. Dalpian, M.M. Al-Jassim, and S.-H. Wei. "Energetics and electronic structure of stacking faults in ZnO". *Phys. Rev. B* **70** (2004). DOI: 10.1103/physrevb.70.193206.

[161] D. Gerthsen, D. Litvinov, T. Gruber, C. Kirchner, and A. Waag. "Origin and consequences of a high stacking fault density in epitaxial ZnO layers". *Appl. Phys. Lett.* **81** (2002), p. 3972. DOI: 10.1063/1.1523151.

[162] H. Blank, P. Delavignette, and S. Amelinckx. "Dislocations and wide stacking faults in wurtzite type crystals: Zinc sulfide and aluminium nitride". *physica status solidi (b)* **2** (1962), pp. 1660–1669. DOI: 10.1002/pssb.19620021204.

[163] L.H. Kuo. "Generation of degradation defects, stacking faults, and misfit dislocations in ZnSe-based films grown on GaAs". *J. Vac. Sci. Technol. B* **13** (1995), p. 1694. DOI: 10.1116/1.587880.

[164] L.H. Kuo, L. Salamanca-Riba, B.J. Wu, G. Hofler, J.M. DePuydt, and H. Cheng. "Dependence of the density and type of stacking faults on the surface treatment of the substrate and growth mode in ZnS_xSe_{1-x}/ZnSe buffer layer/GaAs heterostructures". *Appl. Phys. Lett.* **67** (1995), p. 3298. DOI: 10.1063/1.115226.

[165] H. Shtrikman, R. Popovitz-Biro, A. Kretinin, L. Houben, M. Heiblum, M. Bukała, M. Galicka, R. Buczko, and P. Kacman. "Method for Suppression of Stacking Faults in Wurtzite III-V Nanowires". *Nano Letters* **9** (2009), pp. 1506–1510. DOI: 10.1021/nl803524s.

[166] S. Takeuchi, K. Suzuki, K. Maeda, and H. Iwanaga. "Stacking-fault energy of II–VI compounds". *Philosophical Magazine A* **50** (1985), pp. 171–178. DOI: 10.1080/01418618408244220.

[167] L. Kazmerski. "Role of defects in determining the electrical properties of CdS thin films. II. Stacking faults". *J. Appl. Phys.* **43** (1972), p. 3521. DOI: 10.1063/1.1661747.

[168] D. Schikora, S. Schwedhelm, D.J. As, K. Lischka, D. Litvinov, A. Rosenauer, D. Gerthsen, M. Strassburg, A. Hoffmann, and D. Bimberg. "Investigations on the Stranski–Krastanow growth of CdSe quantum dots". *Appl. Phys. Lett.* **76** (2000), p. 418. DOI: 10.1063/1.125773.

[169] M.G. Bawendi, A.R. Kortan, M.L. Steigerwald, and L.E. Brus. "X-ray structural characterization of larger CdSe semiconductor clusters". *The Journal of Chemical Physics* **91** (1989), p. 7282. DOI: 10.1063/1.457295.

[170] A. Plançon and C. Tchoubar. “Determination of structural defects in phyllosilicates by X-ray powder diffraction; I, Principle of calculation of the diffraction phenomenon”. *Clays Clay Miner.* **25** (1977), pp. 430–435.

[171] A. Plançon and C. Tchoubar. “Determination of structural defects in phyllosilicates by X-ray powder diffraction; II, Nature and proportion of defects in natural kaolinites”. *Clays Clay Miner.* **25** (1977), pp. 436–450.

[172] G.W. Brindley and G. Brown, eds. *Crystal Structures of Clay Minerals and their X-Ray Identification*. Mineralogical Society, 1980. DOI: 10.1180/mono-5.

[173] V. Rives. “Layered Double Hydroxides present and future”. *Appl. Clay Sci.* **22** (2002), pp. 75–76. DOI: 10.1177/1090820X10380861.

[174] P. Nalawade, B. Aware, V. Kadam, and R. Hirlekar. “Layered double hydroxides: A review”. *J. Sci. Ind. Res. (India).* **68** (2009), pp. 267–272.

[175] C. Forano, T. Hibino, F. Leroux, and C. Taviot-Guého. “Layered Double Hydroxides”. In: *Handb. Clay Sci.* Ed. by F. Bergaya, B. Theng, and G. Lagaly. 2006, pp. 1021–1095. DOI: 10.1016/S1572-4352(05)01039-1.

[176] V. Ambrogi, G. Fardella, G. Grandolini, and L. Perioli. “Intercalation compounds of hydrotalcite-like anionic clays with antiinflammatory agents - I. Intercalation and in vitro release of ibuprofen”. *Int. J. Pharm.* **220** (2001), pp. 23–32.

[177] M.I. Carretero and M. Pozo. “Clay and non-clay minerals in the pharmaceutical industryPart I. Excipients and medical applications”. *Appl. Clay Sci.* **46** (2009), pp. 73–80. DOI: 10.1016/j.clay.2009.07.017.

[178] V. Ambrogi, L. Perioli, V. Ciarnelli, M. Nocchetti, and C. Rossi. “Effect of gliclazide immobilization into layered double hydroxide on drug release”. *Eur. J. Pharm. Biopharm.* **73** (2009), pp. 285–91. DOI: 10.1016/j.ejpb.2009.06.007.

[179] S.V. Prasanna, R.A.P. Rao, and P.V. Kamath. “Layered double hydroxides as potential chromate scavengers”. *J. Colloid Interface Sci.* **304** (2006), pp. 292–299. DOI: 10.1016/j.jcis.2006.08.064.

[180] Q. Wang and D. O’Hare. “Recent advances in the synthesis and application of layered double hydroxide (LDH) nanosheets”. *Chem. Rev.* **112** (2012), pp. 4124–55. DOI: 10.1021/cr200434v.

[181] M.V. Sychev. “Hydrotalcites: relation between structural features, basicity and activity in the Wittig reaction”. *Appl. Clay Sci.* **18** (2001), pp. 103–110. DOI: 10.1016/S0169-1317(00)00034-X.

[184] US National Institute of Standards and Technology. *The NIST Reference on Constants, Units, and Uncertainty*. *http://physics.nist.gov/cuu/index.html*. 2011.

Scientific Production

[95] R. Koch and M. Leoni. "Combined quantitative analysis of structure and nanostructure in disordered crystalline materials". *Scientific Reports* (2015, Accepted pending major revisions).

[107] P. Metz, R. Koch, C. B., K. Page, J. Neuefiend, and S.T. Misture. "X-ray and neutron total scattering analysis of $H_y(Bi_{0.2}Ca_{0.55}Sr_{0.25})(Ag_{0.25}Na_{0.75})Nb_3O_{10}$ xH_2O perovskite nanosheet booklets with stacking disorder". *Adv. X-Ray Anal.* (2015, Submitted).

[145] R. Koch and M. Leoni. "The elusive structure/nanostructure of superhard boron nitride". 2015, In Preparation.

[182] R. Koch. "European Powder Diffraction Conference (EPDIC 13)". *Powder Diffr.* **28** (2013), pp. 53–54. DOI: 10.1017/s0885715613000043.

[183] R.J. Koch, I.N. Lokuhewa, J. Shi, M.S. Haluska, and S.T. Misture. "Chemical synthesis of nanoscale Aurivillius ceramics, $Bi_2A_2TiM_2O_{12}$ (A = Ca, Sr, Ba and M = Nb, Ta)". *J. Sol-Gel Sci. Technol.* **64** (2012), pp. 612–618. DOI: 10.1007/s10971-012-2892-6.